**From the holdings of the Department of Special Collections , Princeton University Library, Princeton, NJ**

These documents are either in the public domain, or can only be used for educational and research purposes (Fair use) as per U.S. Copyright law (text below). By accessing this file, all users agree that their use falls in the public domain or within fair use as defined by the copyrightlaw. We do not charge any permission or usage fees for the publication of images of material inour collections, including those provided by Princeton University Library, via our website, catalog, or directly from staff.For more information regarding copyright, credit, and citation please review the information onthe Copyright, Credit and Citation Guidelines page of our website.
https://library.princeton.edu/special-collections/policies/copyright-credit-and-citation-guidelines. If you have any questions, including how to order higher-quality images from the collection, contact Special Collections Public Services via our Ask Us! Form. https://library.princeton.edu/special-collections/ask-us

---

Doctoral Dissertations, 2011-2026 Atmospheric and Oceanic Sciences

2018

# The Influence of Aerosols on Large-scale Circulation and Regional Climate

Shen, Zhaoyi

Princeton, NJ : Princeton University

---

http://arks.princeton.edu/ark:/88435/dsp015h73pz82s

*U.S. Copyright law: The copyright law of the United States (Title 17, §108, United States Code) governs the making of photocopies or other reproductions of copyrighted material. Under certain conditions specified in the law, libraries and archives are authorized to furnish a photocopy or other reproduction. One of these specified conditions is that the photocopy or reproduction is not to be used for any purpose other than private study, scholarship, or research. If a user makes a request for, or later uses, a photocopy or reproduction for purposes in excess of fair use that user may be liable for copyright infringement. This institution reserves the right to refuse to accept a copying order if, in its judgment, fulfillment of the order would involve a violation of copyright law. https://www.copyright.gov/title17/title17.pdf*

# The influence of aerosols on large-scale circulation and regional climate

Zhaoyi Shen

A Dissertation
Presented to the Faculty
of Princeton University
in Candidacy for the Degree
of Doctor of Philosophy

Recommended for Acceptance
by the Program in
Atmospheric and Oceanic Sciences
Adviser: Dr. Yi Ming

September 2018

© Copyright by Zhaoyi Shen, 2018.

All rights reserved.

# Abstract

Aerosols play an important role in the Earth's climate system by scattering and absorbing solar radiation and by interacting with clouds. Using the Geophysical Fluid Dynamics Laboratory (GFDL) atmospheric general circulation models (AGCMs), we investigate aerosol transport and removal processes and the effects of aerosols on large-scale circulation. We also quantify how aerosols have affected twentieth-century climate.

Arctic haze refers to the accumulation of aerosols in the Arctic, which results from the long-range transport of aerosols originating in mid-latitude industrial regions. We use the GFDL AM3 model to elucidate the factors driving the seasonal cycle of Arctic haze. The transport of aerosols into the Arctic is shown to vary little throughout the year, with the seasonal cycle of Arctic haze instead attributed mostly to the changes in wet removal, which becomes less efficient during summertime. The results suggest that future changes in precipitation can potentially alter the concentrations of Arctic aerosols, with implications for air quality and climate.

The climate effects of absorbing and scattering aerosols differ greatly. We examine the effects of absorbing aerosols on atmospheric circulation using the GFDL AM2 model. Absorbing aerosols in the free troposphere stabilize the mid-latitude atmospheric column, which decreases baroclinic eddy activity and thus reduces meridional energy transport at mid-latitudes. The effectiveness of absorbing aerosols in altering circulation generally increases with their height. Scattering aerosols, on the other hand, cool the climate and alter atmospheric circulation in a nearly opposite way to greenhouse gases. Using GFDL AM2 coupled to a slab ocean model, we find that the circulation responses to scattering aerosols and greenhouse gases are not linearly additive. The nonlinearity mainly arises from cloud radiative responses.

Large uncertainty remains in the climate impacts of aerosols. We use GFDL AGCMs to decompose historical land temperature change due to anthropogenic

aerosols into fast and slow components. It is found that the fast response to aerosols significantly contributes to the observed European warming in recent decades but results in cooling over Asia. We demonstrate that AGCM simulations of the fast response are useful for empirically constraining historical aerosol forcing.

# Acknowledgements

This dissertation would not have been possible without the support and help from my advisor and committee, my friends and my family, and many people from Princeton AOS program and NOAA GFDL.

Foremost I would like to thank my advisor, Yi Ming, for his scientific guidance, patience and unwavering support over these years. Yi has been not only a wonderful advisor, but also a great mentor and friend. My committee members, Isaac Held, Larry Horowitz and V. "Ram" Ramaswamy, have greatly improved my research through their questions and feedback. I would like to thank Isaac for his critical and inspiring comments on my work and for his advice on my scientific career. Larry has provided invaluable help with running GFDL models. Ram has always made himself available for discussion despite his busy schedule.

The Princeton AOS program and NOAA GFDL have provided a stimulating environment to study and work. I am grateful to numerous scientists, post-docs and graduate students, but in particular I would like to mention V. Balaji, Spencer Clark, Songmiao Fan, Spencer Hill, Pu Lin, Fabien Paulot, Levi Silvers and Ming Zhao for helpful conversations. The AOS community would not be such an amazing place without the administrative support by Anna Valerio. Dale Walton at GFDL has been a good friend to talk with. I thank my AOS cohort, Anna FitzMaurice and Youmi Oh, for their friendship, and I will cherish all the fun we had together.

Lastly, I am deeply grateful for my family. My parents have always provided me with unconditional love and undertanding. I thank my husband, Junyi Chai, whom I met in the Princeton AOS program. Junyi has been extremely supportive during my PhD, and has always encouraged me to pursue an academic career.

The work presented here has been generously funded by the Princeton/NOAA Cooperative Institute for Climate Science.

# Contents

Abstract . . . . . iii

Acknowledgements . . . . . v

List of Tables . . . . . ix

List of Figures . . . . . x

**1 Introduction** **1**

1.1 Motivation . . . . . 1

1.2 Overview . . . . . 4

**2 On the Seasonality of Arctic Black Carbon** **7**

2.1 Introduction . . . . . 7

2.2 Model Description . . . . . 10

2.3 Simulated and observed seasonal cycle of Arctic BC . . . . . 14

2.4 Controlling factors of Arctic BC . . . . . 15

2.5 Meridional transport . . . . . 17

2.6 Hydrophilic fraction . . . . . 20

2.7 BCpi wet deposition efficiency . . . . . 22

2.8 Concluding remarks . . . . . 24

**3 The Influence of Aerosol Absorption on the Extratropical Circulation** **33**

3.1 Introduction . . . . . 33

3.2 Method . . . . . 36
3.3 Results . . . . . 39
3.3.1 Temperature and zonal wind . . . . . 39
3.3.2 Mean circulation and eddy activity . . . . . 41
3.3.3 Energy budget . . . . . 44
3.4 Theory . . . . . 46
3.5 Discussion and conclusions . . . . . 51

**4 Nonlinear boreal winter tropical circulation response to greenhouse gas and aerosol forcing 63**
4.1 Introduction . . . . . 63
4.2 Method . . . . . 65
4.2.1 Solar forcing perturbation . . . . . 65
4.2.2 Model description and experimental design . . . . . 66
4.3 Results . . . . . 67
4.4 Discussion and conclusions . . . . . 71

**5 Constraining aerosol forcing from land surface air temperature records 79**
5.1 Introduction . . . . . 79
5.2 Methods . . . . . 81
5.2.1 Climate data and climate model simulations . . . . . 81
5.2.2 Statistical analysis . . . . . 82
5.3 Results . . . . . 83
5.4 Discussion and conclusions . . . . . 87

**6 Conclusions 94**
6.1 Summary and Implications . . . . . 94
6.2 Limitations and Future Work . . . . . 97

**Bibliography** **100**

# List of Tables

2.1 Global and Arctic annual mean BC budgets in AM3. . . . . 28

5.1 Comparison of observed and simulated LSAT changes (K) in recent decades shown as the 2001-15 average minus the 1961-80 average. All simulated data are based on ensemble means. An asterisk indicates that the difference between simulated and observed LSAT changes is significant at $P < 0.1$. . . . . 89

# List of Figures

2.1 (top) Model simulated and observed monthly mean surface BC at Alert (2008-2012), Barrow (2008-2013), and Zeppelin (2008-2013). Error bars denote one standard deviation from monthly means. (bottom) Model simulated and observed BC vertical profiles at high latitudes (66°-85°N) during HIPPO (HIPPO1: January 2009, HIPPO2: October-November 2009, HIPPO3: March-April 2010, HIPPO4: June-July 2011, HIPPO5: August-September 2011). Error bars associated with observational profiles represent one standard deviation of the HIPPO data. For the comparison, daily BC fields archived from the model are first sampled along the flight track and then averaged over 66°-85°N for each campaign. . . . . 29

2.2 Monthly mean (a) Arctic BC column burdens simulated using AM3 (red) and derived from the box model (black), (b) AM3 simulated total meridional BC flux into the Arctic (solid) and contributions from the mean meridional circulation (dashed), stationary eddies (dash-dot), and transient eddies (dotted). Error bars denote one standard deviation from monthly means. . . . . 29

2.3 Vertical profiles of meridional BC flux at 66°N. The solid and dashed lines represent DJF and JJA, respectively. . . . . 30

2.4 Time-filtered meridional BC flux ($\{\overline{v_n c_n}\}$ defined in Section 5) as a fraction of total flux at 66°N. The solid and dashed lines represent DJF and JJA, respectively. . . . . 30

2.5 Scatter plot of vertically integrated monthly mean meridional BC flux by transient eddies versus meridional gradients of BC column burden averaged over 40°-66°N. The linear regression line is also shown. Green and red dots represent DJF and JJA, respectively. . . . . 31

2.6 Monthly mean AM3 simulated (a) hydrophilic fractions of Arctic BC (solid) and BC flux into the Arctic (dashed), (b) BC aging time averaged at 66°-90°N (solid) and 40°-66°N (dashed), (c) Arctic BCpi wet deposition efficiency, (d) rate coefficients of conversion of cloud condensate to rain (solid) and snow (dashed) in the Arctic, (e) Arctic rain rate, and (f) Arctic cloud water path. Error bars denote one standard deviation from monthly means. . . . . 32

3.1 Changes in (left) zonal mean temperature and (right) zonal wind resulting from BC at $\sigma$ = (a),(d) 0.38, (b),(e) 0.60, and (c),(f) 0.90 (bottom). The black contour lines denote the climatological mean in the control run. The hatching represents significance at the 0.05 level. 54

3.2 Changes in zonal mean eddy momentum flux resulting from BC at $\sigma$ = 0.38. The black contour lines denote the climatological mean in the control run. The hatching represents significance at the 0.05 level. . 55

3.3 Changes in (left) zonal mean temperature and (right) zonal wind resulting from BC in the (a),(d) tropics (30°S-30°N), (b),(e) mid-latitudes (30°-60°N and 30°-60°S), and (c),(f) high latitudes (60°-90°N and 60°-90°N) at $\sigma$ = 0.38. The black contour lines denote the climatological mean in the control run. The hatching represents significance at the 0.05 level. . . . . 56

3.4 Changes in zonal mean eddy momentum flux resulting from BC in the (a) tropics, (b) mid-latitudes, and (c) high latitudes (bottom) at $\sigma$ = 0.38. The black contour lines denote the climatological mean in the control run. The hatching represents significance at the 0.05 level. . 57

3.5 Changes in meridional streamfunction resulting from BC at $\sigma$ = (a) 0.38, (b) 0.60, and (c) 0.90. The black contour lines denote the climatological mean in the control run. Positive values indicate clockwise motion and negative values indicate counterclockwise motion. The hatching represents significance at the 0.05 level. . . . . 58

3.6 Changes in northward energy flux (red solid) and contributions from the mean meridional circulation (black solid), stationary eddies (black dashed), and transient eddies (black dotted) resulting from BC at $\sigma$ = (a) 0.38, (b) 0.60, and (c) 0.90. Note that the y-axis scale is different in (a), (b) and (c). . . . . 59

3.7 Changes in (left) northward energy flux by transient eddy and (right) eddy kinetic energy resulting from BC at $\sigma$ = (a),(d) 0.38, (b),(e) 0.60, and (c),(f) 0.90. The black contour lines denote the climatological mean in the control run. The hatching represents significance at the 0.05 level. . . . . 60

3.8 Changes in mid-latitude heating rates caused by shortwave (SW) and longwave (LW) radiation, latent heat release by convective (CV) and large-scale (LS) cloud formation, subgrid vertical diffusion (VD), and dynamical advection (DY) resulting from BC at $\sigma$ = (a) 0.38, (b) 0.60, and (c) 0.90. . . . . 61

3.9 Changes in mid-latitude adiabatic heating rates averaged at mid-latitudes resulting from BC at $\sigma$ = (a) 0.38 and (b) 0.60. Solid lines represent changes in the meridional (black) and vertical (red) advection of heat by the mean meridional circulation. Dashed lines represent changes in meridional (black) and vertical (red) eddy heat flux convergence. . . . . 61

3.10 Vertical profiles of temperature changes at mid-latitudes resulting from (a) BC at $\sigma = 0.38$ (red) and $\sigma = 0.60$ (green) in AM2 and (b) heating at $\sigma = 0.38$ (red) and $\sigma = 0.58$ (green) in the idealized model. . . . . 62

4.1 (a) Normalized annual mean perturbation to incoming solar radiation ($M$ = 1.0). (b) DJF mean radiative forcing of solar radiation perturbation (red, $M$ = 4.0) and anthropogenic aerosols (black, derived from the experiments in Ming and Ramaswamy (2009)). The radiative forcing is normalized to a global mean of 1 W $m^{-2}$. . . . . 73

4.2 Changes in DJF zonal-mean (left) temperature (K) and (right) zonal wind (m $s^{-1}$) resulting from (a,e) a doubling of $CO_2$, (b,f) a reduction in solar forcing ($M$ = 4.0), and (c,g) the combined forcing. Nonlinearity in the responses of zonal mean (d) temperature and (h) zonal wind is also shown. The black contours denote the climatological mean from the control run. . . . . 74

4.3 Changes in DJF mean meridional streamfunction ($m^2$ $s^{-1}$) resulting from (a) a doubling of $CO_2$, (b) a reduction in solar forcing ($M$ = 4.0), and (c) the combined forcing. (d) Nonlinearity in the response of meridional streamfunction. The black contours denote the climatological mean from the control run. . . . . 75

4.4 Changes in DJF zonal-mean precipitation resulting from a doubling of $CO_2$ (blue), a reduction in solar forcing ($M$ = 4.0, red), and the combined forcing (black). The grey line represents the linear sum of precipitation changes. . . . . 76

4.5 The relationship between the nonlinearity in mass flux change at the equator and hemispheric difference (0°-45°N average minus 0°-45°S average) in 850 hPa temperature. Positive mass flux indicates a northward upper level flow. . . . . 76

4.6 Nonlinearity in (a,d) DJF, (b,e) JJA, and (c,f) annual mean responses in (left) 850 hPa temperature and (right) cloud radiative effects. . . 77

4.7 Nonlinearity in (a) DJF, (b) JJA, and (c) annual mean responses in low cloud amount. . . . . 78

5.1 Time series (1961-2015) of JJASON mean NH LSAT anomalies from observations (black solid lines), (a)NO_F, (b) NO_AERO, and (c) ALL_F. Anomalies are deviations with respect to the 1961-80 reference period. The colored solid line represents the ensemble mean and the shading represents the full ensemble range (AM2 in red, AM3 in blue). The dashed line represents the 2001-15 average. Strong El Nino (E), La Nina (L), and volcanic eruptions (V) are marked in the figure. The right column shows an enlarged plot of 2001-15 temperature anomalies. . . . . 90

5.2 JJASON mean LSAT changes over (a) NH, (b) Europe (38° -66° N, 10° W-50° E), and (c) Asia (8° -38° N, 70° -123° E) in recent decades shown as the 2001-15 average minus the 1961-80 average from observations (black), AM2 (red), and AM3 (blue). Box shows the mean temperature change (center line) and its 95% confidence interval. Black circles represent LSAT changes from individual ensemble numbers. . . . . 91

5.3 (a) Observed and (b-g) observed minus model simulated JJASON mean surface air temperature change in recent decades shown as the 2001-15 average minus the 1961-80 average. b, d, and f show results from AM2; c, e, and g show results from AM3. Stippling indicates regions exceeding 95% statistical confidence. Solid and dashed rectangles denote Europe and Asia used for averaging in Fig. 5.2. . . . . 92

5.4 Time series (1961-2015) of JJASON mean non-aerosol (solid) and aerosol (dashed) effective radiative forcing over (a) Europe and (b) Asia. Red and blue lines represent AM2 and AM3, respectively. Thick and thin lines represent five-year running mean and annual mean, respectively. . . . . 93

# Chapter 1

# Introduction

## 1.1 Motivation

Atmospheric aerosols are tiny solid or liquid particles suspended in the air. They are emitted directly to the Earth's atmosphere from both natural and anthropogenic sources or can form in the atmosphere from gas-phase precursors. Aerosols come in a wide range of sizes, chemical compositions, and concentrations. Natural aerosols mainly arise from sea spray, wind-borne dust, and volcanic eruptions, and anthropogenic emissions of aerosols and their precursors involve combustion of fossil fuel, biofuel and biomass (e.g., de Leeuw et al., 2011; Ginoux et al., 2012; Bond et al., 2013). Aerosols can be transported from source regions to remote areas and are removed from the atmosphere by gravitational settling and by wet and dry deposition (Seinfeld and Pandis, 2006). The lifetime of aerosols ranges from hours to days near the surface to several weeks in the free troposphere (Boucher et al., 2013). As a result of the relatively short lifetime, the spatial distribution of aerosols is very inhomogeneous, as opposed to the more uniformly distributed greenhouse gases.

Although aerosols constitute only a very small fraction of the atmosphere, they interact strongly with Earth's energy budget and hydrological and chemical cycle.

Therefore, they have significant effects on climate, weather, and atmospheric composition. Aerosols perturb the Earth's energy balance in several ways. They directly scatter and absorb incoming solar radiation and, to a lesser extent, terrestrial radiation (Boucher et al., 2013). Some aerosol particles act as cloud condensation nuclei or ice nuclei and thus can increase the albedo of clouds by increasing cloud droplet number concentration and decreasing the droplet size (Twomey, 1977). In addition, aerosols also affect the lifetime of clouds by modulating precipitation (Albrecht, 1989; Liou and Ou, 1989). The overall aerosol-cloud-precipitation interaction involves many physical processes operating over a wide range of scales and is highly uncertain. Besides playing an important role in the climate system, aerosols are also a major component of air pollution that have adverse effects on air quality, ecosystems and human health (e.g., Law and Stohl, 2007; Carmichael et al., 2009).

Anthropogenic aerosols have increased substantially since pre-industrial times (1750), resulting in a global mean top-of-atmosphere effective radiative forcing of -0.45 (-0.95 to 0.05) W $m^{-2}$ due to aerosol-radiation interactions and -0.45 (-1.2 to 0.0) W $m^{-2}$ due to aerosol-cloud interactions (Myhre et al., 2013). It is believed that the overall effect of aerosols is to cool the Earth and to offset a substantial fraction of the positive radiative forcing due to the increase in well-mixed greenhouse gases, which is estimated as 2.83 (2.54 to 3.12) W $m^{-2}$ (Myhre et al., 2013). In recent decades, anthropogenic aerosol emissions have decreased steadily over Europe and North America in response to air pollution regulations, but have increased in many developing countries especially in Asia (Smith et al., 2011). The regional redistribution of emissions results in a small net change in the effect of aerosols on the global mean temperature over this time period (Myhre et al., 2015). Anthropogenic aerosol emissions are projected to decline over the next century under the Representative Concentration Pathways and eventually exert a warming effect (Lamarque et al., 2011). As a result of the spatial inhomogeneity, aerosols also cause changes

in atmospheric circulation patterns and regional climate. These impacts are much stronger and more uncertain than the global mean climate effect of aerosols, and are the primary focus of this dissertation.

Sulfate and black carbon typify two major types of anthropogenic aerosols with very different radiative properties. Sulfate is a common type of scattering aerosol that partly offsets the climate impacts of greenhouse gases by reflecting solar radiation. Previous studies have shown the impacts of scattering aerosols on atmospheric circulation oppose the greenhouse gas-induced changes. Since sulfate is concentrated at midlatitude industrial regions in the Northern Hemisphere, the interhemispheric asymmetry in aerosol forcing results in a strengthening of the Hadley circulation in the boreal winter and a southward shift of the intertropical convergence zone (Ming and Ramaswamy, 2011). Sulfate aerosols also yield an equatorward shift of the subtropical jet and mid-latitude storm track (Fischer-Bruns et al., 2009; Ming and Ramaswamy, 2009), as well as zonally-asymmetric circulation changes at midlatitudes by altering stationary Rossby waves. On synoptic scales, sulfate aerosols emitted from Asia have been shown to invigorate midlatitude cyclones and increase precipitation over the Pacific (Wang et al., 2014c,b).

Black carbon, on the other hand, is the dominant type of absorbing aerosol. It absorbs solar radiation and has a warming effect along with greenhouse gases. However, the climate response to absorbing aerosols and greenhouse gases are not similar. Unlike the response to greenhouse gas-induced warming, the global mean precipitation increase resulting from the warming caused by absorbing aerosols does not scale with surface temperature change since the strong atmospheric absorption suppresses precipitation (Ming et al., 2010). This atmospheric absorption causes the climate effects of absorbing aerosols to be more significant at regional scales, especially in the major source regions. For example, it has been shown that absorbing aerosols have a strong influence on the monsoon evolution over South Asia (Bollasina et al., 2008; Randles

and Ramaswamy, 2008). In contrast to the effect of scattering aerosols on atmospheric circulation, absorbing aerosols result in a northward shift of the intertropical convergence zone, accompanied by a weakening (strengthening) of the tropical circulation in the boreal winter (summer) (Allen and Sherwood, 2011; Ocko et al., 2014). The increase in black carbon emissions and associated atmospheric heating at Northern Hemisphere midlatitudes is thought to play an important role in driving tropical expansion in recent years (Allen et al., 2012).

The overall picture of aerosol-climate interactions is complicated and highly uncertain due to a variety of poorly understood processes. Results from model simulations of aerosol concentrations vary widely, and often contain large biases when compared with observations at both source regions and remote areas (e.g., Koffi et al., 2012; Eckhardt et al., 2015). These biases result from uncertainties in emission inventories and physical and chemical processes during atmospheric transport, including hygroscopic growth, wet removal, and dry deposition (Boucher et al., 2013; Bond et al., 2013). Besides aerosol concentrations themselves, limited knowledge of aerosol-cloud interactions also contributes significantly to the uncertainty in model simulated aerosol forcing (Seinfeld et al., 2016). While our of aerosol processes have improved as more observations of aerosol properties have been made in recent years, uncertainty in aerosol forcing remains the dominant contributor to the overall uncertainty in anthropogenic forcing, and thus the response of the climate system (Myhre et al., 2013). Reducing the uncertainty range of aerosol forcing is a major challenge of great scientific and societal importance.

## 1.2 Overview

As introduced in Section 1.1, this dissertation investigates various aspects of aerosol-climate interactions. Chapter 2 focuses on Arctic haze, which refers to accumulation

of aerosols in the Arctic during winter and spring. Arctic haze results from long-range transport of aerosols originating from the mid-latitude industrial regions, and influences on Arctic climate. We analyze the characteristics of long-range meridional transport to the Arctic troposphere and physical and chemical processes occurring during this transport. We further resolve uncertainties from previous studies concerning the relative importance of the factors controlling the seasonal cycle of Arctic hazed.

Chapters 3 and 4 address the impact of aerosols on the large-scale atmospheric circulation. In Chapter 3, we use both comprehensive and idealized general circulation models to analyze how absorbing aerosols affect extratropical circulation features such as the jet stream and baroclinic eddies, an issue that has not received much attention in the literature. We examine the dependence of the atmospheric response on the altitude of absorbing aerosols and elucidate the underlying mechanism using dry baroclinic eddy theories. In Chapter 4 we shift the focus to scattering aerosols. Since greenhouse gases and scattering aerosols have opposite effects on the climate system, we investigate whether the climate responses to these two forcings are linearly additive. We conduct idealized forcing experiments to examine systematically the impact of scattering aerosols and propose possible causes of the nonlinearity in the circulation response.

Chapter 5 quantifies how aerosols have affected 20th century climate and explores a possible approach by which observations could be used to constrain aerosol forcing. We use atmospheric general circulation models to decompose the historical land temperature change due to anthropogenic forcing into a fast atmospheric-land-only component and a slow component due to the changing ocean. We demonstrate that the fast component is detectable in the observed land warming in the Northern Hemisphere in recent decades. We further attempt to use the model simulations of the fast response of regional land temperature, in conjunction with the observed records,

to reduce the uncertainty in historical aerosol forcing. Finally, Chapter 6 concludes this dissertation with a summary of the results and discussion on the limitations and directions of future work.

Chapter 2 is joint work with Yi Ming, Larry Horowitz, V. Ramaswamy, and Meiyun Lin. Chapters 3 and 4 are joint work with Yi Ming. Chapter 5 is joint work with Yi Ming and Isaac Held. The results of Chapters 2, 3 and 5 have been presented at various conferences, including the 2015, 2016 and 2017 AGU Fall Meeting and the 98th AMS Annual Meeting. Chapter 2 is published as Shen et al. (2017) and Chapter 3 is published as Shen and Ming (2018). Chapter 5 is currently in preparation for submission with Yi Ming and Isaac Held as co-authors.

# Chapter 2

# On the Seasonality of Arctic Black Carbon

## 2.1 Introduction

The discovery of accumulation of visibility-reducing aerosols in the Arctic during late winter and early spring (known as Arctic haze) dates back to late 1800s (Garrett and Verzella, 2008, and references therein). After being under-appreciated for decades, the haze was rediscovered by pilots flying over the North American Arctic in the 1950s (Mitchell, 1957). Since then the haze has been attracting interests among researchers. The haze has its root cause in the long-range transport of air pollution originating from the mid-latitude industrial regions (Barrie, 1986), and can have an influence on Arctic climate (Law and Stohl, 2007). The haze is a mixture of both light-scattering and light-absorbing aerosols. Black carbon (BC), which accounts for most of the aerosol absorption (Law and Stohl, 2007), is a minor but important component of Arctic haze. BC poses strong positive radiative perturbations by absorbing solar radiation, by interacting with clouds, and by reducing the surface albedo when deposited onto snow and ice (Quinn et al., 2007). The surface temperature in the

Arctic increased more than the global average since the late 20th century, coinciding with a rapid decline of sea ice (Bindoff et al., 2013a). Besides greenhouse gases, increased BC and decreased scattering aerosols (e.g. sulfate) in the Arctic due to the long-term emission trends were postulated to have contributed to this amplified Arctic climate change (Shindell and Faluvegi, 2009).

A distinct seasonal cycle of Arctic BC concentrations is present in measurements. Long-term surface observations at Alert and Barrow show that BC concentrations tend to peak during late winter and early spring before starting to decline in April, and reach a minimum during summer (Sharma et al., 2006). Recent aircraft measurements of BC have shown that the seasonal change in BC vertical structures is in agreement with the seasonality of surface concentrations (Koch et al., 2009; Eckhardt et al., 2015). Different seasonally dependent mechanisms, such as atmospheric transport and removal, have been posited to explain the seasonal cycle of Arctic BC.

Previous studies have shown that similar to other aerosols, Arctic BC is dominated by emissions from Europe and the Asian part of Russia, with smaller contributions from East Asia and North America (e.g., Stohl, 2006; Shindell et al., 2008). A dynamically oriented view holds that during the haze season (winter and spring), meridional transport from mid-latitude source regions to the Arctic is stronger due to vigorous large-scale circulation. The presence of Siberian high pressure helps steer polluted European air into the Arctic by transient and stationary eddies (Barrie, 1986; Iversen and Joranger, 1985). Using a Lagrangian particle dispersion model, Stohl (2006) has shown that in winter the diabatic cooling of air traveling over ice and snow facilitates penetration of the polar dome (surface of constant potential temperature) and transport to the Arctic lower troposphere. In contrast, pollution is diabatically transported to higher altitudes and diluted in summer (Klonecki et al., 2003). On the other hand, Ma et al. (2013) has shown that the circulation features do not have a strong effect on surface concentrations of Arctic BC in the Community Atmosphere Model.

Another mechanism that contributes to the seasonality of Arctic BC is the slower removal in winter. As a major sink term for aerosols, wet scavenging by precipitation (rain and snow) is modulated heavily by cloud microphysics. BC particles become effective ice nuclei (IN) only when the temperature is below ∼240 K (Friedman et al., 2011) and is thus not effectively removed by ice clouds. In mixed-phase clouds, the Bergeron process (i.e. evaporation of liquid droplets in the presence of ice crystals) releases aerosols contained in cloud droplets back into air (Cozic et al., 2008), so the wet scavenging in mixed-phase clouds is much less efficient than in liquid clouds. The low efficiency of ice cloud and mixed-phase cloud scavenging favors accumulation of aerosols at cold temperatures. Previous studies have found that different treatments of aerosol removal in models are a leading cause of the spread in simulated BC burdens. Improving the wet deposition scheme in models has been shown to significantly increase Arctic BC burdens in winter and thus result in better simulation of the seasonal cycle (e.g., Liu et al., 2011; Bourgeois and Bey, 2011; Browse et al., 2012; Wang et al., 2013). Dry deposition also has seasonal variations and is weaker in winter when the stable boundary layer inhibits turbulent mixing (Quinn et al., 2007). It, however, accounts for only a small portion of the total removal and affects mainly the surface concentrations of Arctic haze (Liu et al., 2011). Another key factor determining BC concentrations is the aging process, which refers to the transformation from hydrophobic to hydrophilic aerosols due to coating by soluble species (Petters et al., 2006). Only aged BC particles can act as cloud condensation nuclei (CCN) and be removed by in-cloud scavenging. As a result, the aging rate has a large effect on global BC concentrations and distributions. Previous studies have shown that incorporating microphysical process into treatment of the aging process yields a slower aging rate in winter and improves the models' capability in simulating the seasonal cycle of Arctic BC (Liu et al., 2011, 2016).

It is important to note that the aforementioned mechanisms (namely large-scale circulation, cloud microphysics and aging) are not mutually exclusive; they could all act to induce seasonality. Yet, the relative importance of these mechanisms in shaping the pronounced seasonal cycle of Arctic BC remains unclear. Although we have a general understanding of how air pollution is transported from mid-latitudes to the Arctic, transport of BC into the Arctic has not been quantified in the literature. On the other hand, most of the current modeling studies confirm the importance of wet deposition by investigating the sensitivity of simulated BC concentrations to different removal schemes. This approach, however, does not rule out the potential influence of transport on the seasonality of Arctic BC. In this paper we seek to provide a comprehensive analysis of the roles of long-range transport and wet removal in controlling the seasonal cycle of Arctic BC by quantifying BC budgets in the Arctic.

## 2.2 Model Description

This study uses a modified version of the Geophysical Fluid Dynamics Laboratory (GFDL) AM3 atmospheric general circulation model (AGCM) (Donner et al., 2011) with a cubed-sphere grid resolution of ∼100 km and 48 hybrid vertical levels from the surface to ∼1 Pa. We conduct a six-year hindcast simulation (2008-2013), following one year of spin-up. The emission inventories reflect 2008-2013 conditions. Anthropogenic emissions of aerosol and ozone precursors with seasonal variations are based on Hemispheric Transport of Air Pollution (HTAP) v2 - a mosaic of regional and global emission inventories for the years from 2008 to 2010 (Janssens-Maenhout et al., 2015), and are held constant after 2010. Daily-resolving biomass burning emissions for 2008-2013 are adopted from the Fire Inventory from National Center for Atmospheric Research (NCAR) (Wiedinmyer et al., 2011) and emitted in the surface layer. The model is forced with observed sea surface temperatures and sea ice, and

horizontal winds are nudged to the National Centers for Environmental Prediction (NCEP) Global Forecasting System reanalyses at approximately $1.4^\circ \times 1.4^\circ$ horizontal resolution using a pressure-dependent nudging technique (Lin et al., 2012). The latter makes it possible to compare model simulations with observations for specific flight campaigns.

AM3 uses a bulk aerosol scheme and calculates the mass of aerosols based on their emissions, chemical reactions, transport, and wet and dry deposition, as described by Donner et al. (2011). Here we describe briefly the treatment of wet deposition, which is most pertinent to this study. In AM3, all aerosols are treated as externally mixed, and prescribed lognormal size distributions are assumed for computing aerosol activation into cloud droplets. Wet deposition includes in- and below-cloud scavenging by large-scale and convective clouds. For in-cloud scavenging of hydrophilic aerosols, the removal rate is equal to the scavenging efficiency (i.e. the fraction of aerosols that is incorporated into cloud droplets or ice crystals and removed by precipitation) multiplied by the fractional conversion rate of cloud condensate to precipitation. The scavenging efficiency is prescribed for each aerosol type, with consideration of its solubility. In AM3, in-cloud scavenging does not depend on size explicitly. Below-cloud scavenging is considered only for large-scale precipitation and is parameterized following Li et al. (2008).

The treatment of BC in the modified AM3 used in this study has been discussed extensively by Liu et al. (2011) and Fan et al. (2012); here we summarize briefly the key features. The model includes two types of BC: hydrophobic (BCpo) and hydrophilic (BCpi). 80% (40%) of BC emitted from anthropogenic (biomass burning) sources is assumed to be hydrophobic. The hydrophobic BC is then converted to the hydrophilic form at a variable aging rate (Liu et al., 2011). BC aging is assumed to result primarily from the condensation of $H_2SO_4$ onto BC aerosol surface, a common process that has been examined extensively in observational and laboratory studies.

$H_2SO_4$ is produced from the gas-phase oxidation of $SO_2$ by the OH radical and is rapidly converted to aerosol phase via nucleation or condensation onto existing particles. If it is assumed that during the transport of a plume, mixing with ambient air dilutes the concentrations of $SO_2$ and aerosols at the same rate, one can treat their ratio as a constant. As such, the aging rate is parameterized to be proportional to OH concentrations only, with the implicit assumption that there are always $SO_2$ and aerosol surface available for $H_2SO_4$ production. Aging can also occur through other processes (e.g. coagulation), which are believed to be slower and less important than condensation during long-range transport (Oshima et al., 2009). Their collective effect is represented by adding a small constant term to the parameterized aging rate coefficient. The final form of the aging process is:

$$k_a = \beta \cdot [OH] + \delta, \tag{2.1}$$

where $k_a$ is the aging rate coefficient, and $\beta$ and $\delta$ controls the fast and slow aging processes, respectively. In AM3 $\beta$ (which takes into account the effects of $SO_2$ and aerosol surface) is set to yield an e-folding aging time of 2.5 days under global mean OH concentrations, and $\delta$ is set by assuming a fixed e-folding time of 20 days for the slow aging processes.

Only hydrophilic BC can be removed by in-cloud scavenging, which is parameterized using a first-order rate coefficient ($k_{scav}$, $s^{-1}$) (Fan et al., 2012):

$$k_{scav} = \frac{F_{scav,1}P_{rain} + F_{scav,2}(1 - f_{berg})P_{snow} + F_{scav,3}f_{berg}P_{snow}}{Q_{liq} + Q_{ice}}, \tag{2.2}$$

where $P_{rain}$ and $P_{snow}$ are the 3-dimensional rain and snow rates (kg $m^{-3}$ $s^{-1}$), respectively, and $Q_{liq}$ and $Q_{ice}$ the liquid and ice cloud water contents (kg $m^{-3}$), respectively. $F_{scav,i}$ is the scavenging efficiency for precipitation type $i$ ($i$ =1, 2, 3). $f_{berg}$ is the fraction of snow produced by the Bergeron process. In this study, $F_{scav,1}$ and $F_{scav,2}$ are

set to 0.2, and $F_{scav,3}$ is set to 0.01 to account for the less efficient removal of aerosols by snow produced by the Bergeron process than by rain and snow produced by riming and homogeneous freezing. Both hydrophobic and hydrophilic BC can be removed by below-cloud scavenging and dry deposition. The dry deposition velocity is calculated using the empirical resistance-in-series method with a surface-dependent collection efficiency (Gallagher, 2002), resulting in a much smaller dry deposition velocity over snow and ice than over land surfaces (soils and canopy).

Table 2.1 shows AM3 simulated global and Arctic BC budgets. The global BC emission (7.5 Tg $yr^{-1}$) is close to the commonly used values of the industrial-era emission in the Aerosol Comparisons between Observations and Models (AeroCom) project (Schulz et al., 2006) and is within the range of 4.7-11.4 Tg $yr^{-1}$ in previous studies. The ratio of wet deposition to dry deposition of BC is 1.14, which lies toward the lower end of the published range (e.g., Koch, 2001; Koch and Hansen, 2005; Wang et al., 2014a). This may be related to the weak convective removal of aerosols in AM3 (Paulot et al., 2016), an issue that does not have a direct effect on wet deposition in the Arctic where large-scale precipitation dominates. It, however, may result in stronger high-altitude transport of aerosols in AM3 than in other models. The global mean column burden of BC (0.31 mg $m^{-2}$) is roughly in the middle of the range of previous model estimates (0.11-0.53 mg $m^{-2}$, Bond et al., 2013). Relatively few studies have provided BC budget terms in the Arctic. Local BC emissions are very small as expected. The Arctic mean BC column burden in AM3 (0.12 mg $m^{-2}$) is very similar to that estimated with the Community Atmosphere Model in a recent study (0.13 mg $m^{-2}$, Jiao and Flanner, 2016). Wet deposition accounts for more than 85% of the total sink of BC in the Arctic, consistent with previous studies which have shown that wet deposition is the dominant removal pathway of aerosols in remote regions (e.g., Huang et al., 2010; Wang et al., 2014a).

## 2.3 Simulated and observed seasonal cycle of Arctic BC

While the model treatment of aerosol transport and deposition processes has been improved considerably in recent years and most current models can qualitatively reproduce the seasonal variations of Arctic BC, large biases remain in the amplitudes of simulated seasonal cycles (Shindell et al., 2008; Eckhardt et al., 2015). Figure 2.1 shows AM3 simulated and observed monthly mean BC surface concentrations at Alert, Barrow, and Zeppelin (Eleftheriadis et al., 2009; Sharma, 2004; Sharma et al., 2006). Measured BC exhibits similar seasonal variations at all three stations. Its concentrations peak in winter or early spring, followed by a rather precipitous decrease in April and May. The lowest concentrations occur from June to October. On average, BC concentrations in winter (DJF) are higher than in summer (JJA) by a factor of 3-4. The model is able to capture the seasonal cycle, but appears to underestimate BC at Alert and Barrow by a factor of 2-3 throughout the year. The performance of AM3 in simulating surface BC in the Arctic is comparable to the models in the Arctic Monitoring and Assessment Programme (AMAP), which underestimate BC at Alert and Barrow by about a factor of 2 on average, with largest biases during the haze season (Eckhardt et al., 2015). The discrepancy between AM3 and observations may result from model deficiencies, including uncertainties in BC emissions and deposition, or from observational errors, as some of the measurements are indirect and may be subject to rather large biases (Bond et al., 2013).

Figure 2.1 also compares the simulated BC vertical profiles at high latitudes (66°-85°N) with the aircraft measurements made during the HIAPER Pole-to-Pole Observations (HIPPO) campaigns (Schwarz et al., 2013; Wofsy, 2011). The seasonal variations are evident in the data. In January, high concentrations of BC are confined within the boundary layer (HIPPO1). During early spring, there are enhancements of

BC at higher altitudes (HIPPO3). BC concentrations at all altitudes start to decrease in June, and remain low throughout summer (HIPPO4 and HIPPO5). Despite some mismatches, AM3 generally reproduces the seasonal variations in BC vertical profiles. Previous studies have found no systematic bias in model simulated free troposphere BC when compared with aircraft observations (e.g., Koch et al., 2009; Eckhardt et al., 2015). Yet comparisons of BC vertical profiles are limited by a lack of spatial and temporal coverage of aircraft campaigns, and additional observations are needed for further model validation.

Based on the above results, we conclude that despite the remaining discrepancies between the model and observations, the performance of AM3 in simulating Arctic BC is similar to that of the current generation of models. AM3 is capable of reproducing the seasonal cycle of Arctic BC and thus can be used to study its underlying mechanisms. The improvement in AM3 simulated Arctic BC [compared to the standard version in Donner et al. (2011)] is attributed to the modified BC-related processes (aging, wet removal and dry deposition) in the model, and Liu et al. (2011) discussed the sensitivity of BC simulation to each process in detail. Since observations show similar seasonality of Arctic BC at the surface and in the free troposphere, we will focus on the BC column burden averaged over the Arctic for the rest of the paper. This allows us to take full advantage of the model and generalize the results to the entire Arctic. The column burden is also more relevant to the radiative effects of BC than the surface concentrations, and has received much attention in the literature.

## 2.4 Controlling factors of Arctic BC

We employ a box model of the Arctic region to quantify the key factors controlling Arctic BC concentrations. Given the relatively small emissions from local sources, the prevailing balance is between the meridional BC transport into the Arctic and

local deposition. One can write the rate of change in the average BC column burden ($C$, kg m$^{-2}$) as:

$$\frac{dC}{dt} = \frac{F}{S} - W - D, \tag{2.3}$$

where $F$ is the total net meridional flux into the Arctic (kg s$^{-1}$), $S$ the Arctic surface area (m$^2$), and $W$ and $D$ the average wet and dry deposition rates (kg m$^{-2}$ s$^{-1}$), respectively. Note that $F$ includes transport into and out of the Arctic. Since the dry deposition of BC and the below-cloud scavenging of BCpo in the Arctic region are small (around 10% of the total BC deposition in the Arctic in the model simulation, see Table 2.1) and can be neglected, Eq. (2.3) can be simplified as:

$$\frac{dC}{dt} = \frac{F}{S} - W_{pi}, \tag{2.4}$$

where $W_{pi}$ is the average BCpi wet deposition rate (kg m$^{-2}$ s$^{-1}$). $W_{pi}$ can be written as $r{\cdot}w{\cdot}C$, where $r$ represents the dimensionless hydrophilic fraction of BC ($C_{pi}/C$, $C_{pi}$ being the average BCpi column burden) and $w$ represents the wet deposition efficiency of BCpi ($W_{pi}/C_{pi}$, s$^{-1}$), which can be thought of as the BCpi concentration-weighted in-cloud scavenging rate coefficient ($k_{scav}$) defined in Eq. (2.2), and is different from the wet scavenging efficiency ($F_{scav,i}$). Here $r$ and $w$ are derived from column-integrated quantities, and require no assumption regarding the vertical distributions of BCpi and BCpo. As AM3 simulated residence time of Arctic BC ranges from 6-20 days depending on the season (not shown), we assume steady state on the monthly time scale and arrive at an expression for $C$:

$$C = \frac{F}{S \cdot r \cdot w}. \tag{2.5}$$

An inspection of Eq. (2.5) suggests that elevated BC concentrations could result from stronger transport from mid-latitude source regions and/or weaker wet

removal. General circulation patterns are important for determining long-range transport fluxes. Wet removal is reduced when a smaller fraction of BC is hydrophilic or the wet deposition efficiency of BCpi is lower. The aging process exerts a strong control over the hydrophilic fraction. The wet deposition efficiency is affected mainly by the phase of precipitation because in-cloud scavenging efficiency differs among liquid, ice and mixed-phase clouds.

We apply the box model to quantify the roles of the three main variables, namely the meridional BC flux ($F$), BC hydrophilic fraction ($r$) and BCpi wet deposition efficiency ($w$), in controlling the seasonality of Arctic BC. The monthly mean values of $F$, $r$ and $w$ averaged over the Arctic (defined as poleward of 66°N) are computed from our AM3 model simulation. Figure 2.2a compares the monthly mean BC column burdens calculated using the box model with AM3 simulations. The good agreement validates the assumptions made in deriving Eq. (2.5). The box model captures the seasonal cycle, suggesting that one can rationalize the seasonality of Arctic BC by examining the three variables defined above.

## 2.5 Meridional transport

Like other anthropogenic aerosol species, BC is emitted mainly at the mid-latitude industrial regions and carried into the Arctic by atmospheric transport. Isentropic airflow facilitates high-level transport from warm and humid (high equivalent potential temperature, $\theta_e$) areas such as North America and East Asia, and low-level transport from comparatively low $\theta_e$ areas such as Europe (Stohl, 2006). Cross-isentropic transport due to diabatic heating or cooling also plays an important role (Klonecki et al., 2003). The total meridional BC flux ($F$) can be decomposed into contributions from

the mean meridional circulation (MMC), stationary eddies, and transient eddies:

$$\{\overline{vc}\} = \underbrace{\{[\overline{v}][\overline{c}]\}}_{MMC} + \underbrace{\{\overline{v}^*\overline{c}^*\}}_{stationary\ eddies} + \underbrace{\{\overline{v'c'}\}}_{transient\ eddies}, \tag{2.6}$$

where $v$ is the meridional wind velocity (m $s^{-1}$), and $c$ the BC mass mixing ratio (kg $kg^{-1}$). Overbars denote monthly means, square brackets zonal means, primes deviations from monthly means, asterisks deviations from zonal means, and curly brackets zonal and vertical integrals (from the surface to ∼100 hPa). Figure 2.2b shows the annual cycle of the total monthly mean meridional BC flux into the Arctic (at 66°N) and its three components. Generally, the total BC flux does not show much variation with time. The average flux is only ∼20% higher in DJF than in JJA, far from sufficient to account for the column burden difference between the two seasons (Fig. 2.2a). The contribution of the mean meridional circulation is very small. The transport is realized almost entirely by the eddy components. The flux by stationary eddies is comparable to that by transient eddies in DJF, while the latter dominates in JJA.

Although the vertically integrated BC flux changes little throughout the year, its vertical structure does vary with the season (Fig. 2.3). The flux in DJF is characterized by two peaks (one in the boundary layer, and the other at about 500 hPa), which are of different origins. In winter the polar dome extends to about 40°N, allowing the low-level transport of BC from Europe (Stohl, 2006). The diabatic cooling occurring when relatively warm air travels over a cold surface (i.e. strong inversion) keeps European BC in the boundary layer. The flux at about 500 hPa is more likely to be a result of transport from lower-latitude regions such as East Asia and North America. In JJA when BC from all regions experiences diabatic heating and wet removal caused by precipitation, the flux has only one notable peak at about 800 hPa originating from anthropogenic emissions in Europe and boreal forest fires over

Eurasia. BC from North America and East Asia is more likely to be transported diabatically to higher altitudes, and diluted and rained out along the path to the Arctic (Klonecki et al., 2003).

We further explore the meridional BC flux in frequency space by applying a time filter. Since the mean meridional flux is negligible, $\{\overline{v_n c_n}\}$ approximates BC transport carried out by eddies with time scales greater than $2n$ days (Hall et al., 1994). Note that the subscript $n$ denotes means of consecutive non-overlapping $n$-day periods. Figure 2.4 shows the time-filtered BC flux into the Arctic as a fraction of the total flux. The relative contributions from eddies of different frequencies to the total BC transport are different in the two seasons. In DJF, about 90% of the BC flux is realized by eddies with time scales longer than 10 days. Slightly more than 40% of the BC flux arises from eddies that persist longer than 60 days. In contrast, eddies with time scales longer than 10 days account for less than 50% of the JJA flux, and eddies that persist longer than 60 days have very little contribution to the total flux. Thus, while synoptic eddies dominate in JJA, low frequency eddies contribute substantially to the total transport in DJF.

The prominence of transient eddies in all seasons suggests that the long-range transport of Arctic haze can be represented, to first order, as turbulent diffusion of mid-latitude sources, despite the complexities at the process level (Shaw, 1981). The idea of simplifying eddy transport as turbulent diffusion is widely used in understanding the atmospheric transport of heat and potential vorticity (Held, 1999). Here we apply it to study tracer transport. For a local down-gradient diffusion process, the vertically integrated meridional transient eddy BC flux can be assumed to be proportional to the meridional gradient of the BC column burden:

$$\{\overline{v'c'}\} = -D\frac{\partial}{\partial y}\{\bar{c}\}, \tag{2.7}$$

where D is the turbulent diffusivity. It is clear from Figure 2.5 that there is a strong negative correlation ($r = -0.75$) between the transient eddy flux and meridional gradient averaged at a number of latitudes between 40°-66°N, which validates the diffusive picture of pollution transport. The magnitude of the slope of the best linear fit with zero intercept ($2.24 \times 10^6$ m$^2$ s$^{-1}$) represents the eddy diffusivity, which is within the range of the estimated values in previous studies (e.g., Bolin and Keeling, 1963; Newell et al., 1969; Held, 1999). While BC sources and sinks vary throughout the year, the eddy diffusivity does not change substantially with the season. This indicates that the diffusivity is intrinsically determined by atmospheric dynamics rather than specific tracer properties. It would be interesting to see whether this result is robust across different models.

It should be noted that besides the large-scale circulation patterns, BC emissions also play a role in determining the BC flux into the Arctic. Most of the Arctic BC comes from anthropogenic emissions from mid-latitude industrial regions and biomass burning emissions from boreal forest, which have opposite seasonal variations. Anthropogenic emissions are highest during the heating season from November to March, while biomass burning emissions are highest from April to August. The total BC emission in mid- to high latitudes used in this study has a weak seasonal cycle with a maximum in April and a minimum in September (not shown). This explains some of the difference in the total BC flux between spring and autumn (Fig. 2.2b).

## 2.6 Hydrophilic fraction

Figure 2.6a (solid line) shows the monthly mean hydrophilic fraction ($r$) of Arctic BC, which has a pronounced seasonal cycle. The hydrophilic fraction in DJF is only ∼40%, while almost all BC is hydrophilic in JJA. Figure 2.6a (dashed line) shows the monthly mean hydrophilic fraction of the meridional BC flux into the Arctic (i.e. the

ratio of BCpi flux to total BC flux), which is very similar to that of Arctic BC. This indicates that the transformation from hydrophobic to hydrophilic BC occurs mainly during the long-range transport, and the seasonal cycle of the Arctic BC hydrophilic fraction is shaped mainly by the aging process along the long-range transport path rather than locally in the Arctic.

Figure 2.6b shows the monthly mean e-folding aging time of BC (the inverse of the aging rate coefficient, computed as the average BCpo concentration divided by the average conversion rate from BCpo to BCpi) at 40°-66°N and over the Arctic. During the transport from mid-latitudes to the Arctic, the average aging time is much longer in DJF (∼10 days) than in JJA (∼1 day), resulting in a substantially lower hydrophilic fraction in winter. In the Arctic, the seasonal variations of BC aging time are even greater, which further amplifies the seasonal cycle of the hydrophilic fraction, as shown by the difference between the solid and dashed lines in Figure 2.6a.

The parameterized aging scheme in the model (Section 2) accounts for the seasonal cycle of the aging process and thus the hydrophilic fraction. The aging rate due to condensation is proportional to OH concentrations. As a result of enhanced solar radiation and specific humidity, OH concentrations are much higher in JJA than in DJF, resulting in more rapid aging by condensation in summer. The aging occurring through other processes (e.g. coagulation) is assumed to have a fixed e-folding time of 20 days, which is longer than that for the aging via condensation during the long-range transport (Fig. 2.6b, dashed line), and thus do not contribute to the seasonal cycle of the hydrophilic fraction.

The change in the hydrophilic fraction also helps explain the change in Arctic BC during spring and fall. From October to November, there is a sharp decrease in the hydrophilic fraction, resulting in a rapid buildup of BC. Similarly, from March to April, the increase in the hydrophilic fraction contributes to the decline in BC concentrations. The hydrophilic fraction, however, is fairly constant from April to

September, in contrast with the continuous decrease in BC starting from April. The wet deposition efficiency plays an important role in driving BC changes during this time period, as discussed in the next section.

## 2.7 BCpi wet deposition efficiency

Figure 2.6c shows the monthly mean wet deposition efficiency of BCpi ($w$) in the Arctic. The wet deposition efficiency in JJA is ∼20% higher than in DJF, contributing to the lower BC in JJA than in DJF. The magnitude of its seasonal cycle, however, is much weaker than that of the hydrophilic fraction ($r$) (Fig. 2.6a). Yet, the wet deposition efficiency increases continuously by a factor of 2 from May to August, driving the transition from moderate BC burdens in late spring to exceedingly low burdens in summer.

The wet deposition efficiency is largely controlled by the in-cloud scavenging rate coefficient [$k_{scav}$ in Eq. (2.2)]. To better understand the factors determining $k_{scav}$, we analyze the conversion rate coefficients of cloud condensate to rain ($k_{rain}$) and snow ($k_{snow}$) through which in-cloud scavenging occurs, which are defined as:

$$k_{rain} = \frac{P_{rain}}{Q_{liq} + Q_{ice}},\ k_{snow} = \frac{P_{snow}}{Q_{liq} + Q_{ice}}. \tag{2.8}$$

In this study we use a much larger scavenging efficiency for rain than for snow produced by Bergeron process. Therefore according to Eq. (2.2), $k_{scav}$ and thus the wet deposition efficiency are determined by $k_{rain}$ rather than $k_{snow}$ when most snow is produced by the Bergeron process, which is the case for the Arctic during the winter (Fan et al., 2012). Figure 2.6d shows the annual cycle of AM3 simulated $k_{rain}$ and $k_{snow}$ in the Arctic. [$P_{rain}$, $P_{snow}$, $Q_{liq}$ and $Q_{ice}$ are first averaged over the Arctic and then $k_{rain}$ and $k_{snow}$ are calculated using Eq. (2.8).] Consistent with the seasonal cycle of the wet deposition efficiency, $k_{rain}$ is higher in JJA than in DJF. From May to

August, $k_{rain}$ increases by a factor of 2, which helps explain the two-fold increase in the wet deposition efficiency. The seasonal variation in $k_{rain}$ is a result of the seasonal cycle of both rain rate ($P_{rain}$) and cloud water content ($Q_{liq} + Q_{ice}$). As the atmosphere becomes warmer and holds more water vapor from DJF to JJA, $P_{rain}$ increases by about an order of magnitude (Fig. 2.6e) due to thermodynamic reasons. However, $k_{rain}$ and the wet deposition efficiency increase by only less than a factor of two. This is because $Q_{liq} + Q_{ice}$ increases by a factor of 4-5 (Fig. 2.6f) from DJF to JJA as the clouds become more vigorous, and the wet deposition efficiency is determined by the ratio of $P_{rain}$ to $Q_{liq} + Q_{ice}$ rather than by $P_{rain}$ alone.

In contrast with $k_{rain}$, $k_{snow}$ is much larger in DJF than in JJA because cold temperature favors snow formation, which is opposite to the seasonal variations in the wet deposition efficiency. Therefore one may expect that models without different removal efficiencies for liquid and mixed-phase clouds cannot reproduce the seasonal cycle of the wet deposition efficiency, and thus the seasonal cycle of Arctic BC concentrations.

It should be noted that as clouds get warmer and contain more liquid water from DJF to JJA, riming overtakes the Bergeron process as the main mechanism for generating snow in the Arctic. In AM3 riming accounts for about 20% and 80% of the total Arctic snow production in DJF and JJA, respectively (not shown). In this study riming is assumed to be as efficient at removing aerosols as rain. The change in the mechanism of snow production, however, does not have a strong effect on the seasonal cycle of the wet deposition efficiency. Since $k_{snow}$ is larger in DJF than in JJA by almost an order of magnitude (Fig. 2.6d), the conversion rate coefficient of cloud condensate to snow produced by riming (i.e. $k_{snow}$ scaled by the riming fraction) reaches a maximum in winter, despite much higher riming fraction in summer. The conversion of cloud condensate to rain is much faster than to snow in summer, indicating that rain is the dominant removal mechanism. As a result, we conclude

that the difference in the scavenging efficiency between rain and snow is the primary cause of the seasonal cycle of the wet deposition efficiency, and the change in the dominant mechanism of snow production is a secondary consideration.

## 2.8 Concluding remarks

It has long been recognized that aerosols from mid-latitude source regions undergo long-range transport, leading to high concentrations of air pollution in the Arctic during late winter and early spring. Here we apply the GFDL AM3 model to analyze the key factors affecting the seasonal variations in Arctic BC. The model is able to reproduce the observed Arctic BC concentrations and seasonality, with 3-4 times higher values in DJF than in JJA. We find that the seasonal cycle of Arctic BC is caused mainly by the seasonality of wet deposition, with a secondary contribution from the long-range transport flux.

The transport of BC at mid- to high latitudes occurs mainly through stationary and transient eddies, rather than through the mean meridional circulation. Stationary eddies account for $\sim$40% of the total flux in DJF, while virtually all the transport is realized through transient eddies in JJA. The vertical distribution of meridional BC transport also varies seasonally. The vertical profile of the BC flux into the Arctic in DJF has two peaks (one in the boundary layer and the other in the mid-troposphere), while the BC flux in JJA is concentrated in the lower troposphere. The total meridional BC flux into the Arctic, however, changes little throughout the year despite the shift in large-scale circulation.

The wet removal depends on both BC hydrophilic fraction and BCpi wet deposition efficiency. The hydrophilic fraction is smaller in DJF than in JJA due to the slower BC aging along the long-range transport path to the Arctic during winter. This difference in the hydrophilic fraction plays a dominant role in the large difference in

BC concentrations between DJF and JJA. The wet deposition efficiency is lower in DJF mainly because snow produced in mixed-phase clouds is less efficient in removing BC than rain. The decrease in BC concentrations from late spring to summer is due to a gradual but steady increase in the wet deposition efficiency, while the return of BC in late autumn is caused mainly by a sharp decrease in the hydrophilic fraction.

Our results are consistent with the observational analysis of Garrett et al. (2011), which argued that some combination of dry deposition and wet scavenging drives the seasonal cycle of aerosols at low altitudes in the North American Arctic. Here we show that the dominance of wet deposition in determining BC seasonal cycle applies to the entire Arctic. We further explain the seasonality of wet deposition in terms of aging and cloud microphysical processes. While being influenced by complicated physical and chemical factors, these processes are parameterized in the model in a relatively simple way. Measurements of Arctic BC mixing state at different times are required for verifying the assumed OH dependence of the aging rate. Measurements of BC wet deposition and concentrations in rain and snow will be particularly useful for constraining the rain and snow scavenging efficiencies. It should also be noted that besides transport and wet deposition, large uncertainties remain in BC emission inventories, which have not been discussed in this paper. High latitude BC emissions from gas flaring and residential combustion have a large contribution to Arctic BC concentrations and are potentially crucial for affecting its seasonality (Stohl et al., 2013). Although these sources are included in HTAP emissions, the low biases in model simulated BC surface concentrations at Alert and Barrow suggest an underestimate of BC emissions at high latitudes. However, as most of the emissions remain close to the surface, their contributions to BC in the mid-and upper troposphere in the Arctic are small (Stohl et al., 2013), and will not affect our conclusions, which are based on BC column burden.

In this study the quantitative analysis of the controlling factors is for BC column burden, as opposed to surface concentration. While they share a similar seasonal cycle, the relative importance of the controlling factors is somewhat different. As shown in Figure 2.3, the BC flux in the boundary layer (below 900 hPa) in winter is 2-3 times larger than that in summer, contributing to higher surface concentrations. Furthermore, a sensitivity test (not shown) suggests that dry deposition is a very important controlling factor of BC surface concentrations, while wet deposition plays less of a role than it does in causing high BC column burdens in winter.

Although the analysis in this paper focuses on BC, the findings should be generally applicable to other components of Arctic haze. For example, sulfate has a similar seasonal cycle, but with peak concentrations in spring as opposed to winter (as is the case for BC) (Shindell et al., 2008). The difference in the scavenging efficiencies by rain and snow probably dominates the seasonal variations in sulfate. Reducing wet deposition by snow has been found to improve the model's ability to reproduce the observed sulfate concentrations over the United States (Paulot et al., 2016) and in the Arctic (Browse et al., 2012). The shift in the peak may be due to the absence of an aging process since all sulfate is hydrophilic. The seasonal cycle of sulfate production by $SO_2$ oxidation may also plays a role in shaping the high sulfate concentrations in spring.

The results discussed here may have implications for understanding the variability and trend in Arctic aerosols and their climate impacts. Since large-scale circulation influences the key processes of long-range transport and the spatial pattern of precipitation, natural climate variability at annual to decadal timescales may play an important role in determining changes in aerosol concentrations in the Arctic (Christoudias et al., 2012; Eckhardt et al., 2003). It would be interesting to apply our analysis to study the effect of climate variability on the characteristics of atmospheric transport and wet deposition. As climate warms, precipitation at high latitudes is

expected to increase, but the fraction of snow may decrease (Barnett et al., 2005; Singarayer et al., 2006). These changes tend to enhance the wet scavenging of aerosols and result in a cleaner Arctic atmosphere. A recent study has shown that with constant BC emissions, the annual mean Arctic BC burden will be reduced by 13.6% by the end of the 21st century due to the enhanced wet removal in a warmer climate (Jiao and Flanner, 2016). The aging process, which is affected by atmospheric composition, may also vary over time. $SO_2$ emissions at mid-latitudes have generally declined in recent decades (Streets et al., 2006) and are projected to decrease even more in the future (Levy et al., 2008). This long-term trend in $SO_2$ emissions will result in a decrease in sulfate concentrations but an increase in BC concentrations in the Arctic due to a slower aging process by condensation of $H_2SO_4$ and thus weaker wet removal. Therefore it is important to consider the changes in aerosol sources and sinks when using models to examine how aerosols may alter Arctic climate under future emission scenarios.

Table 2.1: Global and Arctic annual mean BC budgets in AM3.

| | Emission ($Tg\ yr^{-1}$) | Wet Deposition ($Tg\ yr^{-1}$) | Dry Deposition ($Tg\ yr^{-1}$) | Burden ($mg\ m^{-2}$) |
|---|---|---|---|---|
| Global | 7.5 | 4.0 | 3.5 | 0.31 |
| Arctic | 0.0052 | 0.078 | 0.012 | 0.12 |

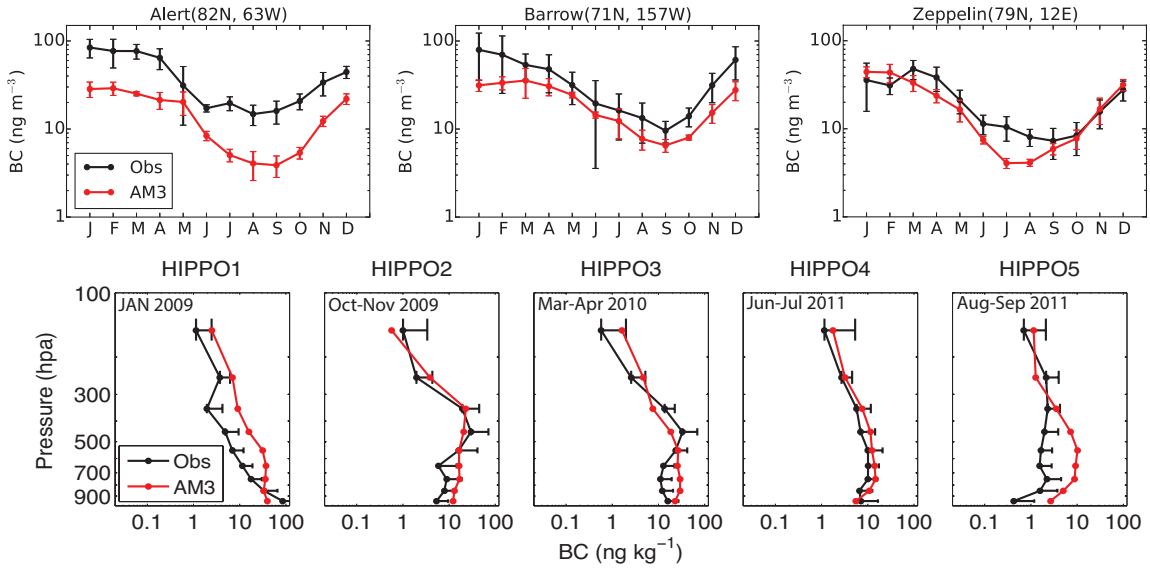



Figure 2.1: (top) Model simulated and observed monthly mean surface BC at Alert (2008-2012), Barrow (2008-2013), and Zeppelin (2008-2013). Error bars denote one standard deviation from monthly means. (bottom) Model simulated and observed BC vertical profiles at high latitudes (66°-85°N) during HIPPO (HIPPO1: January 2009, HIPPO2: October-November 2009, HIPPO3: March-April 2010, HIPPO4: June-July 2011, HIPPO5: August-September 2011). Error bars associated with observational profiles represent one standard deviation of the HIPPO data. For the comparison, daily BC fields archived from the model are first sampled along the flight track and then averaged over 66°-85°N for each campaign.

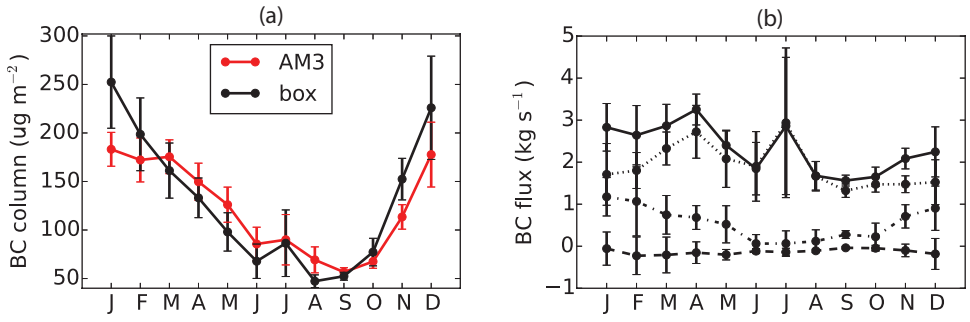



Figure 2.2: Monthly mean (a) Arctic BC column burdens simulated using AM3 (red) and derived from the box model (black), (b) AM3 simulated total meridional BC flux into the Arctic (solid) and contributions from the mean meridional circulation (dashed), stationary eddies (dash-dot), and transient eddies (dotted). Error bars denote one standard deviation from monthly means.

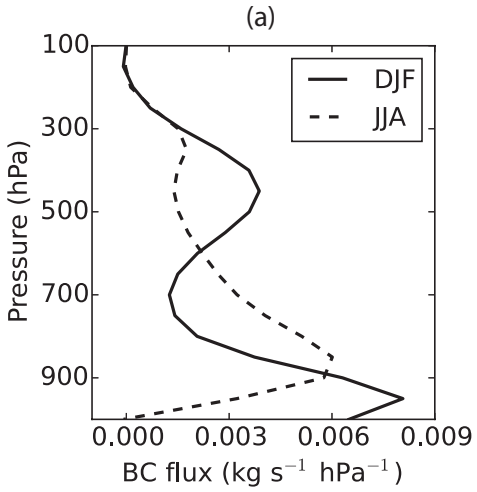



Figure 2.3: Vertical profiles of meridional BC flux at 66°N. The solid and dashed lines represent DJF and JJA, respectively.

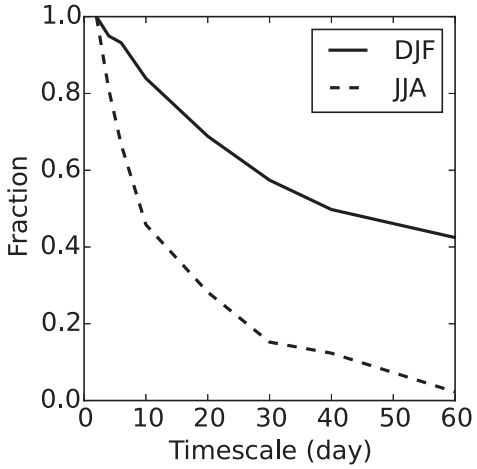



Figure 2.4: Time-filtered meridional BC flux ($\{\overline{v_n c_n}\}$ defined in Section 5) as a fraction of total flux at 66°N. The solid and dashed lines represent DJF and JJA, respectively.

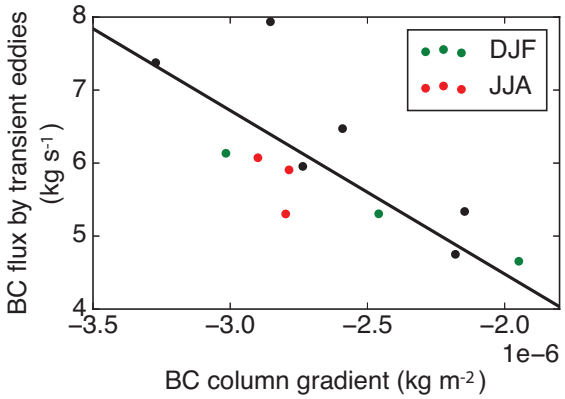



Figure 2.5: Scatter plot of vertically integrated monthly mean meridional BC flux by transient eddies versus meridional gradients of BC column burden averaged over 40°-66°N. The linear regression line is also shown. Green and red dots represent DJF and JJA, respectively.

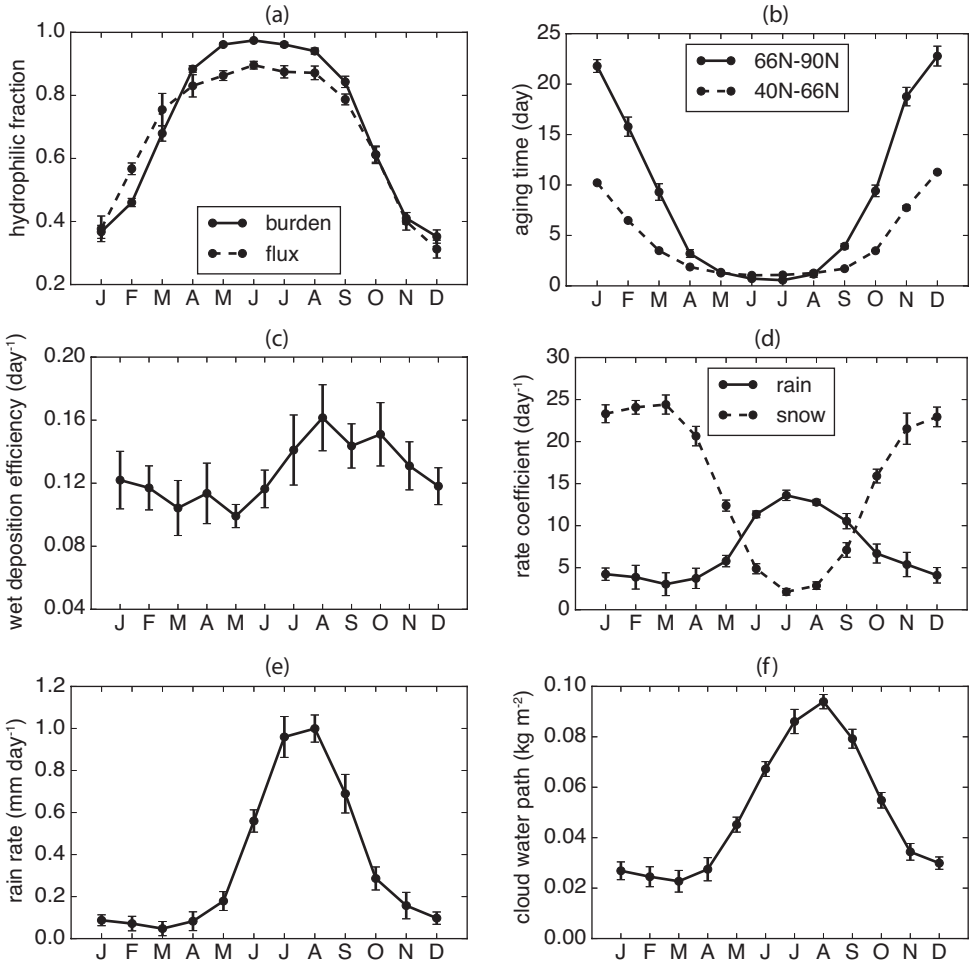



Figure 2.6: Monthly mean AM3 simulated (a) hydrophilic fractions of Arctic BC (solid) and BC flux into the Arctic (dashed), (b) BC aging time averaged at 66°-90°N (solid) and 40°-66°N (dashed), (c) Arctic BCpi wet deposition efficiency, (d) rate coefficients of conversion of cloud condensate to rain (solid) and snow (dashed) in the Arctic, (e) Arctic rain rate, and (f) Arctic cloud water path. Error bars denote one standard deviation from monthly means.

# Chapter 3

# The Influence of Aerosol Absorption on the Extratropical Circulation

## 3.1 Introduction

The large-scale atmospheric circulation response to climate forcings has been studied extensively. The greenhouse gas (GHG)-induced warming is thought to cause a poleward shift of the subtropical jets and storm tracks, and an expansion of the tropics (e.g., Hall et al., 1994; Yin, 2005; Lorenz and DeWeaver, 2007; Lu et al., 2008; Chen et al., 2008). Scattering aerosols (e.g., sulfate) can partly offset the climate impacts of GHGs by reflecting solar radiation. Previous studies using coupled general circulation models (GCMs) have shown the impacts of aerosols on both tropical and extratropical circulation. As a result of the interhemispheric asymmetry in the aerosol forcing, the Hadley circulation weakens (strengthens) in the boreal summer (winter) and the intertropical convergence zone shifts southward (Ming et al., 2011). Aerosol-induced cooling results in an equatorward shift of the jet stream, opposite to

the GHG-induced change (Fischer-Bruns et al., 2009; Ming and Ramaswamy, 2009). Allen and Ajoku (2016) showed that future projected aerosol decrease results in tropical widening and a poleward shift of the jet, and the effect of aerosol decrease may be larger than GHG increase in GCMs including aerosol indirect effect. Ming et al. (2011) suggested that aerosols also cause zonal-asymmetric circulation change at mid-latitudes by altering stationary Rossby waves, which results in a strong cooling and a decrease of transient eddy kinetic energy (EKE) over the North Pacific. On regional scales, aerosols have been shown to modify radiative heating rates at the surface and in the boundary layer in urban areas and thus affect the temperature profile (Ackerman, 1977; Jacobson, 1998). Jacobson and Kaufman (2006) suggested that aerosols tend to reduce near-surface wind speed and precipitation locally by stabilizing the atmosphere. Recent studies using atmospheric GCMs (AGCMs) have shown that anthropogenic aerosols also modulate mid-latitude cyclones by changing the vertical profile of diabatic heating rates in the atmosphere (e.g., Wang et al., 2014c,b; Lu and Deng, 2016).

Absorbing aerosols (e.g., black and brown carbon) have different radiative properties from scattering aerosols and contribute to global warming along with GHGs. Black carbon (BC) from fossil fuel emissions has been shown to increase the stability of near-surface air, slow near-surface winds, and reduce global mean precipitation (e.g., Jacobson, 2002, 2004; Ming et al., 2010). Some studies have suggested that controlling BC emissions may be more effective at slowing global warming than controlling GHG emissions (Jacobson, 2002, 2010). Recent work has focused on the effects of absorbing aerosols on regional climate (e.g., Bollasina et al., 2008; Randles and Ramaswamy, 2008). However, the impacts of absorbing aerosols on atmospheric circulation have received little attention. Allen et al. (2011) showed that the circulation response to natural (mostly scattering) and anthropogenic (scattering and absorbing) aerosols are very different and inferred that absorbing aerosols strongly

affect atmospheric circulation in an opposite way to scattering aerosols. While both absorbing aerosols and GHGs act to warm the climate, their effects on large-scale circulation are not necessarily similar. Ming et al. (2010) showed that the global mean precipitation increase due to the warming caused by absorbing aerosols does not scale with surface temperature change since the strong atmospheric absorption suppresses precipitation. Using the Community Atmosphere Model coupled to a slab ocean, Allen et al. (2012) showed that BC and tropospheric ozone play a more important role than GHGs in driving tropical expansion in the Northern Hemisphere in recent years due to the associated atmospheric heating at mid-latitudes and the resulting poleward shift of the maximum meridional temperature gradient. Despite these early attempts, the influence of absorbing aerosols on large-scale circulation has not been studied systematically.

In general, global emissions of BC have increased in recent decades while sulfate emissions have declined (Lamarque et al., 2010), and this trend is projected to continue over the next decade under several Representative Concentration Pathways (Lamarque et al., 2011; Fiore et al., 2012). This adds urgency to understanding the circulation response to absorbing aerosols for attributing the observed trend and variability in atmospheric circulation and predicting future changes. Satellite and in-situ observations shows that large amount of BC is present both in the tropics and at mid-latitudes (e.g., Koch et al., 2009; Schwarz et al., 2013). One would expect that the circulation response to the same forcing varies with latitude due to different dynamical regimes. In the tropics where the Coriolis parameter is small, the time mean flow is the largest contributor to the poleward energy transport. The vertical temperature structure (or the static stability) is set approximately by the moist adiabat. In the extratropics, baroclinic eddies play the dominant role in transporting heat and moisture poleward and shaping the large-scale circulation and weather pattern. The static stability is largely controlled by dry baroclinic eddy dynamics

(Held, 1982; Zurita-Gotor and Lindzen, 2007; Schneider and O'Gorman, 2008), while moisture has an important but secondary role (Frierson, 2008). In light of the very different tropical and extratropical regimes, in this study we choose to focus on the impacts of absorbing aerosols on the extratropical circulation and associated physical mechanisms.

The overall picture of aerosol-climate interactions is complicated and uncertain since it involves a variety of physical processes, such as aerosol emission and transport, aerosol-radiation interactions, aerosol-cloud interactions, and air-sea coupling. To simplify the problem, we use an AGCM to study tropospheric-only response to idealized absorbing aerosol forcings. Our analysis includes only aerosol direct and semi-direct effects. We examine the effects of absorbing aerosols at different altitudes since previous studies have shown that BC-climate interaction is highly dependent on the vertical profile (Hansen, 2005; Ming et al., 2010; Ban-Weiss et al., 2012; Persad et al., 2012).

## 3.2 Method

We use the Geophysical Fluid Dynamics Laboratory (GFDL) AM2, the atmospheric component of GFDL coupled model CM2, to investigate the atmospheric-only response to absorbing aerosols. The configuration and performance of this model have been documented in The GFDL Global Atmospheric Model Development Team (GAMDT, 2004); here we describe briefly the features most relevant to this study. AM2 uses a finite volume dynamical core with a horizontal resolution of $\sim 2^\circ \times 2.5^\circ$. The model has 24 hybrid vertical levels from the surface to 3 hPa, with nine levels in the planetary boundary layer (the lowest 1.5 km), ten levels in the free troposphere, and five levels in the stratosphere. The shortwave and longwave radiation algorithms follow Freidenreich and Ramaswamy (1999) and Schwarzkopf and Ra-

maswamy (1999), respectively, with modifications as described in GAMDT (2004). The model uses the relaxed Arakawa-Schubert (RAS) convective parameterization, which represents moist convection as multiple entraining plumes that produce precipitation (Moorthi and Suarez, 1992). Stratiform clouds are prognosed following Tiedtke (1993) with modifications as described in GAMDT (2004). Cloud microphysics are parameterized based on Rotstayn (1997) and Rotstayn et al. (2000). Convective planetary boundary layers are parameterized using a K-profile scheme based on Lock et al. (2000). For stable layers, conventional stability functions dependent on the Richardson number are used. Tropospheric aerosols and ozone are simulated offline using a chemical transport model driven by GCM-simulated meteorological fields (Horowitz, 2006). All aerosols are treated as externally mixed, and lognormal size distribution is assumed with the geometric mean radius and standard deviation from Haywood and Ramaswamy (1998). The model includes only the direct effects of aerosols with optical properties described by Haywood and Ramaswamy (1998) and Haywood et al. (1999). The model has been used to study the responses of general circulation and hydrological cycle to GHGs and aerosols (e.g., Ming et al., 2010; Persad et al., 2012).

We perturb the control case (with GHG and aerosol concentrations in 1990) with an increase of $2.4 \times 10^{-6}$ kg m$^{-2}$ in BC burden within a specific model layer over the entire globe. This burden is chosen so that the resulting radiative forcing is comparable to that of the present-day BC [approximately 0.53 W m$^{-2}$ in AM2 (Ming et al., 2010)]. The BC burden is prescribed and not interactive. The globally uniform increase in BC is not representative of present-day BC or any future scenario. Given large uncertainties in the realistic spatial distribution of aerosols, we choose to use these uniform absorbing aerosol experiments to investigate the underlying mechanisms through which the climate impacts are manifested. We examine the model-simulated response to increase of BC at three model layers in the free troposphere or

the boundary layer ($\sigma = 0.38$, 0.60, 0.90). To investigate to what extent the response is local, we also perform experiments with latitudinally restricted increase of BC in the tropics (30°S-30°N), mid-latitudes (30-60°N/S) and high latitudes (60-90°N/S) at $\sigma = 0.38$. The simulations are forced with monthly climatological sea surface temperatures (SSTs) and sea ice from the NOAA Optimal Interpolation sea surface temperature dataset (Reynolds et al., 2002). Each simulation is run for 17 years, and the results in this paper are averaged over the last 16 years.

We also conduct a set of idealized model experiments to complement the comprehensive model results. The idealized model is based on a spectral dynamical core. It uses a sigma coordinate, with the vertical differencing following Simmons and Burridge (1981). The model is dry (i.e., has no clouds or water vapor), and has neither topography nor seasonal cycle. It is forced with highly idealized physics as described in Held and Suarez (1994). Radiative heating and cooling are represented by Newton relaxation of temperature to a specified zonally symmetric radiative-equilibrium state. Momentum is damped by Rayleigh friction near the surface, the rate of which decreases linearly from 1 day$^{-1}$ at the surface to 0 at $\sigma = 0.7$. The model does not have parameterized convection. This dry idealized GCM has been used to study the response of tropospheric circulation to idealized forcings such as stratospheric warming, surface friction, and zonal torque (Chen et al., 2007; Lorenz and DeWeaver, 2007; Chen and Zurita-Gotor, 2008). We run the model with a horizontal resolution of T85 ($\sim 1.4°$) and 30 evenly spaced vertical levels, and perturb the control run by adding a global uniform heating rate of $3 \times 10^{-5}$ K s$^{-1}$ at specific levels. The heating rate is chosen to yield an anomalous column integrated heating rate similar to that induced by BC in the comprehensive model. This is done for two different layers in the free troposphere ($\sigma = 0.38$ and 0.58). The model is integrated for 1000 days for each experiment, and the last 500 days are used for analysis.

## 3.3 Results

### 3.3.1 Temperature and zonal wind

Figure 3.1 shows the responses of zonal mean temperature and zonal wind to BC at different levels. In general BC heats the troposphere by absorbing solar radiation, and the maximum warming occurs at heated altitudes. The temperature increase due to BC at higher altitudes is much stronger. Upper ($\sigma = 0.38$) and mid- ($\sigma = 0.60$) tropospheric BC yields a maximum warming of $\sim$6 K and $\sim$3 K, respectively, while the temperature change due to boundary layer ($\sigma = 0.90$) BC is less than 1 K. The magnitude of warming decays away throughout the troposphere, which stabilizes (destabilizes) the atmosphere below (above) the heating layer. The tropospheric warming penetrates to lower altitudes more in the mid-latitudes than in the low and high latitudes, indicating that the atmosphere responds differently in the three distinct dynamical regimes. More specifically, the tropical air temperature is under strong control of the surface temperature through moist convection; the latter is fixed in our simulations. The stable polar atmosphere is not conducive to vertical mixing. A detailed discussion of the mid-latitudes will be given later. Mid-tropospheric and boundary layer BC is more effective at exciting surface polar amplification. Free tropospheric BC also results in cooling in the polar stratosphere and warming near the tropopause in the tropics. These non-local responses may result from the stratospheric residual circulation change, which is out of the scope of this paper.

Upper tropospheric BC has a strong effect on both the subtropical jet and the eddy-driven jet, which merge together in the climatological control run (Figure 3.1d). There is an appreciable weakening of the zonal wind on the equatorward flank of the subtropical jet ($\sim$20°), which is accompanied by a strengthening on the poleward flank of the eddy-driven jet ($\sim$ 60°). If one defines the jet position as the latitude of maximum vertical averaged zonal mean zonal wind, this wind pattern change amounts

to a poleward jet displacement of $\sim 3^\circ$ in both hemispheres. The jet response is a result of changes in both the vertical wind shear and surface wind. The vertical shear decreases (increases) on the equatorward (poleward) flank of the jet, consistent with the anomalous meridional temperature gradient (Figure 3.1a). The poleward shift of surface westerlies is related to the change in eddy momentum flux, which is shown in Figure 3.2. In both hemispheres, the decrease (increase) in eddy momentum flux on the equatorward (poleward) flank of the jet gives rise to a divergence of eddy momentum flux at mid-latitudes, which slows down surface westerlies. In contrast, the convergence of eddy momentum flux poleward of $\sim 60^\circ$ acts to accelerate surface westerlies. The negligible jet displacement in the case of mid-tropospheric BC is likely due to the competing effects of the surface warming amplification at high latitudes and the upper tropospheric warming amplification in the tropics. This is consistent with previous studies focusing on the jet shift under global warming, which have shown that increased upper tropospheric meridional temperature gradient tends to shift the jet poleward while decreased lower tropospheric temperature gradient does the opposite (e.g. Barnes and Screen, 2015; Butler et al., 2010). The impact of boundary layer BC on zonal wind is similar to that of mid-tropospheric BC, albeit with an even smaller magnitude, especially in the Northern Hemisphere.

Figures 3.3a-c show the responses of zonal mean temperature in the latitudinally restricted perturbation experiments in which BC is increased at $\sigma = 0.38$ in the tropics, mid-latitudes and high latitudes, respectively. Increased BC at individual latitude bands yields maximum warming at the heated latitudes. To first order the temperature response is local; the warming is mostly confined in the forced latitudinal bands. It is notable that tropical BC also causes some dynamically induced warming at mid-latitudes. In contrast to the clear downward mixing in the mid-latitude case, the high latitude warming is almost entirely confined locally, a manifestation of the stable atmospheric condition in the polar regions. A comparison with Figure 3.1a

suggests that the temperature response to BC at different latitudes are mostly linearly additive.

Figures 3.3d-f depict the responses of zonal wind to the latitudinal restricted forcings, with corresponding changes in eddy momentum flux in Figure 3.4. The poleward jet displacement seen in the case of globally uniform BC can be attributed mostly to mid-latitude BC (Figure 3.3e). The resulting divergence (convergence) of eddy momentum flux decelerate (accelerate) surface westerlies equatorward (poleward) of 60°. Upper tropospheric wind anomalies are consistent with changes in the meridional temperature gradient and the associated vertical wind shear. The poleward jet shift due to mid-latitude BC is more prominent than that in the globally uniform case in the Southern Hemisphere. This is mainly because high-latitude BC has an opposite effect, reducing zonal wind on the poleward flank of the jet and yielding an equatorward jet displacement (Figure 3.3f). The opposite effects of mid- and high-latitude heating on the jet have also been found in GCM experiments with idealized thermal forcings at different latitudes (Allen et al., 2012). Tropical BC results in an anomalous poleward eddy momentum flux at the jet core in both hemispheres, which helps force the weakening (strengthening) of the surface wind near 30° (60°). In the upper troposphere the eddy-driven jet becomes stronger, consistent with the increased meridional temperature gradient as a result of tropical warming. In the Southern Hemisphere tropical BC also results in a slight poleward jet displacement, but mid-latitude BC is much more effective at shifting the jet.

### 3.3.2 Mean circulation and eddy activity

Figure 3.5 shows the response of the meridional overturning streamfunction to BC at different altitudes. Upper tropospheric BC results in a weakening and expansion of the Hadley cell in both hemispheres. The weakening occurs in the summer hemisphere of the solstice seasons and in both hemispheres of the equinox seasons (not

shown). This is related to the anomalous eddy momentum flux convergence in the upper troposphere at $\sim 20^\circ$ (Figure 3.2), consistent with the linear theories of Hadley circulation strength (e.g., Walker and Schneider, 2006). The Hadley cell expansion may be due to the increase in subtropical static stability (Figure 3.1a), as suggested by the existing scaling theories of Hadley circulation extent (e.g., Walker and Schneider, 2006; Lu et al., 2007). In the extratropics upper tropospheric BC results in a weakening of the Ferrel cell. This is consistent with the change in eddy momentum flux (Figure 3.2), as the anomalous divergence of the eddy momentum flux in the upper troposphere at mid-latitudes is balanced by the Coriolis torque acting on the anomalous poleward flow. Mid-tropospheric and boundary layer BC yields a similar weakening of the Hadley and Ferrel cells, but the magnitude is much smaller.

Atmospheric circulation plays an important role in transporting energy from equatorial regions to higher latitudes. This poleward energy flux occurs mainly through the mean meridional circulation, stationary eddies and transient eddies. Figure 3.6 shows the change in total northward energy flux due to BC at different altitudes and the contribution from each component. In the tropics the weakening of the Hadley cell due to free tropospheric BC results in a decrease in the poleward energy transport by mean circulation. In the extratropics free tropospheric BC causes a decrease in energy transport by transient eddies. The weakening of the energy transport occurs everywhere below the heating layer (Figures 3.7a,b). Overall, the poleward energy flux by transient eddies decreases by about 14% (5%) at mid-latitudes due to upper (mid-) tropospheric BC. In the Northern Hemisphere part of the decrease is balanced by an anomalous northward energy flux associated with the weaker Ferrel Cell (Figures 3.5a,b), but in general transient eddies dominate the weakening of poleward energy transport in both hemispheres. The stationary eddies have seasonal variations with opposite signs in summer and winter (not shown), and thus does not contribute to the change in annual mean meridional energy flux. The change in meridional energy

flux due to boundary layer BC is not statistically significant in most places (Figures 3.6c and 3.7c).

Since the poleward eddy transport of energy at mid-latitudes can be thought of as turbulent diffusion (Held, 1999), the anomalous energy flux is related to the changes in the meridional gradient and the eddy strength. Further calculations suggest that the meridional moist static energy gradient at mid-latitudes does not change significantly, thus the decrease in the energy flux is caused by weaker eddies. To understand the change in eddy activities, we examine the velocity scale ($V$) and the length scale ($L$) of the baroclinic eddies. Figures 3.7d-f show the change in EKE due to BC at different altitudes. Free tropospheric BC results in a reduction in EKE, which peaks at upper troposphere where the climatological EKE is the strongest. The average velocity of the eddies (the square root of mean EKE) decreases by about 13% (3%) due to upper (mid-) tropospheric BC. The change in EKE due to boundary layer BC is, again, not statistically significant. The decrease in eddy velocity is largely a result of the enhanced static stability, consistent with the scaling theories stating that $V$ is inversely proportional to the isentrope slope (Held and Larichev, 1996). Following previous literatures (e.g., Barry et al., 2002), we further diagnose the average meridional mixing length $L \propto F/VT_y$, where $F$ is the meridional eddy heat flux and $T_y$ is the meridional temperature gradient. Upper and mid- tropospheric BC results in a 6% and 4% decrease in the eddy length scale, respectively. The decrease in the mixing length is consistent with the Rhine's scale ($L_\beta = (V/\beta)^{1/2}$, where $\beta$ is the meridional gradient of the Coriolis parameter) at which the inverse energy cascade is halted by $\beta$-effect (Held and Larichev, 1996; Barry et al., 2002). A detailed discussion on the scaling arguments for baroclinic eddies is beyond the scope of this paper, but we hope that similar tropospheric heating experiments in GCMs can be used to test eddy closure theories in future studies.

In this study we focus on changes in the zonal mean flow. In reality the longitudinal variations in the Earth's surface and the inhomogeneous forcing can excite stationary waves and thus result in changes in the zonally asymmetric flow (e.g., Held et al., 2002; Ming et al., 2011). The effects of these two factors are always coupled with each other and may not be separated cleanly. Here we only include one source of zonal asymmetry by using an AGCM with realistic geography, but with idealized BC forcing, and the role of changes in stationary eddies may be underestimated. Future work may focus on the atmospheric response to idealized BC forcing in AGCMs with idealized boundary conditions (e.g., aqua-planet models) or to inhomogeneous BC forcing in realistic AGCMs.

### 3.3.3 Energy budget

The above analysis shows that the temperature response is key to understanding the extratropical circulation change. Free tropospheric BC affects the static stability and meridional temperature gradient at mid-latitudes, which weakens the baroclinic eddies and thus the meridional energy transport. It is clear that the temperature and circulation changes due to upper tropospheric BC are much more stronger than that due to mid-tropospheric BC. Boundary layer BC, in contrast, does not have a significant effect on temperature, zonal wind, or eddy activity.

The altitude-dependence of BC-induced response is not immediately intuitive. Since we use the same BC burden in the three experiments, the increase in atmospheric shortwave absorption is similar and cannot explain the different magnitudes of temperature change. An analysis of the change in heating rates provides some insights into the temperature response (Figure 3.8). Atmospheric temperature is affected by physical processes including radiative shortwave (SW) heating and longwave (LW) cooling, latent heat release by convective and large-scale cloud formation, vertical diffusion, and dynamical advection of sensible heat. BC at different altitudes

results in local SW heating anomalies. Note that the SW heating due to boundary layer BC is stronger than that due to free tropospheric BC because model layers in the boundary layer contain less mass. The vertical integrated SW heating actually increases slightly with altitude as a result of low and middle clouds. Since we focus on the equilibrium response to a perturbation, the changes in heating rates by different processes have to balance out one another. Therefore as diabatic heating terms (radiative and latent heating) and vertical diffusion are computed directly from the model output, one can evaluate dynamical advection as a residual.

When BC is added in the free troposphere, the most important sources of heating rate changes are SW radiation, latent heat release by large-scale precipitation, and dynamical advection. The forced increase in SW heating in the upper troposphere is mainly offset by a decrease in dynamical heating (Figure 3.8a), while the reduction in large-scale precipitation and dynamical heating are almost equally important in balancing out the stronger SW heating in the mid-troposphere (Figure 3.8b). Note that the change in LW radiation is small despite the strong local warming. Further analysis indicates that there is a decrease in the cloud amount at the heating layer. This leads to a decrease in LW emissivity which balances out the higher temperature, and as a result there is only a small change in LW radiation. Below the heating layer, the increase in dynamical heating contributes to a higher temperature, which is damped by decreased convective heating. The large response of dynamical advection compared to other heating sources indicates the change in the large-scale circulation is the main mechanism for reestablishing the atmospheric energy balance under a heating perturbation in the free troposphere.

The energy balance change due to boundary layer BC is very different. The warming at $\sim$900 hPa stabilizes the boundary layer, and thus suppresses turbulent diffusion of sensible heat and shallow convection. As a result, the increased SW absorption in the heating layer is mainly damped by subgrid vertical diffusion and a decrease

in convective heating. Below the heating layer, LW cooling becomes stronger and is balanced by the resulting increase in latent heat release by large-scale condensation. The change in dynamical advection is very small, indicating that boundary layer BC is less capable of altering atmospheric circulation than free tropospheric BC. This is consistent with the result that boundary layer BC does not cause significant changes in zonal wind or baroclinic eddies.

We conclude this section by noting that the heating rate changes caused by LW radiation and latent heat release are closely related to cloud changes. While it is expected that the model simulated extratropical responses are more robust than tropical responses which may be strongly affected by uncertainties in convective parameterizations, we emphasize that it remains to be seen whether other GCMs may yield similar results. In addition BC can also result in changes in clouds through the indirect effect and the cloud-absorption effect (Jacobson, 2012), which are not considered here. These effects are potentially large but uncertain, and inclusion of them would likely quantitatively alter our results.

## 3.4 Theory

In order to further understand why the temperature response to upper tropospheric BC is much stronger, we examine how the change in dynamical advection due to free tropospheric BC occurs. The advection of sensible heat ($DY$) can be divided into contributions from the mean meridional circulation and eddies (both stationary and transient):

$$DY = -\frac{\overline{v}}{a}\frac{\partial \overline{T}}{\partial \phi} - \overline{\omega}\left(\frac{\partial \overline{T}}{\partial p} - \frac{R\overline{T}}{C_p p}\right) - \frac{1}{a cos\phi}\frac{\partial \overline{v'T'} cos\phi}{\partial \phi} - \left(\frac{\partial \overline{\omega'T'}}{\partial p} - \frac{R\overline{\omega'T'}}{C_p p}\right). \quad (3.1)$$

Here $v$ is the meridional wind, $\omega$ the vertical pressure velocity, $T$ the temperature; $a$ is the radius of the Earth, $\phi$ the latitude, $p$ the pressure, $R$ the gas constant,

$C_p$ the specific heat capacity of air. Overbars denote monthly and zonal means, primes deviations thereof. The first and second right-hand-side terms of Eq. (3.1) are the meridional and vertical advection of heat by the mean meridional circulation, respectively. The third and fourth terms are meridional and vertical eddy heat flux convergence, respectively.

Figure 3.9 shows the vertical profiles of changes in different terms of Eq. (3.1) at mid-latitudes due to free tropospheric BC. Note that the explicitly computed $DY$ change agrees approximately with the inferred one in Figure 3.8. It is clear that the response of dynamical advection is dominated by the change in vertical eddy heat flux convergence, which cools the heating layer and warms the atmosphere below. There is also anomalous mean advective warming associated with the weaker Ferrel Cell (Fig. 3.5) in the upper tropospheric BC perturbation case, but the magnitude is much smaller. The change in meridional eddy heat flux convergence is also small. This is because the strongest weakening of the meridional eddy heat flux at the jet core (not shown) leads to an increase (decrease) in the heat flux convergence on the equatorward (poleward) flank of the jet, which cancel out when averaged over mid-latitudes.

In Section 3.3 we have shown the dominant balance between dynamical advection and SW heating. Neglecting the small terms in Eq. (3.1) and using potential temperature ($\theta$) instead of temperature to simplify the equation, we have:

$$\delta \left\langle \frac{\partial \overline{\omega'\theta'}}{\partial p} \right\rangle dp \approx \langle Q \rangle \,, \tag{3.2}$$

where $Q$ is the heating rate by BC-induced SW absorption and the angle brackets denote a horizontal average (mid-latitudes in this study). Integrating from the bottom of the heating layer to the tropopause at mid-latitudes and since the vertical heat

flux at the tropopause is approximately zero, Eq. (3.2) then becomes:

$$\delta \left\langle \overline{\omega'\theta'} \right\rangle_h \approx \{Q\}\,, \tag{3.3}$$

where $\{Q\} = \int_{p_t}^{p_h} \langle Q \rangle \, dp$ and subscripts h and t denote the bottom of the heating layer and the tropopause, respectively. Eq. (3.3) indicates that the weaker vertical eddy heat flux across the heating level acts to balance the anomalous SW heating above it. Note that $\{Q\}$ resulting from upper and mid- tropospheric BC are similar.

It is tempting to relate the change in vertical eddy heat flux to the change in static stability as our ultimate goal is to understand the temperature response. In the interior of the extratropical troposphere, the total eddy heat flux is roughly aligned along the mean isentropes (Held and Schneider, 1999). In the pressure coordinate this can be written as:

$$-\frac{\left\langle \overline{\omega'\theta'} \right\rangle_h}{\left\langle \overline{v'\theta'} \right\rangle_h} = \frac{\left\langle \partial_y \overline{\theta} \right\rangle_h}{\left\langle \partial_p \overline{\theta} \right\rangle_h}. \tag{3.4}$$

The horizontal eddy heat flux can be related to the mean meridional temperature gradient using the eddy diffusivity of heat (D); that is, $\left\langle \overline{v'\theta'} \right\rangle_h = -D \left\langle \partial_y \overline{\theta} \right\rangle_h$. Therefore Eq. (3.4) can be written as:

$$\left\langle \overline{\omega'\theta'} \right\rangle_h = \frac{D \left\langle \partial_y \overline{\theta} \right\rangle_h^2}{\left\langle \partial_p \overline{\theta} \right\rangle_h}. \tag{3.5}$$

Since the atmosphere is perturbed by globally uniform BC at a certain level in this study, one would expect the change in meridional temperature gradient ($\left\langle \partial_y \overline{\theta} \right\rangle_h$) is small. It can be seen in Figure 3.1 that the temperature response at mid-latitudes does not has much meridional difference at mid-latitudes. More detailed calculations show that the change in $\left\langle \partial_y \overline{\theta} \right\rangle_h$ due to upper (mid-) tropospheric BC is less than 5% (1%) when averaged over mid-latitudes, despite some spatial variations within the mid-latitudes. If the changes in $D$ is also small, the perturbation of the vertical eddy

heat flux can be approximated as:

$$\delta \left\langle \overline{\omega' \theta'} \right\rangle_h \approx -D \frac{\left\langle \partial_y \overline{\theta} \right\rangle_h^2}{\left\langle \partial_p \overline{\theta} \right\rangle_h^2} \delta \left\langle \partial_p \overline{\theta} \right\rangle_h = -DI^2 \delta \left\langle \partial_p \overline{\theta} \right\rangle_h , \tag{3.6}$$

where $I = \frac{\left\langle \partial_y \overline{\theta} \right\rangle_h}{\left\langle \partial_p \overline{\theta} \right\rangle_h}$ is the isentropic slope. We use the change in bulk static stability below the heating level to approximate the stratification change at the heating level; that is, $\delta \left\langle \partial_p \overline{\theta} \right\rangle_h \approx \frac{\delta \left\langle \overline{\theta} \right\rangle_h - \delta \left\langle \overline{\theta} \right\rangle_s}{p_h - p_s}$, with the subscript s denoting the surface. We further neglect the change in surface temperature since SST is fixed; that is, $\delta \left\langle \overline{\theta} \right\rangle_s = 0$. Eq. (3.6) then becomes:

$$\delta \left\langle \overline{\omega' \theta'} \right\rangle_h \approx -DI^2 \frac{\delta \left\langle \overline{\theta} \right\rangle_h}{p_h - p_s}. \tag{3.7}$$

Combining Eq. (3.3) and Eq. (3.7) yields:

$$\delta \left\langle \overline{\theta} \right\rangle_h \approx \{Q\} D^{-1} I^{-2} \left( p_s - p_h \right). \tag{3.8}$$

Eq. (3.8) shows that temperature change due to a certain amount of heating is determined by the diffusivity, the isentropic slope, and the pressure difference between the surface and the heating level. Both the diffusivity and the isentropic slope have a vertical structure with lower values at higher altitudes (Chen and Plumb, 2014), while the pressure difference is larger for a forcing at higher altitude. As a result, all three factors contribute to a stronger temperature change due to heating in the upper troposphere.

The above analysis highlights the role of baroclinic eddies in re-establishing atmospheric energy balance at mid-latitudes in the presence of BC-induced SW heating. Since the change in the vertical eddy heat flux tends to diffuse the anomalous heating away from the heating layer, one would expect the warming signal penetrates more to lower troposphere at mid-latitudes in the Northern Hemisphere where eddies are more energetic. This is clearly shown in our AGCM simulated temperature response

(Figure 3.1). To confirm the importance of baroclinic eddies in driving atmospheric response at mid-latitudes, we conduct similar heating experiments with the dry idealized model (Section 2.2). Figure 3.10 compares the temperature changes in the AGCM and in the idealized model, which have qualitatively similar vertical profiles. The magnitude of temperature change increases with height before reaching its maximum at the heating level. The temperature change due to upper tropospheric heating is 2.4 (1.9) times of that due to mid-tropospheric heating in the AGCM (idealized model). In the AGCM the shortwave absorption of BC becomes more effective as BC rises above the reflective cloud layer, and model simulated SW heating due to upper tropospheric BC is larger than that due to mid-tropospheric BC by $\sim$20% (not shown). If taking into account the vertical variation in heating, the ratio in the idealized model would be about $1.9\times1.2=2.28$, even closer to the AGCM result. The similarities between the AGCM and the idealized model demonstrate the dominant role of dry dynamics in determining temperature response at mid-latitudes to anomalous heating in the free troposphere. We also notice some differences between the two models. The maximum warming in the idealized model is larger than that in the AGCM by about a factor of 2, and the warming below the heating level is weaker in the idealized model. The discrepancies indicate the influence of other factors in the AGCM (e.g., convection, radiation, boundary layer processes) on the thermal structure of mid-latitudes and thus the atmospheric response to BC-induced heating.

In deriving Eq. (3.8) we make an important assumption that the change in eddy diffusivity ($D$) is small. A constant $D$ would allow us to avoid much discussion on the specific scaling of diffusivity and temperature gradient and simplify the equations. This may not be a strictly valid assumption since free tropospheric BC has a significant influence on baroclinic eddies (Section 3.2). The above derivation, however, can be generalized to a case in which $D$ is not a constant. Despite different forms, almost all the scaling relations for $D$ used in the literature are inversely proportional

to the $n$th power of the stratification (e.g., Green, 1971; Held and Larichev, 1996; Zurita-Gotor and Vallis, 2010; Jansen and Ferrari, 2013). Thus from Eq. (3.5) we have $\left\langle \overline{\omega'\theta'} \right\rangle_h \propto \left\langle \partial_p \overline{\theta} \right\rangle_h^{-n-1}$, and Eq. (3.8) still holds except that there is an extra term that is proportional to $\left\langle \partial_p \overline{\theta} \right\rangle_h^{-n-1}$ on the right hand side. This will not affect the qualitative conclusion that heating at higher altitudes yields a stronger temperature response.

## 3.5 Discussion and conclusions

The GFDL AM2 is used to examine the extratropical atmospheric-only response to global uniform BC forcings at different altitudes. BC direct and semi-direct effects are considered in our analysis. Free tropospheric BC-induced SW heating warms the troposphere with maximum temperature increase at the heated altitudes. For the same column burden, the temperature change due to upper tropospheric BC is much stronger. The warming signal penetrates to a greater depth at mid-latitudes than in the tropics. As a result, free tropospheric BC stabilizes the mid-latitude atmospheric column and weakens meridional temperature gradient on the equatorward flank of the tropospheric jet. Consistent with the thermal wind relation and the change in the eddy momentum flux, the response of the zonal-mean circulation to upper tropospheric BC features a strong weakening and poleward shift of the jet. Mid-tropospheric BC weakens the jet without significantly shifting its location. Boundary layer BC yields slight warming of the troposphere and has a weak impact on the jet.

Free tropospheric BC results in weaker mean meridional circulation and less energetic baroclinic eddies at mid-latitudes. The weakening of the eddies is characterized by a smaller eddy velocity related to the stronger stratification and a shorter mixing length consistent with the Rhine's scale. The less energetic eddies result in a reduction in the meridional energy transport by transient eddies, which dominates

the change in total meridional energy transport at mid-latitudes. Similar to the temperature response, the weakening of eddy activities and associated energy transport due to upper tropospheric BC is much stronger than that due to mid-tropospheric BC. Boundary layer BC does not has a strong influence on the mean circulation and baroclinic eddies.

An investigation of changes in heating rates at mid-latitudes helps explain the altitude dependence of the temperature response to BC-induced heating, which is key to understand the response of extratropical circulation. A large fraction of the BC-induced boundary layer SW heating is damped by vertical diffusion of sensible heat. As a result, boundary layer BC only causes a small temperature change and does not effectively alter the large-scale circulation. BC-induced free tropospheric SW heating causes a strong change in the vertical profile of dynamical heating, which is dominated by the change in vertical eddy heat flux convergence. There is a reduction in vertical eddy heat transport to the heating level, which balances the BC-induced local SW heating and warms the atmosphere below the heating layer. Upper tropospheric BC results in a stronger temperature response since the eddy diffusivity and the isentrope slope decrease with height and the increase in stratification extends to higher altitudes. Similar results are found when using a dry idealized model, which further highlights the importance of dry dynamics in driving the temperature change at mid-latitudes. Other factors, such as moisture and radiation, also affect the extratropical response, but their impacts are secondary.

The strong atmospheric-only response at mid-latitudes suggests that BC is capable of altering weather pattern, as the underlying dynamics involved operate on synoptic time-scales. Our results suggest that BC may also modulate extratropical cyclones and affect mid-latitude extreme weather. Preliminary results (not shown) indicate that upper tropospheric BC leads to increases in light precipitation frequency and decreases in moderate to heavy precipitation frequency over the storm track re-

gions, and reduces total precipitation by ∼20%. Mid-tropospheric BC yields similar but weaker changes in precipitation extremes. The decreases in mid-latitude extreme precipitation due to free tropospheric BC is consistent with weaker baroclinic eddies. Since BC is mainly removed from the atmosphere through wet scavenging, the decrease in precipitation may further amplify the circulation response when BC concentration is interactive with atmospheric circulation rather than prescribed, as in this study.

The regional perturbation experiments suggest that the atmospheric response to BC is mostly local and linearly additive, and the extratropical response examined in this study is ascribed mainly to mid-latitude BC. Thus, the results presented here have important implications for understanding the climate impacts of realistic BC, which concentrates at mid-latitude industrial regions in the Northern Hemisphere. The strong altitude-dependence of BC-induced response indicates that BC at higher altitudes, albeit less abundant, may still have large impacts on climate. This highlights the importance of better constraining the spatial distribution of BC concentration, which is currently uncertain across global models and observations (Koch et al., 2009; Bond et al., 2013). In general model simulated BC has a high bias in the upper troposphere (Allen and Landuyt, 2014), therefore it is likely that the BC-induced atmospheric responses presented here are overestimated in current models.

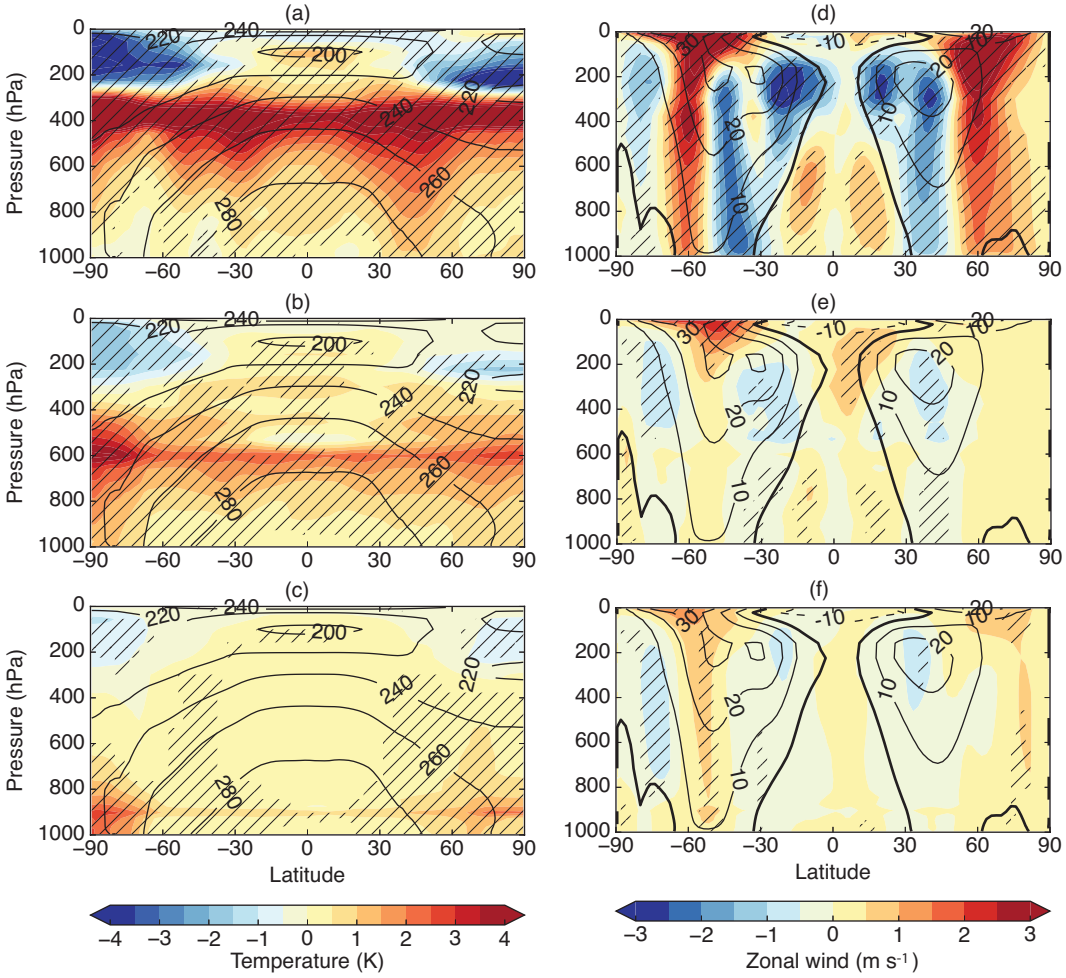



Figure 3.1: Changes in (left) zonal mean temperature and (right) zonal wind resulting from BC at $\sigma =$ (a),(d) 0.38, (b),(e) 0.60, and (c),(f) 0.90 (bottom). The black contour lines denote the climatological mean in the control run. The hatching represents significance at the 0.05 level.

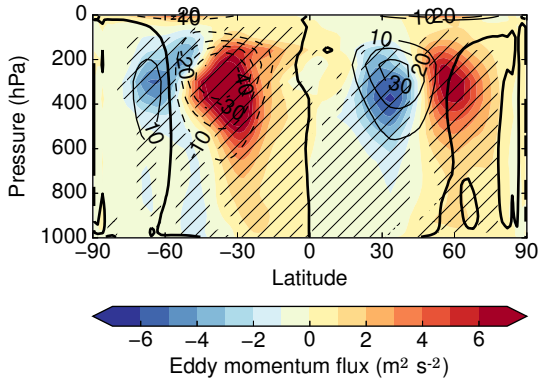



Figure 3.2: Changes in zonal mean eddy momentum flux resulting from BC at $\sigma = 0.38$. The black contour lines denote the climatological mean in the control run. The hatching represents significance at the 0.05 level.

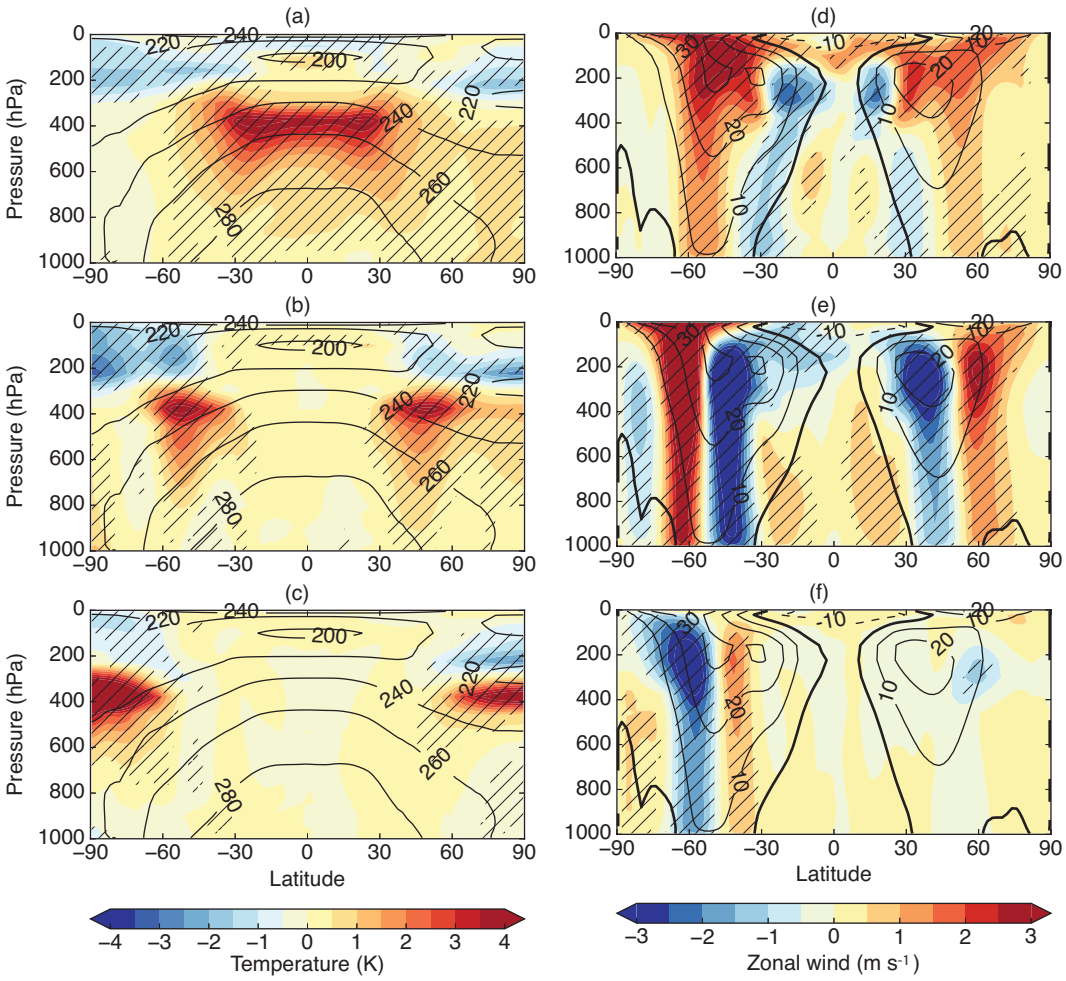



Figure 3.3: Changes in (left) zonal mean temperature and (right) zonal wind resulting from BC in the (a),(d) tropics (30°S-30°N), (b),(e) mid-latitudes (30°-60°N and 30°-60°S), and (c),(f) high latitudes (60°-90°N and 60°-90°N) at $\sigma = 0.38$. The black contour lines denote the climatological mean in the control run. The hatching represents significance at the 0.05 level.

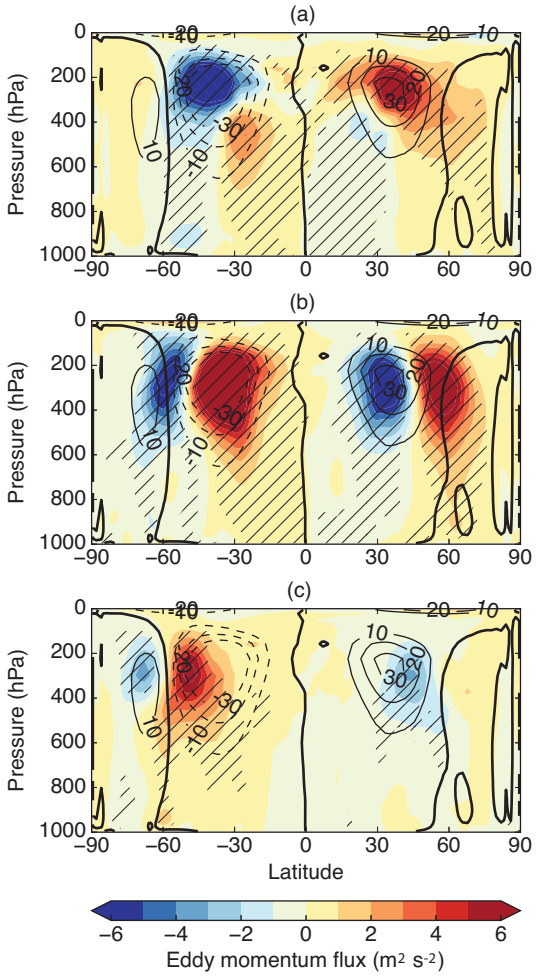



Figure 3.4: Changes in zonal mean eddy momentum flux resulting from BC in the (a) tropics, (b) mid-latitudes, and (c) high latitudes (bottom) at $\sigma = 0.38$. The black contour lines denote the climatological mean in the control run. The hatching represents significance at the 0.05 level.

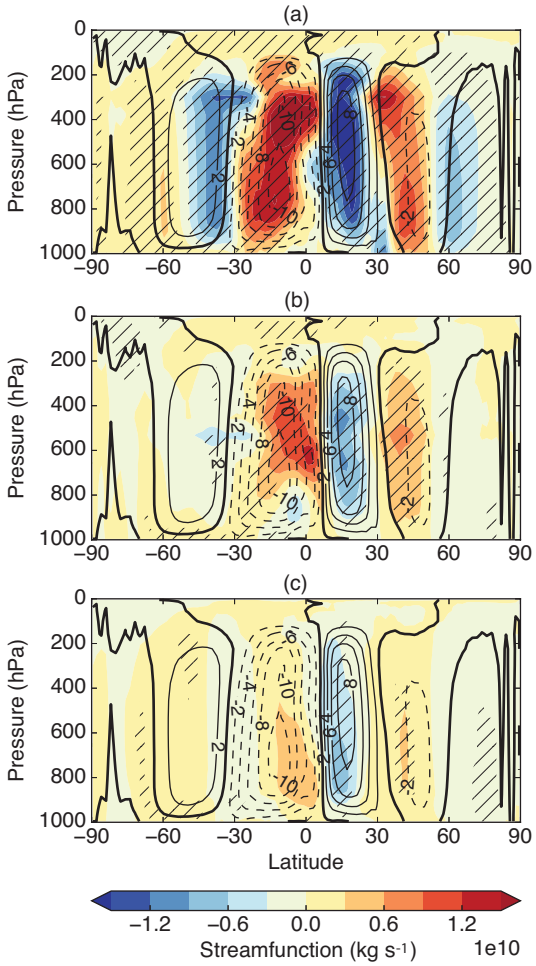



Figure 3.5: Changes in meridional streamfunction resulting from BC at $\sigma =$ (a) 0.38, (b) 0.60, and (c) 0.90. The black contour lines denote the climatological mean in the control run. Positive values indicate clockwise motion and negative values indicate counterclockwise motion. The hatching represents significance at the 0.05 level.

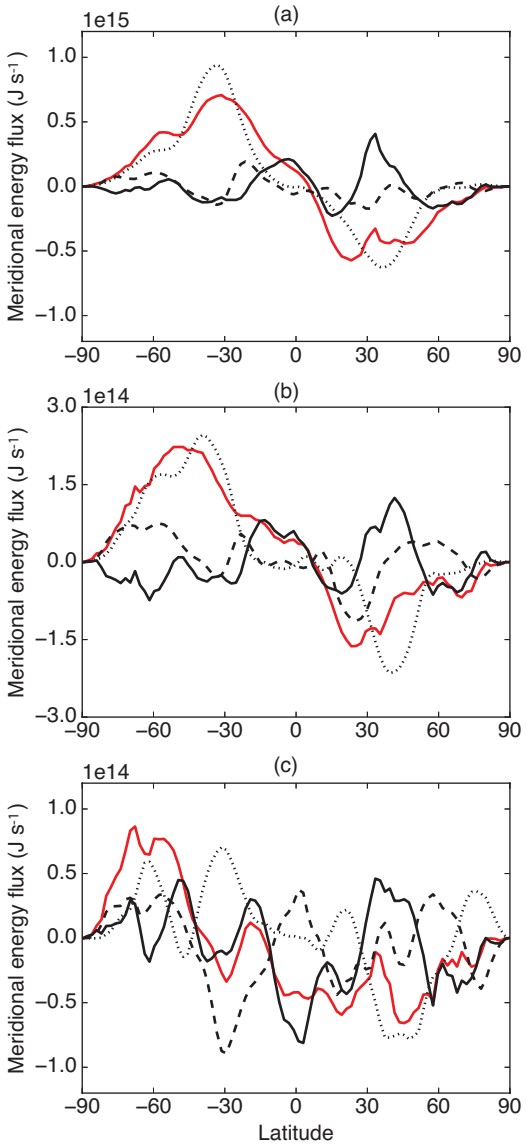



Figure 3.6: Changes in northward energy flux (red solid) and contributions from the mean meridional circulation (black solid), stationary eddies (black dashed), and transient eddies (black dotted) resulting from BC at $\sigma$ = (a) 0.38, (b) 0.60, and (c) 0.90. Note that the y-axis scale is different in (a), (b) and (c).

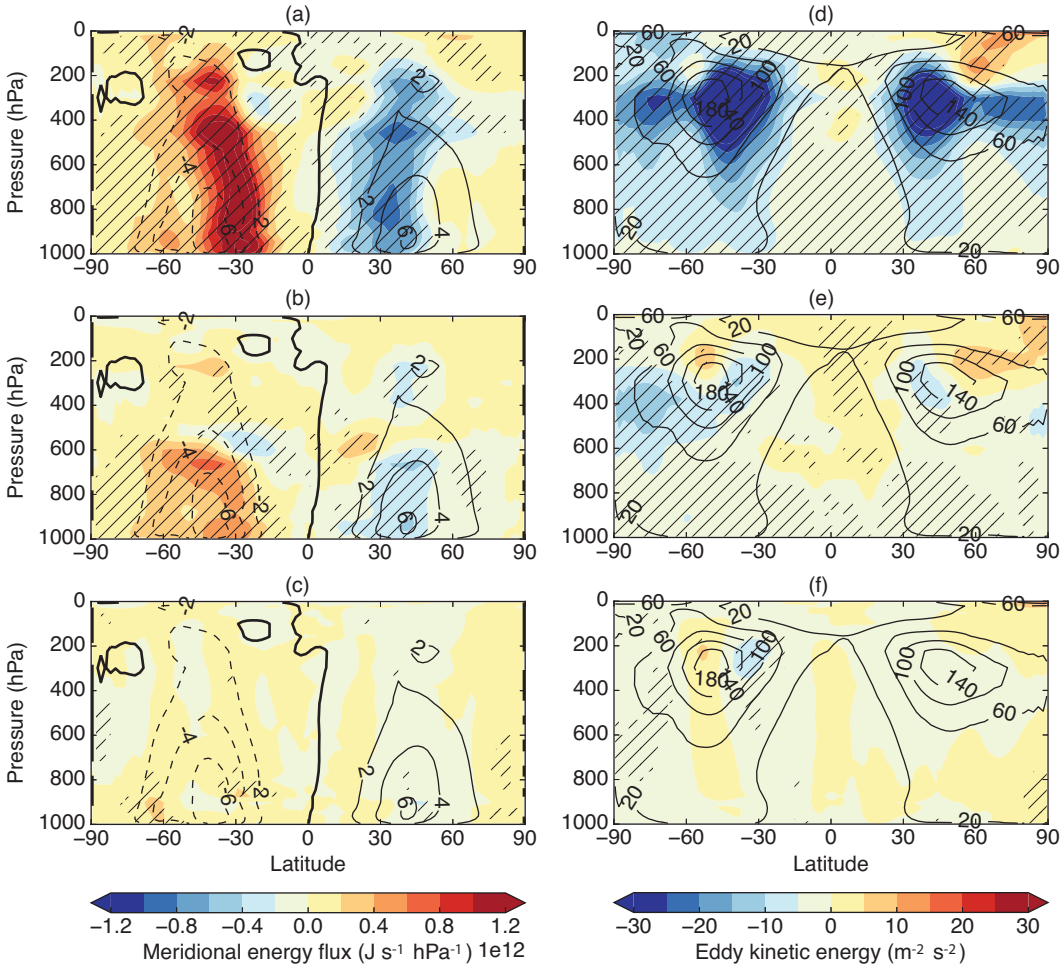



Figure 3.7: Changes in (left) northward energy flux by transient eddy and (right) eddy kinetic energy resulting from BC at $\sigma$ = (a),(d) 0.38, (b),(e) 0.60, and (c),(f) 0.90. The black contour lines denote the climatological mean in the control run. The hatching represents significance at the 0.05 level.

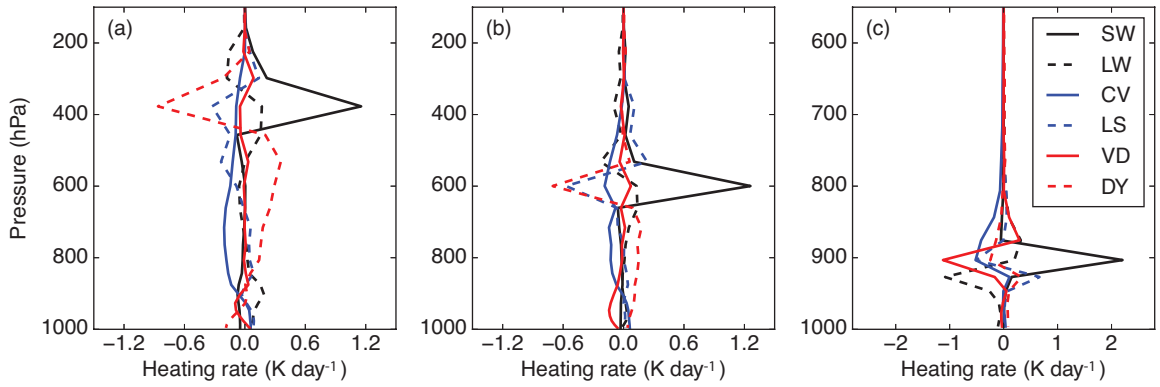



Figure 3.8: Changes in mid-latitude heating rates caused by shortwave (SW) and longwave (LW) radiation, latent heat release by convective (CV) and large-scale (LS) cloud formation, subgrid vertical diffusion (VD), and dynamical advection (DY) resulting from BC at $\sigma$ = (a) 0.38, (b) 0.60, and (c) 0.90.

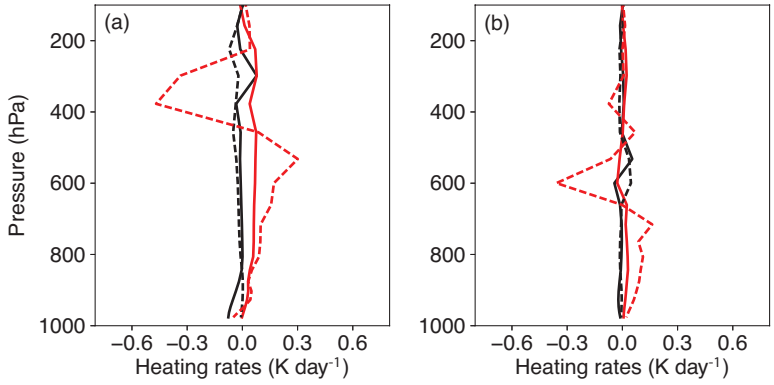



Figure 3.9: Changes in mid-latitude adiabatic heating rates averaged at mid-latitudes resulting from BC at $\sigma$ = (a) 0.38 and (b) 0.60. Solid lines represent changes in the meridional (black) and vertical (red) advection of heat by the mean meridional circulation. Dashed lines represent changes in meridional (black) and vertical (red) eddy heat flux convergence.

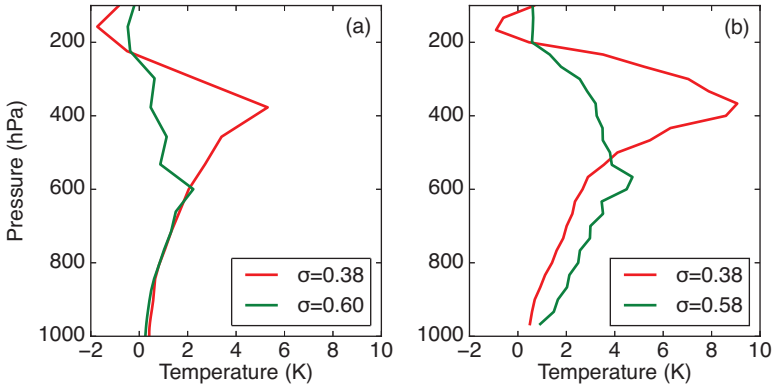



Figure 3.10: Vertical profiles of temperature changes at mid-latitudes resulting from (a) BC at $\sigma = 0.38$ (red) and $\sigma = 0.60$ (green) in AM2 and (b) heating at $\sigma = 0.38$ (red) and $\sigma = 0.58$ (green) in the idealized model.

# Chapter 4

# Nonlinear boreal winter tropical circulation response to greenhouse gas and aerosol forcing

## 4.1 Introduction

Greenhouse gases (GHGs) and aerosols are the two most important anthropogenic forcing agents of the Earth's climate system. Globally, anthropogenic aerosols partly offset the warming due to GHGs by scattering solar radiation and interacting with clouds. The effects of anthropogenic aerosols on the atmospheric circulation are nearly opposite to the GHG-induced changes. More specifically, the atmospheric response to GHGs is characterized by a weakening of the tropical circulation (Vecchi and Soden, 2007), an expansion of the Hadley cell (Lu et al., 2007), and a poleward shift of the subtropical jets and midlatitude storm tracks (Yin, 2005; Lorenz and DeWeaver, 2007). On the other hand, scattering aerosols result in a strengthening (weakening) of the Hadley circulation during boreal winter (summer) (Allen and Sherwood, 2011;

Ming and Ramaswamy, 2011; Ming et al., 2011), a southward shift of the Intertropical Convergence Zone (ITCZ), and an equatorward shift of the jets.

Since the climate impacts of GHGs and aerosols generally differ in sign, an important issue is whether the combined effect is simply the linear sum of individual effects. Several previous studies have suggested that this may not be the case at either global or regional scales. For instance, the increase in global mean temperature resulting from combined GHG and aerosol forcing appears to be smaller than that obtained by adding the individual responses (Feichter et al., 2004; Ming and Ramaswamy, 2009). The nonlinear thermal response is stronger in the Northern Hemisphere (NH) than in the Southern Hemisphere (SH), consistent with the hemispherically asymmetric distribution of aerosols (Ming and Ramaswamy, 2009). Ming et al. (2011) showed that changes in the wintertime subtropical jet and extratropical tropopause height in the NH in response to GHGs and aerosols deviate significantly from the linear sum, indicating that there is substantial nonlinearity in the atmospheric circulation response. Despite these early attempts, the nonlinearity in the climate response to GHGs and aerosols has not been studied systematically and is often neglected in climate change attribution studies. It is not clear whether the nonlinear effect is robust across different models. Additionally, the climate effects of aerosols is further complicated by the uncertain spatial distribution and aerosol-cloud interactions.

In this study we seek to add clarity to this issue by investigating the nonlinearity in climate impacts of idealized forcings. We analyze the atmospheric responses to a doubling of $CO_2$ and a zonally symmetric perturbation to incoming solar radiation that mimics the idealized radiative effect of scattering aerosols. We focus on the boreal winter season when the atmospheric circulation trend is greatest in model simulations and observations (Deser and Phillips, 2009).

## 4.2 Method

### 4.2.1 Solar forcing perturbation

The approach we use to perturb solar forcing follows Clark et al. (2018), with modifications to take into account the seasonal cycle as described below. The climatological annual-mean insolation ($S$) as a function of latitude ($\theta$) is given by

$$S(\theta) = \alpha(\theta) S_0, \tag{4.1}$$

where $\alpha$ is a normalization function and $S_0$ is the solar constant. We modify the solar radiation in such a way that the perturbed annual and zonal-mean insolation is given by

$$S'(\theta) = \alpha(\theta)(S_0 + \frac{\delta S(\theta)}{\alpha(\theta)}) = S(\theta) + \delta S(\theta), \tag{4.2}$$

where $\delta S(\theta)$ is a zonally symmetric and time-independent insolation perturbation that has a Gaussian shape:

$$\delta S(\theta) = -\frac{M}{M_0} exp\left[-\frac{(\theta - \theta_c)^2}{2\sigma}\right]. \tag{4.3}$$

Here $M$ is the magnitude of the global mean downward top-of-atmosphere solar forcing, $\theta_c$ is the latitude of the center of the forcing and $\sigma$ controls the width of the forcing. $M_0$ is a normalization parameter:

$$M_0 = \frac{1}{2}\int_{-\frac{\pi}{2}}^{\frac{\pi}{2}} exp\left[-\frac{(\theta - \theta_c)^2}{2\sigma}\right] cos\theta d\theta. \tag{4.4}$$

In this study $\theta_c$ and $\sigma$ are chosen such that the latitudinal structure of solar forcing is similar to that of realistic aerosol forcing, as discussed in Section 4.2.2.

### 4.2.2 Model description and experimental design

In this study we use the Geophysical Fluid Dynamics Laboratory (GFDL) Atmospheric Model version 2 (AM2) coupled to a slab ocean. The configuration and performance of the atmospheric model and the slab ocean model are described by GFDL GAMDT (2004) and Stouffer et al. (2006), respectively; here we describe briefly the features most relevant to this study. AM2 uses a finite volume dynamical core with a horizontal resolution of about $2^\circ \times 2.5^\circ$ and has 24 hybrid vertical levels from the surface to 3 hPa. The shortwave and longwave radiation algorithms follow Freidenreich and Ramaswamy (1999) and Schwarzkopf and Ramaswamy (1999), respectively, with modifications as described in GFDL GAMDT (2004). The model uses the relaxed Arakawa–Schubert (RAS) convective parameterization, which represents moist convection as multiple entraining plumes that produce precipitation (Moorthi and Suarez, 1992). Stratiform clouds are represented following Tiedtke (1993), with modifications as described in Anderson et al. (2004). Cloud microphysics is parameterized based on Rotstayn (1997) and Rotstayn et al. (2000). Convective planetary boundary layers are parameterized using a K-profile scheme based on Lock et al. (2000). For stable layers, conventional stability functions dependent on the Richardson number are used. Monthly mean abundances of tropospheric aerosols and ozone are prescribed from offline simulations using a chemical transport model driven by general circulation model simulated meteorological fields (Horowitz, 2006). The atmospheric model is coupled to a mixed-layer ocean with a uniform depth of 50 m. Oceanic heat transport is accomplished using heat flux adjustment and is assumed to be constant under climate change. The model has been used to study the climate response to GHGs and aerosols (e.g., Ming and Ramaswamy, 2009; Ming et al., 2011).

The control simulation (CONT) is forced by present-day (1990) GHG and aerosol concentrations. We perturb the control run by a doubling of $CO_2$ ($CO_2$). For the solar forcing experiments (SOLAR) we follow the approach described in Section 4.2.1

to impose a solar forcing with $\theta_c$ set to 20°N and $\sigma$ set to 17.47° (Fig. 4.1a). We systematically vary the strength of the downward top-of-atmosphere solar forcing in a series of 7 experiments ($M$ = 2.5, 3.0, 3.5, 4.0, 4.5, 5.0, 5.5). Figure 4.1b shows the latitudinal structure of wintertime (December-February, DJF) zonal-mean radiative forcing from a sample solar forcing experiment ($M = 4$), which is generally similar to that of realistic aerosol forcing. To investigate the nonlinearity in the climate response we run another series of 7 experiments with the same solar forcing perturbation as well as a doubling of $CO_2$ ($CO_2$+SOLAR). The nonlinearity in the response of a given climate variable ($X$) is defined as:

$$\delta X_{nonlinear} = \delta X_{CO_2+SOLAR} - \delta X_{CO_2} - \delta X_{SOLAR}, \tag{4.5}$$

where the subscript at the right hand side of Eq. (4.5) denotes the experiment that $\delta X$ is derived from (as the difference between that experiment and CONT).

## 4.3 Results

Figure 4.2 shows the responses of zonal-mean temperature and zonal wind to a doubling of $CO_2$, a reduction in solar forcing ($M = 4.0$), and the combined forcings. The temperature response to $CO_2$ shows amplified warming in the tropical upper troposphere and near the surface at NH high latitudes, as well as cooling in the stratosphere. Similar to previous studies, $CO_2$ weakens (strengthens) the zonal wind at the equatorward (poleward) flank of the jet, resulting in a poleward shift of the jet in both hemispheres. The zonal-mean changes in temperature and zonal wind due to the reduction in solar forcing resemble the aerosol-induced changes (e.g., Ming et al., 2011). The cooling at NH midlatitudes strengthens (weakens) the meridional temperature gradient at the equatorward (poleward) flank of the jet, and as a result the jet shifts equatorward via the thermal-wind relationship. The key features of

the temperature response to combined $CO_2$ and solar forcing (Fig. 4.2c) in the low and high latitudes are similar to the $CO_2$-induced change, while the $CO_2$-induced warming in the NH midlatitudes is largely offset by cooling due to the reduction in solar forcing. The zonal wind response (Fig. 4.2g) to the combined forcing is dominated in the troposphere by solar forcing and is characterized by a strengthening and equatorward shift of the jet.

The spatial structure of the simulated responses of temperature and zonal wind to combined $CO_2$ and solar forcing is similar to the linear sum of the individual responses, but the magnitude of the responses is different in the NH (Figs. 4.2d and 4.2h). The warming at NH midlatitudes resulting from the combined forcing is weaker than the summed responses throughout the troposphere. The linear assumption overestimates the temperature response by about 0.3 K at NH midlatitude surface. Consistent with the temperature change, the strengthening of the jet resulting from the combined forcing is much stronger than the linear sum of individual responses. The nonlinearity in zonal wind anomalies at the jet core is about 2 m $s^{-1}$, one third of the zonal wind change in the combined forcing experiment. The nonlinearity in zonal-mean temperature and zonal wind responses is similar to that found by Ming et al. (2011), who used realistic greenhouse gas and aerosol concentrations. This indicates that the nonlinearity in the climate response to greenhouse gases and aerosols does not dramatically depend on the zonal asymmetry in the aerosol forcing.

Figure 4.3 shows the responses of the meridional streamfunction to a doubling of $CO_2$, a reduction in solar forcing ($M = 4.0$), and the combined forcing. During the wintertime the tropical mean meridional circulation is dominated by a cross-equatorial Hadley cell with northward upper-level flow, transporting energy from the warmer SH to the NH. As shown in previous studies, $CO_2$ results in a weakening and expansion of the Hadley cell. The tropical precipitation response to $CO_2$ is characterized by an overall increase between the equator and 10° and a slight decrease

in the subtropics (Fig. 4.4), while the effect of $CO_2$ on the location of the ITCZ is small. Solar forcing strengthens the cross-equatorial Hadley cell by cooling the NH and thus resulting in a substantial hemispheric asymmetry. There is an increase (decrease) in precipitation to the south (north) of the equator, indicating a southward shift of the ITCZ (Fig. 4.4). The overall structure of Hadley cell and precipitation responses to the combined forcing is dominated by solar forcing. The strengthening of the Hadley cell resulting from the combined forcing has a larger amplitude than the linear sum of individual responses, especially at the rising branch of the Hadley cell. Compared with the linear sum of precipitation changes, the response to the combined forcing show enhanced (reduced) precipitation to the south (north) of the equator, consistent with the stronger upward motion at and to the south of the equator (Fig. 4.3d). The nonlinearity in precipitation response is substantial near 10°, where $CO_2$ tends to amplify the response to solar forcing rather than mitigating it, as suggested by the linear sum of the individual responses.

The nonlinearity in the response of the Hadley cell can be explained by the nonlinearity in temperature response, since the cooler NH in the combined forcing experiment requires larger energy transport from the SH to the NH. In our experiments the change in the efficiency of meridional energy transport by Hadley cell (referred to as the gross moist stability) is roughly linear (not shown), therefore the larger interhemispheric energy transport can only be accomplished by stronger mass flux. Figure 4.5 compares the nonlinearity in mass flux changes at the equator with the hemispheric asymmetry in lower troposphere (850 hPa) temperature. The mass flux is defined as $\psi_{eq} = 2\pi a \int_0^{p_m} v dp/g$, where $v$ is the time- and zonal-mean meridional wind and $a$ the Earth's radius. For simplicity $p_m$ is fixed as the pressure at a midtropospheric level ($\sigma = 0.38$). The results are nearly identical if we use the level where the vertically integrated mass flux attains its maximum magnitude as $p_m$. It is clear from Figure 4.5 that the change in the mass flux resulting from the combined forcing is stronger

than the linear sum of individual changes in almost all experiments, and the mass flux response is closely associated with the response of hemispheric asymmetry in temperature.

The nonlinearity in temperature response is a robust feature throughout the year and increases with the magnitude of the solar forcing perturbation, as shown in Figure 4.6a-4.6c. In all experiments, the nonlinear component of the temperature response is negative in NH but positive in SH, while the nonlinearity in the global mean temperature response is less than 5% in general. This indicates that when $CO_2$ concentration is doubled, the climatologically cooler NH (resulting from a reduction in solar forcing) warms less than the SH. Similar results are also found in aquaplanet simulations (Seo et al., 2017), indicating that the difference in lower boundary condition (e.g., land-sea distribution and sea ice) between the two hemispheres does not play an important role. Previous studies have shown that the radiative forcing of $CO_2$ is dependent on the atmospheric state (Huang et al., 2016; Merlis, 2015). However, one would expect the $CO_2$ forcing in the warmer and wetter SH to be smaller than in the NH due to the masking effect of deep convective clouds and water vapor (Huang et al., 2016), and as a result the nonlinear temperature response cannot be attributed to the inhomogeneity in $CO_2$ forcing. Figure 4.6d-4.6f shows that the nonlinearity may arise from the hemispheric asymmetry in cloud feedbacks. The nonlinearity in changes in the cloud radiative effect is generally positive in the SH and deep tropics but negative in the NH subtropics and midlatitudes, resulting in hemispherically asymmetric thermal responses. Further calculations suggest that the nonlinear cloud radiative effect can be ascribed mostly to shortwave effects everywhere except in the deep tropics. The nonlinear cloud response is strongest during the summer (June-August, JJA), which can affect the wintertime temperature response due to the memory provided by the slab ocean.

An inspection of the low cloud and liquid water path responses sheds light on the cause of the nonlinearity. Fig. 4.7 shows the nonlinearity in the response of low cloud amount. The nonlinear component of annual mean low cloud amount shows a clear hemispheric asymmetry with negative peaks in the SH tropics and midlatitudes but near zero or positive values in the NH midlatitudes, leading to more warming in the SH than in the NH. The nonlinearity in low cloud changes has some seasonality and is stronger in summer than in winter, but in general the latitudinal structure in both seasons follows that in the annual mean response. The nonlinearity in the response of liquid water path is generally positive at NH midlatitudes, especially in JJA (not shown). The stronger liquid water path results in larger cloud optical depth and thus stronger shortwave reflection, which is consistent with the nonlinear temperature response in the NH.

## 4.4 Discussion and conclusions

The climate response to a doubling of $CO_2$ and a hemispheric asymmetric solar forcing perturbation, which coarsely represents the effect of scattering aerosols, shows substantial nonlinearity. The linear sum of individual responses generally overestimates (underestimates) warming over the NH (SH) resulting from the combined $CO_2$ and solar forcing. Consistent with the nonlinear temperature response, the linear sum underestimates the acceleration of zonal wind at the equatorward flank of the NH jet as well as the strengthening of the cross-equatorial Hadley cell during the boreal winter. The solar forcing perturbation in this study is zonally symmetric, indicating that the nonlinearity in the climate response to GHGs and aerosols found in previous studies is a robust feature and does not depend on the spatial structure of aerosol forcing, which is uncertain and different across models.

The nonlinear temperature response mainly arises from cloud feedbacks. Preliminary results indicate that both low cloud amount feedback and cloud optical depth feedback play a role in causing the nonlinearity. Since large uncertainty remains in convection schemes and cloud parameterizations in current models, the robustness of the cloud response warrants further investigation. Nevertheless, this study highlights the importance of accounting for the nonlinearity when attributing climate change to specific forcings, especially at regional scales.

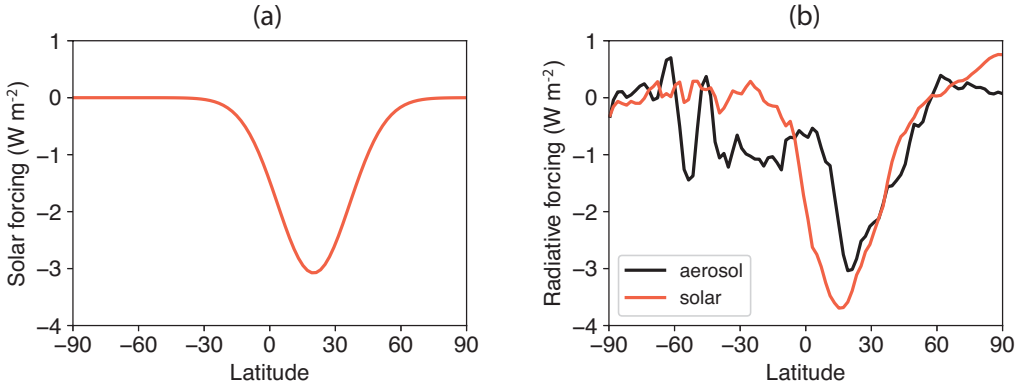



Figure 4.1: (a) Normalized annual mean perturbation to incoming solar radiation ($M = 1.0$). (b) DJF mean radiative forcing of solar radiation perturbation (red, $M = 4.0$) and anthropogenic aerosols (black, derived from the experiments in Ming and Ramaswamy (2009)). The radiative forcing is normalized to a global mean of 1 W $m^{-2}$.

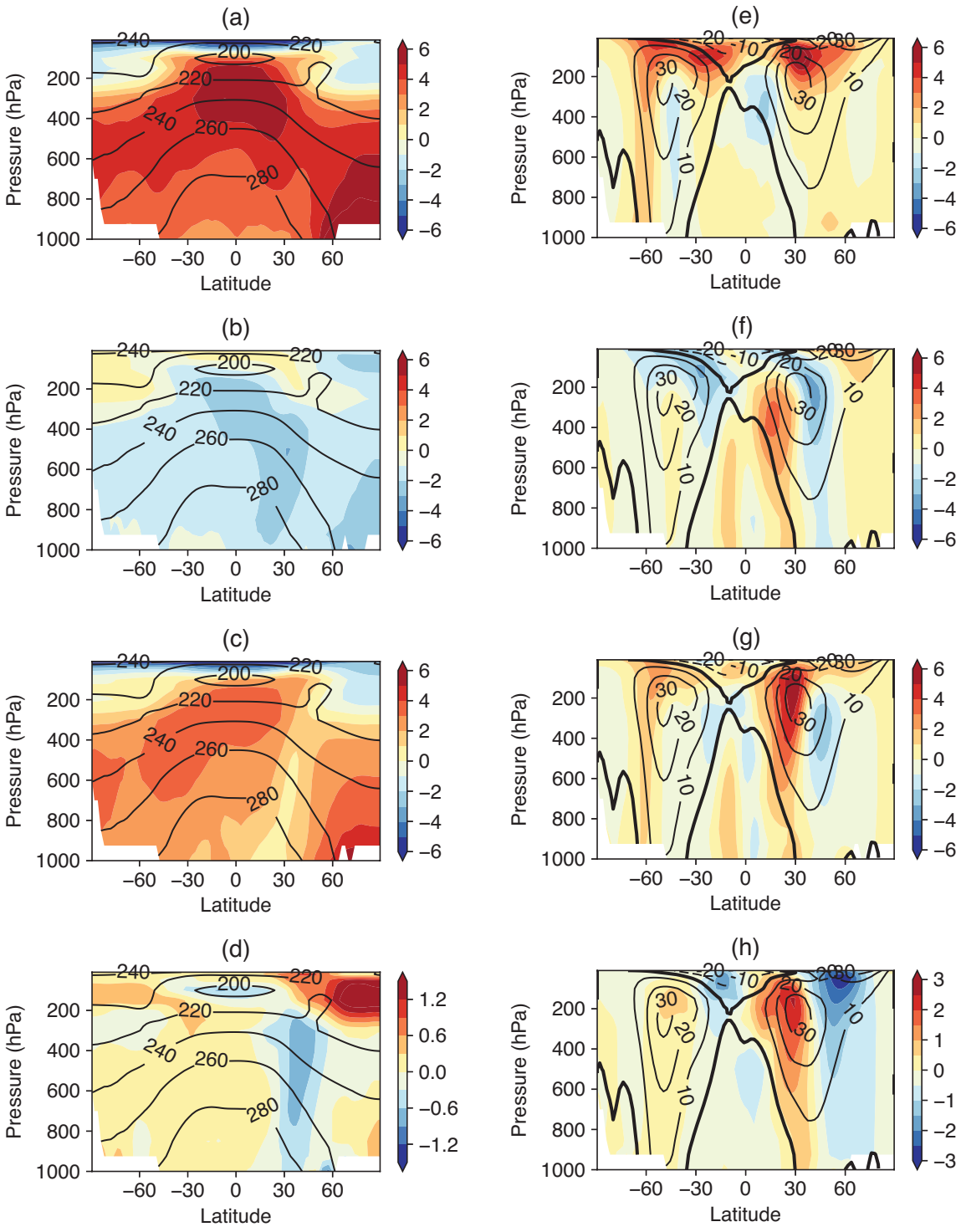



Figure 4.2: Changes in DJF zonal-mean (left) temperature (K) and (right) zonal wind (m $s^{-1}$) resulting from (a,e) a doubling of $CO_2$, (b,f) a reduction in solar forcing ($M = 4.0$), and (c,g) the combined forcing. Nonlinearity in the responses of zonal mean (d) temperature and (h) zonal wind is also shown. The black contours denote the climatological mean from the control run.

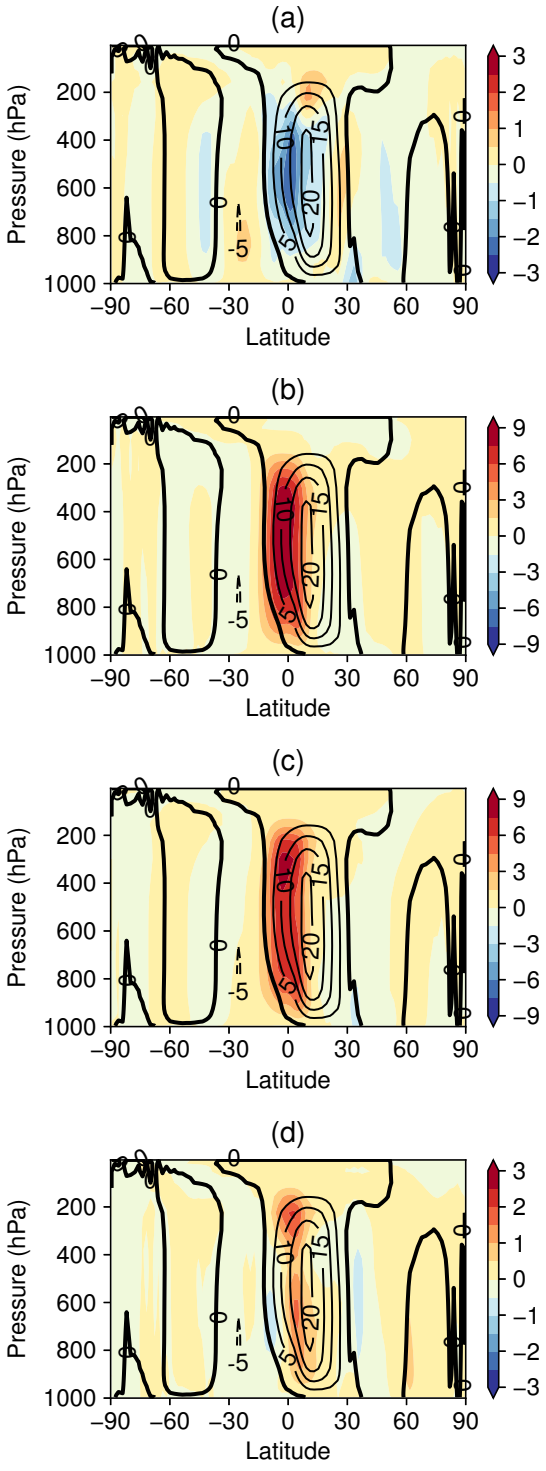



Figure 4.3: Changes in DJF mean meridional streamfunction ($m^2\ s^{-1}$) resulting from (a) a doubling of $CO_2$, (b) a reduction in solar forcing ($M = 4.0$), and (c) the combined forcing. (d) Nonlinearity in the response of meridional streamfunction. The black contours denote the climatological mean from the control run.

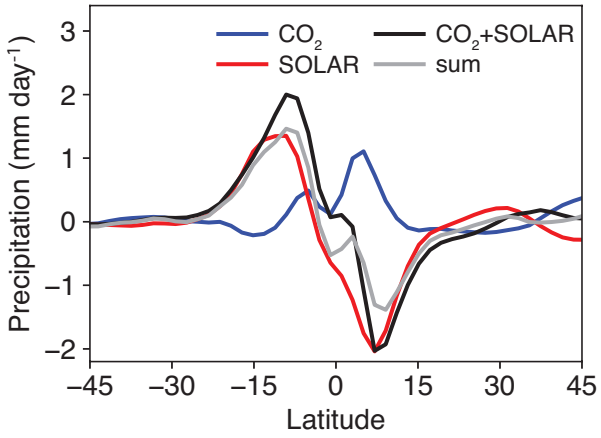



Figure 4.4: Changes in DJF zonal-mean precipitation resulting from a doubling of $CO_2$ (blue), a reduction in solar forcing ($M = 4.0$, red), and the combined forcing (black). The grey line represents the linear sum of precipitation changes.

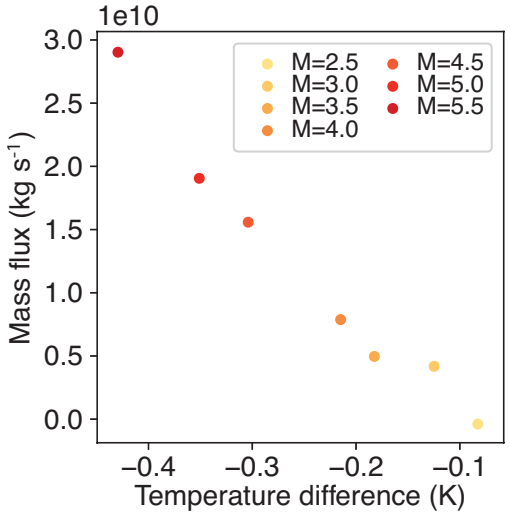



Figure 4.5: The relationship between the nonlinearity in mass flux change at the equator and hemispheric difference (0°-45°N average minus 0°-45°S average) in 850 hPa temperature. Positive mass flux indicates a northward upper level flow.

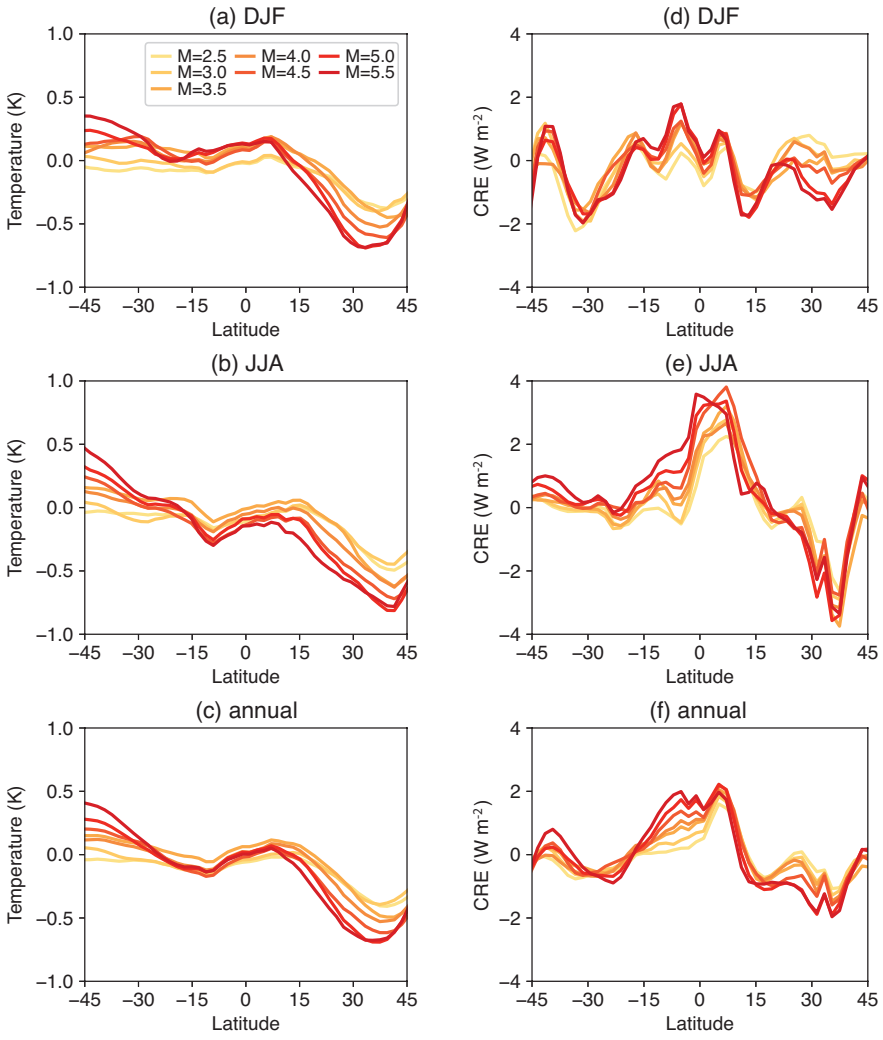



Figure 4.6: Nonlinearity in (a,d) DJF, (b,e) JJA, and (c,f) annual mean responses in (left) 850 hPa temperature and (right) cloud radiative effects.

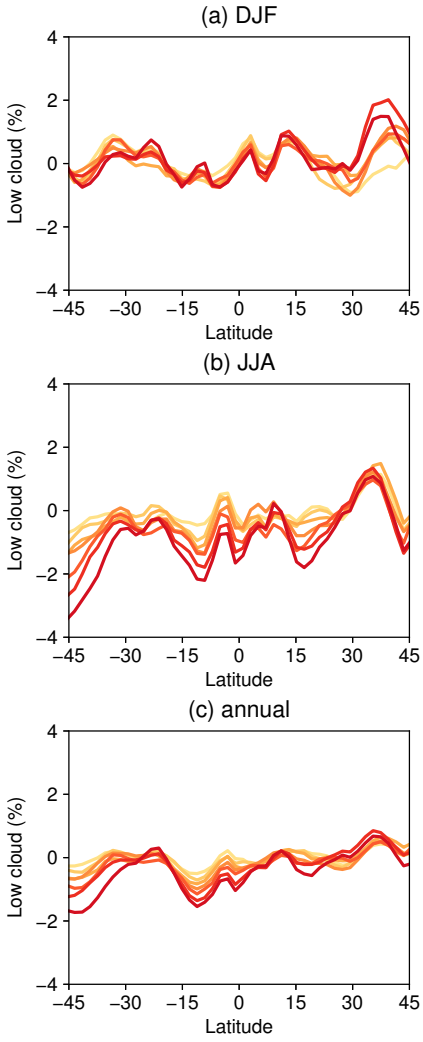



Figure 4.7: Nonlinearity in (a) DJF, (b) JJA, and (c) annual mean responses in low cloud amount.

# Chapter 5

# Constraining aerosol forcing from land surface air temperature records

## 5.1 Introduction

The global land surface air temperature (LSAT) has increased markedly since the 1970s (Compo et al., 2013; Hartmann et al., 2013), and there is growing evidence that anthropogenic forcing has made a substantial contribution to this warming (Bindoff et al., 2013a). The response of land temperature (L) to forcing agents (F) can be approximated as a combination of a fast and a slow component:

$$\delta L = \left( \frac{\partial L}{\partial F}|_O + \frac{\partial L}{\partial O}|_F \frac{\delta O}{\delta F} \right) \delta F. \tag{5.1}$$

The first term in the bracket on the right-hand side of Eq. 5.1 represents the atmospheric-land-only adjustment that is due directly to the forcing, and the second term represents the slow response that is mediated through changes in the ocean state (O). The fast and slow components are simultaneously present in coupled atmosphere-

ocean general circulation models (CGCMs), principal tools used for understanding the influence of anthropogenic forcing on land temperature (Zhang et al., 2006; Jones et al., 2008; Christidis et al., 2010; Knutson et al., 2013). The slow component contains much of the uncertainty in climate sensitivity and is where the forced signals are mixed most strongly with natural variability, which limits the robustness of CGCM results (Shin and Sardeshmukh, 2011; Knutson et al., 2013; Deser et al., 2014).

Atmospheric general circulation models (AGCMs) forced by observed ocean boundary conditions [sea surface temperatures and sea ice concentrations] can be used to separate the fast and slow components of climate response to forcing. The AGCM configuration is well-established and used in the Atmospheric Model Intercomparison Project (AMIP) (Gates et al., 1999). By specifying the ocean state according to observations, one avoids the large uncertainty in climate sensitivity and low-frequency internal variability of the ocean and thus reduces the noise. AGCMs have been used to understand the mechanism of changes in the atmospheric circulation and the hydrological cycle (Deser and Phillips, 2009; Bichet et al., 2011; Bony et al., 2013). This approach, however, has received little attention in the analysis of land temperature since it is generally believed that the ocean state has a strong influence on climate change over land (Compo and Sardeshmukh, 2009; Dommenget, 2009). Some few studies have suggested that the direct (fast) response of global or Northern Hemisphere mean land temperature to anthropogenic forcing is significant (Folland et al., 1998; Andrews, 2014; Paynter and Frölicher, 2015), although an early attempt has shown the anthropogenic signal is not detectable in the spatial pattern of land temperature change over the last half of the 20th century (Sexton et al., 2001). Here we probe the fast component of land warming in recent decades and show that the anthropogenic signal on land temperature change may already emerge from the noise at continental and subcontinental scales. We further isolate the fast

response to aerosols and show that it is helpful for reducing the uncertainty range of aerosol forcing.

## 5.2 Methods

### 5.2.1 Climate data and climate model simulations

We use observed LSAT from the Berkeley Earth Surface Temperatures (BEST), an interpolated dataset based on many preexisting surface air temperature records (Rohde et al., 2013b,a). We compare observations with three sets of historical simulations (1870-2015), each using two Geophysical Fluid Dynamics Laboratory atmospheric model AM2 and AM3. As in AMIP protocols, all simulations use prescribed monthly sea surface temperatures and sea ice concentrations consistent with observations (Taylor et al., 2000). The "ALL_F" experiments follow the AMIP protocol and is forced by the historical radiative forcings of CMIP5 (Taylor et al., 2012) for 1870-2005 extended using Representative Concentration Pathway 4.5 for 2006-2015. The forcings include GHGs, ozone, aerosols, solar forcing, and land use. To separate the fast and slow components, we carry out a set of experiments (NO_F) with all forcing agents held fixed at preindustrial (1860) levels. To isolate the fast response to aerosols, we carry out a third set of experiments (NO_AERO) in which anthropogenic aerosols are fixed at preindustrial levels, while the other forcings evolve in time as in the "ALL_F" experiments. Each experiment consist of five ensemble members of each model to remove effects of internal atmospheric variability.

AM2 uses a finite volume, latitude-longitude dynamic core with a horizontal resolution of $\sim 2^\circ \times 2.5^\circ$ and 24 vertical levels from the surface to $\sim$3 hPa. The shortwave and longwave radiation algorithms are as described in Freidenreich et al. (1999) and Schwarzkopf et al. (1999). Moist convection is parameterized using the relaxed Arakawa-Schubert convection scheme (Moorthi and Suarez, 1992). Stratiform clouds

are prognosed based on Tiedtke (1993), and cloud microphysics are parameterized following Rotstayn (1997) and Rotstayn et al. (2000). Convective planetary boundary layers are parameterized based on Lock et al. (2000), and conventional stability functions dependent on the Richardson number are used for stable layers. Ozone and aerosol concentrations are prescribed in AM2, and only the direct and semi-direct effects of aerosols is included. AM3 uses a cubed-sphere implementation of the finite-volume dynamical core, and has a horizontal resolution of ∼200 km with 48 vertical layers from the surface to ∼1 Pa. Relative to AM2, AM3 includes new parameterizations of deep and shallow cumulus convection (Donner et al., 2001; Bretherton and McCaa, 2004) and a physically-based representation of cloud droplet activation by aerosols (Ming et al., 2007). Subgrid variability of vertical velocities in stratiform clouds is parameterized for droplet activation (Golaz et al., 2011). Ozone and aerosols are simulated interactively based on their emission, chemical production, transport, and dry and wet removal. The treatment of aerosol forcing in AM3 differs significantly from that in AM2, in that AM3 includes direct, semi-direct and indirect effects of aerosols and treats sulfate and hydrophilic black carbon as internally mixed (for radiation). The configurations and performances of AM2 and AM3 have been documented in detail in GAMDT (2004) and Donner et al. (2011), respectively.

### 5.2.2 Statistical analysis

In this paper the LSAT change in recent decades is defined as the 2001-15 average minus the 1961-80 average. The Student's t-test is applied to assess the statistical significance and confidence interval of the observed record and ensemble means. The t-statistic is calculated as:

$$t = \frac{\overline{X}_1 - \overline{X}_2}{S_p \sqrt{\frac{1}{n_1} + \frac{1}{n_2}}},$$

where $\overline{X}_i$ is the mean LSAT and $n_i$ is the number of years, where subscripts $i = 1$ and 2 denote the time periods 1961-80 and 2001-15, respectively. $S_p$ is the pooled estimate of the standard deviation:

$$S_p = \sqrt{\frac{(n_1 - 1)S_1^2 + (n_2 - 1)S_2^2}{n_1 + n_2 - 1}}, \tag{5.2}$$

where $S^2$ is the unbiased estimate of the variance of LSAT. The degree of freedom of the t-test is $n_1 + n_2 - 2$.

A linear contrast test (von Storch and Zwiers, 1999) is conducted for the statistical significance of the difference in LSAT change between observations and ensemble means. In the contrast test, the F-statistic is calculated as:

$$F = \frac{\overline{X}_4 - \overline{X}_3 - (\overline{X}_2 - \overline{X}_1)}{MSW\sqrt{\frac{1}{n_1} + \frac{1}{n_2} + \frac{1}{n_3} + \frac{1}{n_4}}}, \tag{5.3}$$

where $X_1$ and $X_2$ are the 1961-80 and 2001-15 average LSAT from observations, respectively, and $X_3$ and $X_4$ are the 1961-80 and 2001-15 average LSAT from simulations, respectively. MSW is the within mean square error from the one-way analysis of variance (ANOVA) of the four groups of LSAT, and $n_i$ are the number of years in each group ($n_1 = 20$, $n_2 = 15$, $n_3 = 20$, $n_4 = 15$). The calculated F-statistic is then compared with the F distribution with $(1, n_1 + n_2 + n_3 + n_4 - 4)$ degrees of freedom.

## 5.3 Results

Fig. 5.1 compares observed and simulated LSAT over Northern Hemisphere (NH) land in summer and autumn (June to November, JJASON). We focus on these two seasons to avoid the large internal atmospheric variability in winter and spring (Wallace et al., 2012). Observed LSAT shows a clear warming trend since 1980 as well as significant interannual variations, including warming following El Niño events and

cooling following La Niña events and major volcanic eruptions. While NO_F generally captures the warming trend of NH land and most of the interannual variations, it does not show enough warming in recent decades, with clear departures from observations after about 2000. Recent LSAT changes (defined as the 2001-15 average minus the 1961-80 average) over NH from individual ensemble members are shown Fig. 5.2a. None of the individual AM2 or AM3 ensemble members in NO_F can reproduce the observed warming. On average the recent land warming in NO_F is 79% of that in observations (Table 5.1). Hence, assuming the land temperature response to oceanic warming and forcing agents are linearly additive, 21% of the recent warming over NH land can be identified as due to the fast response. The observed NH warming in recent decades is reproduced by the GFDL AGCMs when anthropogenic aerosols are excluded (NO_AERO) (Fig. 5.1b and Table 5.1), suggesting that the fast response to aerosols is small. Since the natural forcing and the forcing due to land-use change are small over the past half century (Skeie et al., 2011; Myhre et al., 2013), the fast response is dominated by an increase in GHGs. The simulated recent NH warming with all forcing agents (ALL_F) is not significantly different from that in NO_AERO or observations (Fig. 5.1c and Table 5.1).

The observed land warming is nearly ubiquitous in the NH (Fig. 5.3a). The difference between NO_F simulated and observed LSAT change is significant over most of the NH land (Figs. 5.3b and 5.3c) and shows distinct spatial patterns. NO_F does not show enough warming in a number of regions including Europe, North Africa, and northern Asia. On the contrary, in some regions such as East Asia and South Asia the warming in NO_F is consistent with or even stronger than that in observations. Figs. 5.2b and 5.2c show observed and model simulated LSAT change in recent years over Europe (38° -66° N, 10° W-50° E) and Asia (8° -38° N, 70° -123° E), respectively. In both AM2 and AM3, recent warming over Europe is underestimated by ∼50% in NO_F (Fig. 5.2b and Table 5.1). Thus the fast component of recent European

warming is comparable to the slow component and cannot be neglected. On the other hand, the difference in LSAT change over Asia between NO_F simulations and observations is not statistically significant (Fig. 5.2c and Table 5.1), indicating that the fast component of recent Asian land warming is small.

In recent decades there have been regional shifts in the global distribution of $SO_2$ emission, the main source of sulfate aerosols. Anthropogenic $SO_2$ emissions have declined steadily in Europe since the 1970s as a result of efforts to improve air quality, while emissions in Asia, especially China and India, have been increased substantially (Smith et al., 2011). The fast response to aerosols becomes evident when examining LSAT changes on subcontinental scales. A clear contrast between Europe and Asia is evident in the difference between NO_AERO and observations (Figs. 5.3d and 5.3e). Recent European warming is underestimated by ∼30% in NO_AERO (Fig. 5.2b and Table 1), indicating that the fast response to aerosols contributes to more than half of the total fast response (∼50%). In contrast, NO_AERO shows more warming over Asia in both AM2 and AM3 (Fig. 5.2c and Table 5.1). It is encouraging to see the similarity in NO_AERO simulated LSAT changes between AM2 and AM3, given the large differences in the representation of physical processes between the two models. If the oceanic influence on land warming (the slow response) and the fast response to non-aerosol forcing are robust across models, one can subtract them from observations to derive the fast response to aerosols. It is promising that the empirically inferred fast aerosol effect on temperature over Europe (warming) and Asia (cooling) from the 1970s to the present is consistent in sign with the opposite emission trends in Europe and Asia over this time period.

These AGCM simulations can be used to explore which set of assumptions about aerosol forcing best fits the observations. Several improvements have been made in the representation of aerosol physics between AM2 and AM3. In AM2 aerosol concentrations are prescribed as monthly means and no indirect effects are included,

while AM3 includes interactive aerosols and aerosol indirect effects. Also, sulfate and hydrophilic black carbon are assumed to be internally mixed (for radiation) in AM3, but externally mixed in AM2. The resulting negative radiative forcing from aerosols in source regions in AM3 is much stronger than that in AM2 (Fig. 5.4). In general the model simulated land warming is closer to observations in ALL_F than in NO_F or NO_AERO (Figs. 5.3e and 5.3f). Including anthropogenic aerosols results in stronger model simulated warming over Europe in recent decades and a better agreement with observations (Fig. 5.2b and Table 5.1). While the ensemble mean of AM3 is closer to observations than AM2, the observed LSAT change falls within the range of ALL_F ensemble members in both two models. Larger differences are found in the fast response to aerosols in Asia between the two models (Fig. 5.2c and Table 5.1). Including time-varying aerosols reduces the warming over Asia in recent decades in AM3, however it has hardly any effect on LSAT change over Asia in AM2. As a result, while AM3 all-forcing runs and observations are in fairly good agreement, all AM2 ensemble members overestimate the recent warming in Asia. The difference in aerosol forcing between AM2 and AM3 may explain the difference in the ALL_F simulated LSAT change over Asia, and to a lesser extent, Europe. The present-day (2001-15 average) aerosol effective radiative forcing (defined as the change in net top-of-atmosphere downward radiative flux after allowing for rapid adjustments) relative to pre-industrial (1860) is -0.3 W $m^{-2}$ and -1.8 W $m^{-2}$ in AM2 and AM3, respectively, which are both near the ends of the range in IPCC AR5 (-1.9 to -0.1 W $m^{-2}$) (Myhre et al., 2013). The fact that the AM3 simulated spatial pattern of recent LSAT changes using the AMIP framework fits the observed record better suggests that the stronger (more negative) aerosol forcing may be more realistic. On the other hand, the global mean aerosol radiation forcing change in recent decades is small in both AM2 and AM3 since the opposite trends in emissions in Europe and Asia nearly balance each other. As a result the recent changes in total anthropogenic forcing are dominated

by the less uncertain GHGs, and both AM2 and AM3 ALL_F simulations reproduce recent changes in NH mean LSAT (Fig. 5.1c).

## 5.4 Discussion and conclusions

Understanding the anthropogenic influence on regional climate change is important for policy making and adaption planning. The ability of the traditional method based on coupled climate models in attribution studies is limited by the strong influence of natural variability. Here we use AGCMs to investigate the fast component of the anthropogenic influence on regional temperature change. Although this fast component of the anthropogenic warming is often thought of as small, we find that it is detectable in the observed warming of Northern Hemisphere land in recent decades. We suggest that the fast response to aerosol forcing can be separated from that of other forcings when focusing on the surface temperature change on subcontinental scales.

Despite an improved understanding of aerosol processes and more observations of aerosol properties in recent years, uncertainties in the radiative effects of aerosols remain the dominant contributor to the overall uncertainty in anthropogenic forcing, and thus the response of the climate system (Boucher et al., 2013). Previous studies have proposed several emergent constraints for aerosol forcing, such as the sensitivity of rain efficiency to aerosols (Wang et al., 2012), recent change in surface solar radiation (Cherian et al., 2014), and the cloud response to volcano eruptions (Malavelle et al., 2017). Observations of all these metrics are spatially and temporally inhomogeneous and suffer from large uncertainty and natural variability. Here we make a first attempt to constrain historical aerosol forcing from sustained observations of LSAT using AGCMs. The lower internal variability in AGCMs allows one to analyze observed climate change on smaller spatial scales and shorter time scales. Assuming

the models represent the fast response to other forcings correctly, we infer a significant fast response of LSAT to aerosol forcing changes over recent decades in Europe and Asia, although not over the entire Northern Hemisphere. We find that the model with a larger magnitude of aerosol forcing better matches the observed LSAT changes over Asia, suggesting that the lowest end of the range of aerosol forcing in present assessments is very unlikely. The implications on aerosol forcing would be more reliable if this kind of AGCM simulations, with and without aerosol forcing, were made available for multiple climate models.

Table 5.1: Comparison of observed and simulated LSAT changes (K) in recent decades shown as the 2001-15 average minus the 1961-80 average. All simulated data are based on ensemble means. An asterisk indicates that the difference between simulated and observed LSAT changes is significant at $P < 0.1$.

| | OBS | AM2 | | | AM3 | | |
|---|---|---|---|---|---|---|---|
| | | NO_F | NO_AERO | ALL_F | NO_F | NO_AERO | ALL_F |
| NH | 0.99 | 0.82* | 1.03 | 1.07 | 0.74* | 0.99 | 1.05 |
| Europe | 1.16 | 0.60* | 0.83* | 0.98 | 0.62* | 0.86* | 1.15 |
| Asia | 0.54 | 0.67 | 0.88* | 0.86* | 0.66 | 0.78* | 0.60 |

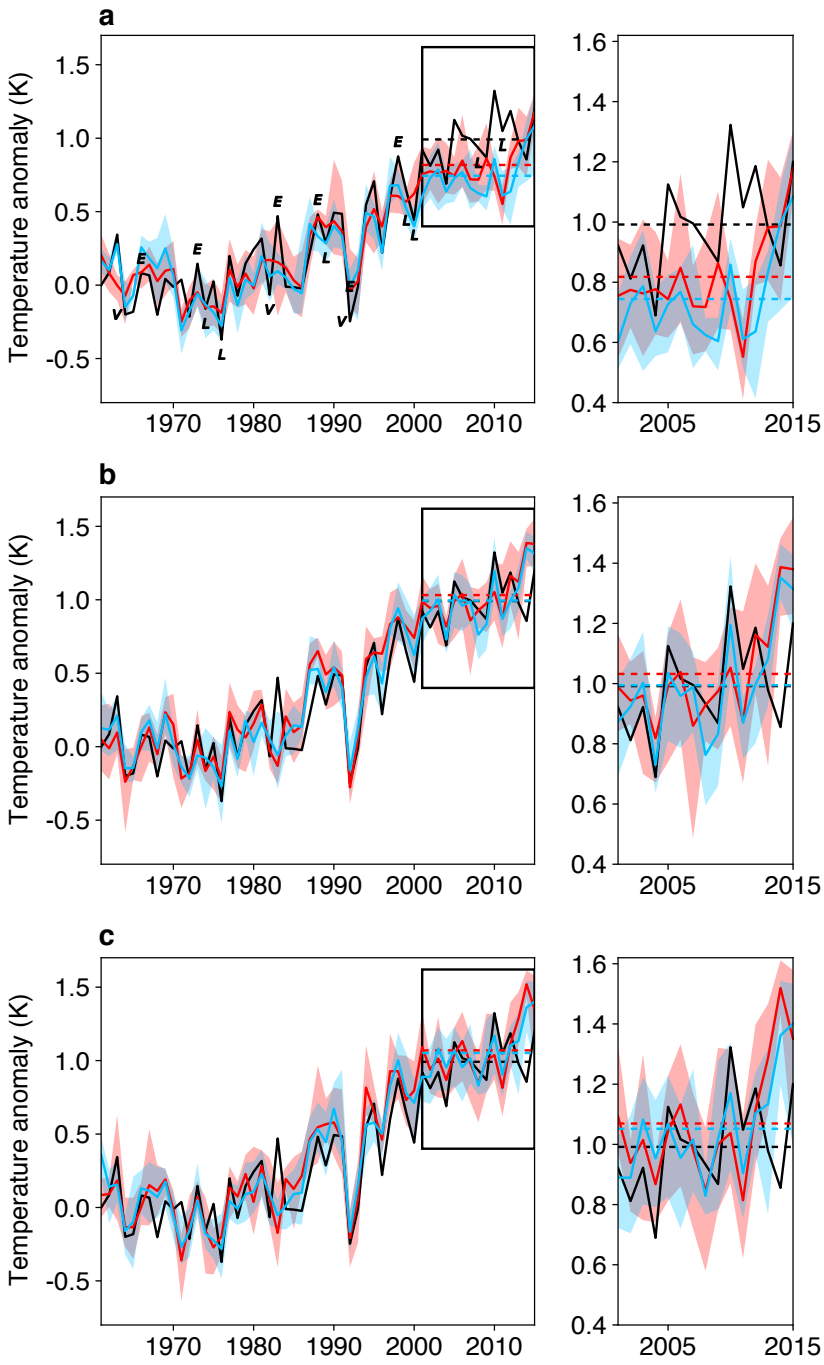



Figure 5.1: Time series (1961-2015) of JJASON mean NH LSAT anomalies from observations (black solid lines), (a)NO_F, (b) NO_AERO, and (c) ALL_F. Anomalies are deviations with respect to the 1961-80 reference period. The colored solid line represents the ensemble mean and the shading represents the full ensemble range (AM2 in red, AM3 in blue). The dashed line represents the 2001-15 average. Strong El Nino (E), La Nina (L), and volcanic eruptions (V) are marked in the figure. The right column shows an enlarged plot of 2001-15 temperature anomalies.

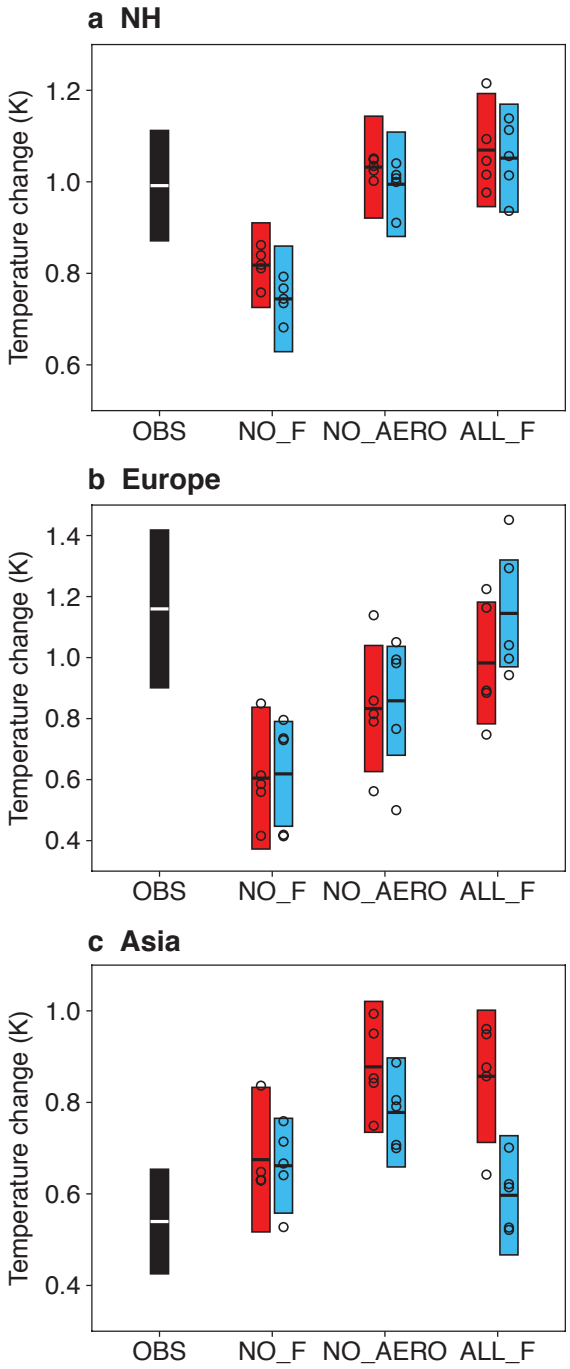



Figure 5.2: JJASON mean LSAT changes over (a) NH, (b) Europe (38° -66° N, 10° W-50° E), and (c) Asia (8° -38° N, 70° -123° E) in recent decades shown as the 2001-15 average minus the 1961-80 average from observations (black), AM2 (red), and AM3 (blue). Box shows the mean temperature change (center line) and its 95% confidence interval. Black circles represent LSAT changes from individual ensemble numbers.

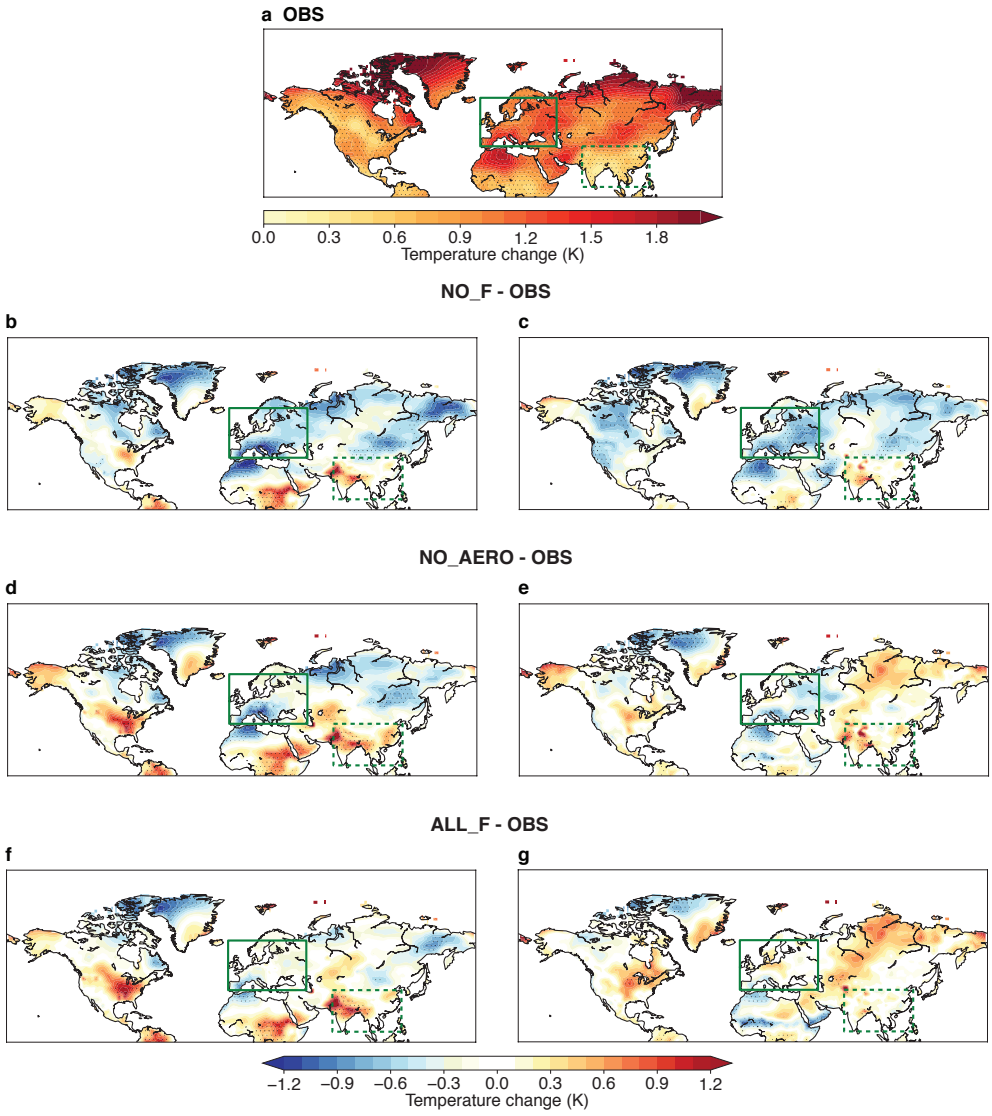



Figure 5.3: (a) Observed and (b-g) observed minus model simulated JJASON mean surface air temperature change in recent decades shown as the 2001-15 average minus the 1961-80 average. b, d, and f show results from AM2; c, e, and g show results from AM3. Stippling indicates regions exceeding 95% statistical confidence. Solid and dashed rectangles denote Europe and Asia used for averaging in Fig. 5.2.

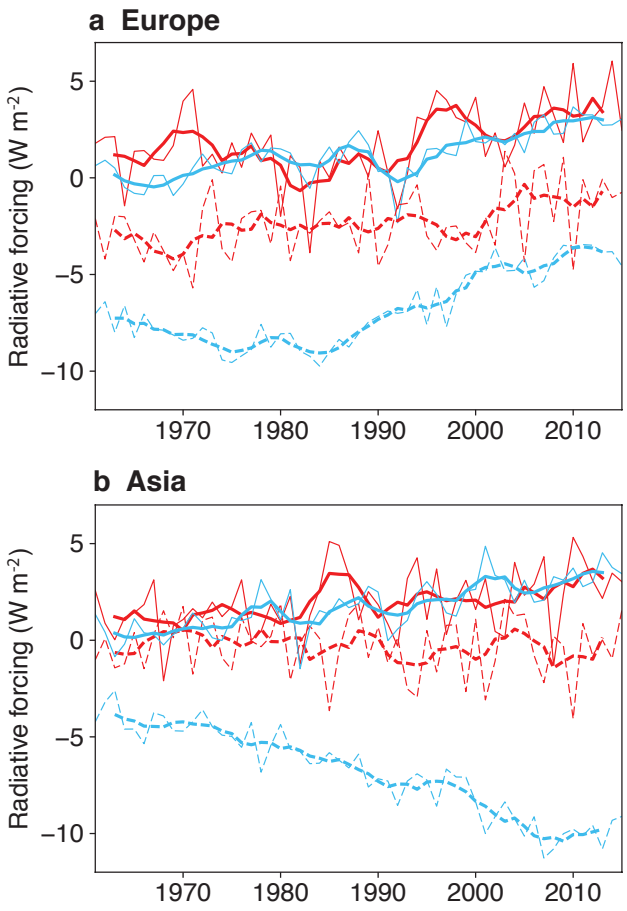



Figure 5.4: Time series (1961-2015) of JJASON mean non-aerosol (solid) and aerosol (dashed) effective radiative forcing over (a) Europe and (b) Asia. Red and blue lines represent AM2 and AM3, respectively. Thick and thin lines represent five-year running mean and annual mean, respectively.

# Chapter 6

# Conclusions

## 6.1 Summary and Implications

Anthropogenic aerosols have a strong influence on atmospheric circulation and climate change at both global and regional scales. Using comprehensive general circulation model simulations, along with observations and theoretical understanding, this dissertation investigates the atmospheric transport and removal processes of aerosols (Chapter 2), as well as the impacts of aerosols on large-scale atmospheric circulation (Chapters 3 and 4) and regional climate change over the twentieth century (Chapter 5).

Chapter 2 focuses on Arctic haze, which has a distinct seasonal cycle with peak concentrations in winter but pristine conditions in summer. It is demonstrated that the Geophysical Fluid Dynamics Laboratory (GFDL) atmospheric model, AM3, can reproduce the observed seasonality of Arctic black carbon (BC), an important component of Arctic haze. The model is used to study how large-scale circulation and removal drive the seasonal cycle of Arctic BC. It is found that despite large seasonal shifts in the general circulation pattern, the transport of BC into the Arctic varies little throughout the year. The seasonal cycle of Arctic BC is attributed mostly to

variations in the factors controlling wet removal, namely the hydrophilic fraction of BC and wet deposition efficiency of hydrophilic BC. Specifically, a confluence of low hydrophilic fraction and weak wet deposition, owing to slower aging process and less efficient mixed-phase cloud scavenging, respectively, is responsible for the wintertime peak of BC. The transition to low BC in summer is the consequence of a gradual increase in the wet deposition efficiency, whereas the increase of BC in late fall can be explained by a sharp decrease in the hydrophilic fraction. The results suggest that future changes in the aging and wet deposition processes can potentially alter the concentrations of Arctic aerosols and their climate effects.

Chapter 3 examines how aerosol absorption affects the extratropical circulation by analyzing the response to a globally uniform increase in BC simulated with an atmospheric general circulation model (AGCM) forced by prescribed sea surface temperatures. The model includes aerosol direct and semi-direct effects, but not indirect or cloud-absorption effects. BC-induced heating in the free troposphere stabilizes the mid-latitude atmospheric column, which results in less energetic baroclinic eddies and thus reduced meridional energy transport at mid-latitudes. Upper tropospheric BC also decreases the meridional temperature gradient on the equatorward flank of the tropospheric jet and yields a weakening and poleward shift of the jet, while boundary layer BC has no significant influence on the large-scale circulation since most of the heating is diffused by turbulence in the boundary layer. The effectiveness of BC in altering circulation generally increases with height. It is found that dry baroclinic eddy theories can explain most of the extratropical response to free troposphere BC. Specifically, the decrease in vertical eddy heat flux related to a more stable atmosphere is the main mechanism for re-establishing atmospheric energy balance in the presence of BC-induced heating. Similar temperature responses are found in a dry idealized model, which further confirms the dominant role of baroclinic eddies in driving the extratropical circulation changes. The strong atmospheric-only response to

BC suggests that absorbing aerosols are capable of altering synoptic-scale weather patterns. The height dependence of the atmospheric response to BC highlights the importance of better constraining model-simulated aerosol vertical distributions with satellite and field measurements.

Chapter 4 examines the nonlinearity in the climate impacts of greenhouse gases and scattering aerosols by analyzing the response to a doubling of $CO_2$ and a zonally symmetric solar forcing perturbation simulated with an AGCM coupled to a slab ocean model. The solar forcing has a similar latitudinal variation to the realistic aerosol forcing. The boreal winter zonal mean circulation response to solar forcing is characterized by an equatorward shift of the subtropical jet and the intertropical convergence zone, and a strengthening of the Hadley Cell. When forced by $CO_2$ and solar forcing simultaneously, the model simulated warming is less (more) than the linear sum of the response to individual forcing in the Northern (Southern) Hemisphere. As a result, a significant nonlinearity arises in the response of the subtropical jet and the Hadley Cell. The nonlinearity largely comes from cloud radiative responses and increases with the magnitude of solar forcing. The results suggest that the nonlinear climate response to greenhouse gas and aerosol forcings is a robust feature that cannot be neglected in climate change attribution studies.

Chapter 5 applies AGCMs forced by observed sea surface temperatures and sea ice concentrations to decompose the historical land warming into a fast atmospheric-land-only component and a slow component mediated by the ocean. By prescribing the ocean state, the uncertainty in climate sensitivity and natural variability is reduced, and the slow component appears to be robust across models. We find that the fast component of the anthropogenic warming, which is often thought of as small, accounts for more than 20% of observed warming of Northern Hemisphere land during summer and autumn in recent decades. The fast response to anthropogenic aerosols inferred from observations has a warming effect in Europe but a cooling effect in Asia,

consistent with the regional shift in aerosol emissions in recent years. By comparing two GFDL AGCMs, AM2 and AM3, we suggest that the magnitude of aerosol forcing is likely towards the high end of the present model range.

## 6.2 Limitations and Future Work

While the response of atmospheric circulation to greenhouse gases has been studied extensively in the literature, the circulation change due to aerosols has received relatively little attention. The impacts of aerosols are complicated and uncertain due to the interplay between aerosol emission, transport and removal processes, as well as the complex aerosol-radiation interactions, aerosol-cloud interactions and air-sea coupling. To simplify the problem, in Chapters 3 and 4 we analyze the atmospheric circulation response to globally uniform and zonally symmetric forcings, respectively. The idealized forcing is helpful for gaining a theoretical understanding of the physical mechanisms driving the response, however it is not representative of present-day aerosols or any future scenario. Our results may therefore underestimate the effect of the spatial heterogeneity of aerosols, such as the change in stationary eddies (Held et al., 2002; Ming et al., 2011). Evaluating the circulation response to realistic aerosol forcing would be a valuable step forward in understanding the climate impacts of aerosols.

The climate response to an external forcing involves a variety of time scales and can be thought as consisting of a fast, an intermediate and a slow component (e.g., Manabe et al., 1990; Held et al., 2010). The fast atmospheric-land only response occurs with a fixed ocean state and has time scales of a month or less. The intermediate response has time scales of a few years in which the shallow oceanic mixed layer reaches equilibrium, and the much more slowly evolving response is a manifestation of the change in the deep ocean. Section 3 focuses on the fast component using an AGCM with fixed

sea surface temperatures, while Section 4 focuses on the equilibrium response using an AGCM coupled to a slab ocean model. The results in both sections differ from the transient climate response, which is dominated by the intermediate component, and thus cannot be applied directly to understand observed historical changes in atmospheric circulation. Evaluating the aerosol impacts in fully coupled atmosphere-ocean general circulation models would be helpful for attributing observed circulation changes to aerosols.

The results in this dissertation are based on simulations with several GFDL models, and the robustness of the results needs to be examined with additional models. Many processes associated with aerosol-climate interactions that are explored in this dissertation, such as aerosol hygroscopic growth and microphysics (Section 2), boundary layer dynamics (Section 3) and cumulus convection (Section 4), operate at scales that are much smaller than the resolution of current models and are therefore parameterized in a relatively simple way. It remains to be seen whether other climate models with different parameterization schemes yield similar impacts of aerosols. In recent years, an emerging class of models has endeavored to represent the atmospheric circulation at cloud-resolving scales (a few kilometers) (e.g., Tomita and Satoh, 2004; Pressel et al., 2015; Zängl et al., 2015), and it would be interesting to evaluate the similarities and differences in the atmospheric circulation response to aerosols between these high-resolution models and traditional climate models. In addition, targeted observations and laboratory experiments would greatly complement modeling studies and improve our understanding of aerosol impacts in the real world.

The uncertainty in aerosol forcing is one of the greatest challenges associated with projecting future climate change. Chapter 5 makes an attempt to empirically constrain historical aerosol forcing from the fast component of land surface air temperature change in recent decades. The decomposition of recent land warming is limited to some extent by the internal atmospheric variability, as shown by the large varia-

tion among the ensemble members. Larger ensembles and simulations with multiple climate models would be desirable for examining this kind of decomposition more carefully in different regions. Similar approaches could be applied to analyze other climate variables with a stronger anthropogenic signal, such as precipitation (e.g., Li et al., 2018). The forced signal in many aspects of the climate system is expected to emerge from the background of natural climate variability in the near future (Bindoff et al., 2013b). Integrating global observations and climate model simulations may lead to a better quantification of the role of aerosols in the Earth's climate system.

# Bibliography


Ackerman, T. P., 1977: A Model of the Effect of Aerosols on Urban Climates with Particular Applications to the Los Angeles Basin. *Journal of the Atmospheric Sciences*, **34 (3)**, 531–547, doi:10.1175/1520-0469(1977)034⟨0531:AMOTEO⟩2.0.CO;2.

Albrecht, B. A., 1989: Aerosols, Cloud Microphysics, and Fractional Cloudiness. *Science*, **245 (4923)**, 1227–1230, doi:10.1126/science.245.4923.1227.

Allen, R. J., and O. Ajoku, 2016: Future aerosol reductions and widening of the northern tropical belt. *Journal of Geophysical Research: Atmospheres*, **121 (12)**, 6765–6786, doi:10.1002/2016JD024803.

Allen, R. J., and W. Landuyt, 2014: The vertical distribution of black carbon in CMIP5 models: Comparison to observations and the importance of convective transport. *Journal of Geophysical Research: Atmospheres*, **119 (8)**, 4808–4835, doi:10.1002/2014JD021595.

Allen, R. J., and S. C. Sherwood, 2011: The impact of natural versus anthropogenic aerosols on atmospheric circulation in the Community Atmosphere Model. *Climate Dynamics*, **36 (9-10)**, 1959–1978, doi:10.1007/s00382-010-0898-8.

Allen, R. J., S. C. Sherwood, J. R. Norris, and C. S. Zender, 2012: The equilibrium response to idealized thermal forcings in a comprehensive GCM: implications for recent tropical expansion. *Atmospheric Chemistry and Physics*, **12 (10)**, 4795–4816, doi:10.5194/acp-12-4795-2012.

Anderson, J. L., and Coauthors, 2004: The New GFDL Global Atmosphere and Land Model AM2LM2: Evaluation with Prescribed SST Simulations. *Journal of Climate*, **17 (24)**, 4641–4673, doi:10.1175/JCLI-3223.1.

Andrews, T., 2014: Using an AGCM to Diagnose Historical Effective Radiative Forcing and Mechanisms of Recent Decadal Climate Change. *Journal of Climate*, **27 (3)**, 1193–1209, doi:10.1175/JCLI-D-13-00336.1.

Ban-Weiss, G. A., L. Cao, G. Bala, and K. Caldeira, 2012: Dependence of climate forcing and response on the altitude of black carbon aerosols. *Climate Dynamics*, **38 (5-6)**, 897–911, doi:10.1007/s00382-011-1052-y.

Barnes, E. A., and J. A. Screen, 2015: The impact of Arctic warming on the midlatitude jet-stream: Can it? Has it? Will it? *Wiley Interdisciplinary Reviews: Climate Change*, **6 (3)**, 277–286, doi:10.1002/wcc.337.

Barnett, T. P., J. C. Adam, and D. P. Lettenmaier, 2005: Potential impacts of a warming climate on water availability in snow-dominated regions. *Nature*, **438 (7066)**, 303–309, doi:10.1038/nature04141.

Barrie, L. A., 1986: Arctic air pollution: An overview of current knowledge. *Atmospheric Environment (1967)*, **20 (4)**, 643–663, doi:10.1016/0004-6981(86)90180-0.

Barry, L., G. C. Craig, and J. Thuburn, 2002: Poleward heat transport by the atmospheric heat engine. *Nature*, **415 (6873)**, 774–777, doi:10.1038/415774a.

Bichet, A., M. Wild, D. Folini, and C. Schär, 2011: Global precipitation response to changing forcings since 1870. *Atmospheric Chemistry and Physics*, **11 (18)**, 9961–9970, doi:10.5194/acp-11-9961-2011.

Bindoff, N., and Coauthors, 2013a: Detection and Attribution of Climate Change: from Global to Regional. *Climate Change 2013 - The Physical Science Basis*, Intergovernmental Panel on Climate Change, Ed., Cambridge University Press, Cambridge, 867–952, doi:10.1017/CBO9781107415324.022.

Bindoff, N. L., and Coauthors, 2013b: Near-term Climate Change: Projections and Predictability. *Climate Change 2013 - The Physical Science Basis*, Intergovernmental Panel on Climate Change, Ed., Cambridge University Press, Cambridge, 953–1028, doi:10.1017/CBO9781107415324.023.

Bolin, B., and C. D. Keeling, 1963: Large-scale atmospheric mixing as deduced from the seasonal and meridional variations of carbon dioxide. *Journal of Geophysical Research*, **68 (13)**, 3899–3920, doi:10.1029/JZ068i013p03899.

Bollasina, M., S. Nigam, and K.-M. Lau, 2008: Absorbing Aerosols and Summer Monsoon Evolution over South Asia: An Observational Portrayal. *Journal of Climate*, **21 (13)**, 3221–3239, doi:10.1175/2007JCLI2094.1.

Bond, T. C., and Coauthors, 2013: Bounding the role of black carbon in the climate system: A scientific assessment. *Journal of Geophysical Research: Atmospheres*, **118 (11)**, 5380–5552, doi:10.1002/jgrd.50171.

Bony, S., G. Bellon, D. Klocke, S. Sherwood, S. Fermepin, and S. Denvil, 2013: Robust direct effect of carbon dioxide on tropical circulation and regional precipitation. *Nature Geoscience*, **6 (6)**, 447–451, doi:10.1038/ngeo1799.

Boucher, O., and Coauthors, 2013: Clouds and Aerosols. *Climate Change 2013 - The Physical Science Basis*, Intergovernmental Panel on Climate Change, Ed., Cambridge University Press, Cambridge, 571–658, doi:10.1017/CBO9781107415324.016.

Bourgeois, Q., and I. Bey, 2011: Pollution transport efficiency toward the Arctic: Sensitivity to aerosol scavenging and source regions. *Journal of Geophysical Research*, **116 (D8)**, D08 213, doi:10.1029/2010JD015096.

Bretherton, C. S., and J. R. McCaa, 2004: A New Parameterization for Shallow Cumulus Convection and Its Application to Marine Subtropical Cloud-Topped Boundary Layers. Part II: Regional Simulations of Marine Boundary Layer Clouds. *Monthly Weather Review*, **132 (4)**, 883–896, doi:10.1175/1520-0493(2004)132⟨0883:ANPFSC⟩2.0.CO;2.

Browse, J., K. S. Carslaw, S. R. Arnold, K. Pringle, and O. Boucher, 2012: The scavenging processes controlling the seasonal cycle in Arctic sulphate and black carbon aerosol. *Atmospheric Chemistry and Physics*, **12 (15)**, 6775–6798, doi:10.5194/acp-12-6775-2012.

Butler, A. H., D. W. J. Thompson, and R. Heikes, 2010: The Steady-State Atmospheric Circulation Response to Climate Change-like Thermal Forcings in a Simple General Circulation Model. *Journal of Climate*, **23 (13)**, 3474–3496, doi:10.1175/2010JCLI3228.1.

Carmichael, G. R., and Coauthors, 2009: Asian Aerosols: Current and Year 2030 Distributions and Implications to Human Health and Regional Climate Change. *Environmental Science & Technology*, **43 (15)**, 5811–5817, doi:10.1021/es8036803.

Chen, G., I. M. Held, and W. a. Robinson, 2007: Sensitivity of the Latitude of the Surface Westerlies to Surface Friction. *Journal of the Atmospheric Sciences*, **64 (8)**, 2899–2915, doi:10.1175/JAS3995.1.

Chen, G., J. Lu, and D. M. W. Frierson, 2008: Phase Speed Spectra and the Latitude of Surface Westerlies: Interannual Variability and Global Warming Trend. *Journal of Climate*, **21 (22)**, 5942–5959, doi:10.1175/2008JCLI2306.1.

Chen, G., and A. Plumb, 2014: Effective Isentropic Diffusivity of Tropospheric Transport. *Journal of the Atmospheric Sciences*, **71 (9)**, 3499–3520, doi:10.1175/JAS-D-13-0333.1.

Chen, G., and P. Zurita-Gotor, 2008: The Tropospheric Jet Response to Prescribed Zonal Forcing in an Idealized Atmospheric Model. *Journal of the Atmospheric Sciences*, **65 (7)**, 2254–2271, doi:10.1175/2007JAS2589.1.

Cherian, R., J. Quaas, M. Salzmann, and M. Wild, 2014: Pollution trends over Europe constrain global aerosol forcing as simulated by climate models. *Geophysical Research Letters*, **41 (6)**, 2176–2181, doi:10.1002/2013GL058715.

Christidis, N., P. A. Stott, F. W. Zwiers, H. Shiogama, and T. Nozawa, 2010: Probabilistic estimates of recent changes in temperature: a multi-scale attribution analysis. *Climate Dynamics*, **34 (7-8)**, 1139–1156, doi:10.1007/s00382-009-0615-7.

Christoudias, T., A. Pozzer, and J. Lelieveld, 2012: Influence of the North Atlantic Oscillation on air pollution transport. *Atmospheric Chemistry and Physics*, **12 (2)**, 869–877, doi:10.5194/acp-12-869-2012.

Clark, S. K., Y. Ming, I. M. Held, and P. J. Phillipps, 2018: The role of the water vapor feedback in the ITCZ response to hemispherically asymmetric forcings. *Journal of Climate*, doi:10.1175/JCLI-D-17-0723.1.

Compo, G. P., and P. D. Sardeshmukh, 2009: Oceanic influences on recent continental warming. *Climate Dynamics*, **32 (2-3)**, 333–342, doi:10.1007/s00382-008-0448-9.

Compo, G. P., P. D. Sardeshmukh, J. S. Whitaker, P. Brohan, P. D. Jones, and C. McColl, 2013: Independent confirmation of global land warming without the use of station temperatures. *Geophysical Research Letters*, **40 (12)**, 3170–3174, doi:10.1002/grl.50425.

Cozic, J., S. Mertes, B. Verheggen, D. J. Cziczo, S. J. Gallavardin, S. Walter, U. Baltensperger, and E. Weingartner, 2008: Black carbon enrichment in atmospheric ice particle residuals observed in lower tropospheric mixed phase clouds. *Journal of Geophysical Research*, **113 (D15)**, D15 209, doi:10.1029/2007JD009266.

de Leeuw, G., E. L. Andreas, M. D. Anguelova, C. W. Fairall, E. R. Lewis, C. O'Dowd, M. Schulz, and S. E. Schwartz, 2011: Production flux of sea spray aerosol. *Reviews of Geophysics*, **49 (2)**, RG2001, doi:10.1029/2010RG000349.

Deser, C., and A. S. Phillips, 2009: Atmospheric Circulation Trends, 19502000: The Relative Roles of Sea Surface Temperature Forcing and Direct Atmospheric Radiative Forcing. *Journal of Climate*, **22 (2)**, 396–413, doi:10.1175/2008JCLI2453.1.

Deser, C., A. S. Phillips, M. A. Alexander, and B. V. Smoliak, 2014: Projecting North American Climate over the Next 50 Years: Uncertainty due to Internal Variability*. *Journal of Climate*, **27 (6)**, 2271–2296, doi:10.1175/JCLI-D-13-00451.1.

Dommenget, D., 2009: The Ocean's Role in Continental Climate Variability and Change. *Journal of Climate*, **22 (18)**, 4939–4952, doi:10.1175/2009JCLI2778.1.

Donner, L. J., C. J. Seman, R. S. Hemler, and S. Fan, 2001: A Cumulus Parameterization Including Mass Fluxes, Convective Vertical Velocities, and Mesoscale Effects: Thermodynamic and Hydrological Aspects in a General Circulation Model. *Journal of Climate*, **14 (16)**, 3444–3463, doi:10.1175/1520-0442(2001)014⟨3444:ACPIMF⟩2.0.CO;2.

Donner, L. J., and Coauthors, 2011: The Dynamical Core, Physical Parameterizations, and Basic Simulation Characteristics of the Atmospheric Component AM3 of the GFDL Global Coupled Model CM3. *Journal of Climate*, **24 (13)**, 3484–3519, doi:10.1175/2011JCLI3955.1.

Eckhardt, S., and Coauthors, 2003: The North Atlantic Oscillation controls air pollution transport to the Arctic. *Atmospheric Chemistry and Physics*, **3 (5)**, 1769–1778, doi:10.5194/acp-3-1769-2003.

Eckhardt, S., and Coauthors, 2015: Current model capabilities for simulating black carbon and sulfate concentrations in the Arctic atmosphere: a multi-model evaluation using a comprehensive measurement data set. *Atmospheric Chemistry and Physics*, **15 (16)**, 9413–9433, doi:10.5194/acp-15-9413-2015.

Eleftheriadis, K., S. Vratolis, and S. Nyeki, 2009: Aerosol black carbon in the European Arctic: Measurements at Zeppelin station, Ny-Ålesund, Svalbard from 1998-2007. *Geophysical Research Letters*, **36 (2)**, doi:10.1029/2008GL035741.

Fan, S.-M., and Coauthors, 2012: Inferring ice formation processes from global-scale black carbon profiles observed in the remote atmosphere and model simulations. *Journal of Geophysical Research*, **117 (D23)**, D23 205, doi:10.1029/2012JD018126.

Feichter, J., E. Roeckner, U. Lohmann, and B. Liepert, 2004: Nonlinear aspects of the climate response to Greenhouse gas and aerosol forcing. *Journal of Climate*, doi:10.1175/1520-0442(2004)017⟨2384:NAOTCR⟩2.0.CO;2.

Fiore, A. M., and Coauthors, 2012: Global air quality and climate. *Chemical Society Reviews*, **41 (19)**, 6663, doi:10.1039/c2cs35095e.

Fischer-Bruns, I., D. F. Banse, and J. Feichter, 2009: Future impact of anthropogenic sulfate aerosol on North Atlantic climate. *Climate Dynamics*, **32 (4)**, 511–524, doi:10.1007/s00382-008-0458-7.

Folland, C. K., D. M. H. Sexton, D. J. Karoly, C. E. Johnson, D. P. Rowell, and D. E. Parker, 1998: Influences of anthropogenic and oceanic forcing on recent climate change. *Geophysical Research Letters*, **25 (3)**, 353–356, doi:10.1029/97GL03701.

Freidenreich, S. M., and V. Ramaswamy, 1999: A new multiple-band solar radiative parameterization for general circulation models. *Journal of Geophysical Research: Atmospheres*, **104 (D24)**, 31 389–31 409, doi:10.1029/1999JD900456.

Friedman, B., G. Kulkarni, J. Beránek, A. Zelenyuk, J. A. Thornton, and D. J. Cziczo, 2011: Ice nucleation and droplet formation by bare and coated soot particles. *Journal of Geophysical Research*, **116 (D17)**, D17 203, doi:10.1029/2011JD015999.

Frierson, D. M. W., 2008: Midlatitude Static Stability in Simple and Comprehensive General Circulation Models. *Journal of the Atmospheric Sciences*, **65 (3)**, 1049–1062, doi:10.1175/2007JAS2373.1.

Gallagher, M. W., 2002: Measurements and parameterizations of small aerosol deposition velocities to grassland, arable crops, and forest: Influence of surface roughness length on deposition. *Journal of Geophysical Research*, **107 (D12)**, 4154, doi:10.1029/2001JD000817.

Garrett, T. J., S. Brattström, S. Sharma, D. E. J. Worthy, and P. Novelli, 2011: The role of scavenging in the seasonal transport of black carbon and sulfate to the Arctic. *Geophysical Research Letters*, **38 (16)**, doi:10.1029/2011GL048221.

Garrett, T. J., and L. L. Verzella, 2008: LOOKING BACK: An Evolving History of Arctic Aerosols. *Bulletin of the American Meteorological Society*, **89 (3)**, 299–302, doi:10.1175/BAMS-89-3-299.

Gates, W. L., and Coauthors, 1999: An Overview of the Results of the Atmospheric Model Intercomparison Project (AMIP I). *Bulletin of the American Meteorological Society*, **80 (1)**, 29–55, doi:10.1175/1520-0477(1999)080⟨0029:AOOTRO⟩2.0.CO;2.

Ginoux, P., J. M. Prospero, T. E. Gill, N. C. Hsu, and M. Zhao, 2012: Global-scale attribution of anthropogenic and natural dust sources and their emission rates based on MODIS Deep Blue aerosol products. *Reviews of Geophysics*, **50 (3)**, doi: 10.1029/2012RG000388.

Golaz, J.-C., M. Salzmann, L. J. Donner, L. W. Horowitz, Y. Ming, and M. Zhao, 2011: Sensitivity of the Aerosol Indirect Effect to Subgrid Variability in the Cloud Parameterization of the GFDL Atmosphere General Circulation Model AM3. *Journal of Climate*, **24 (13)**, 3145–3160, doi:10.1175/2010JCLI3945.1.

Green, J. S. A., 1971: Transfer properties of the large-scale eddies and the general circulation of the atmosphere. *Quarterly Journal of the Royal Meteorological Society*, **97 (414)**, 579–580, doi:10.1002/qj.49709741422.

Hall, N. M. J., B. J. Hoskins, P. J. Valdes, and C. a. Senior, 1994: Storm tracks in a high-resolution GCM with doubled carbon dioxide. *Quarterly Journal of the Royal Meteorological Society*, **120 (519)**, 1209–1230, doi:10.1002/qj.49712051905.

Hansen, J., 2005: Efficacy of climate forcings. *Journal of Geophysical Research*, **110 (D18)**, D18 104, doi:10.1029/2005JD005776.

Hartmann, D. J., and Coauthors, 2013: Observations: Atmosphere and Surface. *Climate Change 2013 - The Physical Science Basis*, Intergovernmental Panel on Climate Change, Ed., Cambridge University Press, Cambridge, 159–254, doi:10.1017/CBO9781107415324.008.

Haywood, J. M., and V. Ramaswamy, 1998: Global sensitivity studies of the direct radiative forcing due to anthropogenic sulfate and black carbon aerosols. *Journal of Geophysical Research: Atmospheres*, **103 (D6)**, 6043–6058, doi:10.1029/97JD03426.

Haywood, J. M., V. Ramaswamy, and B. J. Soden, 1999: Tropospheric aerosol climate forcing in clear-sky satellite observations over the oceans. *Science*, **283 (5406)**, 1299–1303, doi:10.1126/science.283.5406.1299.

Held, I. M., 1982: On the Height of the Tropopause and the Static Stability of the Troposphere. *Journal of the Atmospheric Sciences*, **39 (2)**, 412–417, doi:10.1175/1520-0469(1982)039⟨0412:OTHOTT⟩2.0.CO;2.

Held, I. M., 1999: The macroturbulence of the troposphere. *Tellus A: Dynamic Meteorology and Oceanography*, **51 (1)**, 59–70, doi:10.3402/tellusa.v51i1.12306.

Held, I. M., and V. D. Larichev, 1996: A Scaling Theory for Horizontally Homogeneous, Baroclinically Unstable Flow on a Beta Plane. *Journal of the Atmospheric Sciences*, **53 (7)**, 946–952, doi:10.1175/1520-0469(1996)053⟨0946:ASTFHH⟩2.0.CO;2.

Held, I. M., and T. Schneider, 1999: The Surface Branch of the Zonally Averaged Mass Transport Circulation in the Troposphere. *Journal of the Atmospheric Sciences*, **56**, 1688–1697, doi:http://dx.doi.org/10.1175/1520-0469(1999)056⟨1688:TSBOTZ⟩2.0.CO;2.

Held, I. M., and M. J. Suarez, 1994: A Proposal for the Intercomparison of the Dynamical Cores of Atmospheric General Circulation Models. *Bulletin of the American Meteorological Society*, **75 (10)**, 1825–1830, doi:10.1175/1520-0477(1994)075⟨1825:APFTIO⟩2.0.CO;2.

Held, I. M., M. Ting, and H. Wang, 2002: Northern winter stationary waves: Theory and modeling. *Journal of Climate*, **15 (16)**, 2125–2144, doi:10.1175/1520-0442(2002)015⟨2125:NWSWTA⟩2.0.CO;2.

Held, I. M., M. Winton, K. Takahashi, T. Delworth, F. Zeng, and G. K. Vallis, 2010: Probing the Fast and Slow Components of Global Warming by Returning Abruptly to Preindustrial Forcing. *Journal of Climate*, **23 (9)**, 2418–2427, doi:10.1175/2009JCLI3466.1.

Horowitz, L. W., 2006: Past, present, and future concentrations of tropospheric ozone and aerosols: Methodology, ozone evaluation, and sensitivity to aerosol wet removal. *Journal of Geophysical Research*, **111 (D22)**, D22 211, doi:10.1029/2005JD006937.

Huang, L., S. L. Gong, C. Q. Jia, and D. Lavoué, 2010: Importance of deposition processes in simulating the seasonality of the Arctic black carbon aerosol. *Journal of Geophysical Research Atmospheres*, **115 (17)**, doi:10.1029/2009JD013478.

Huang, Y., X. Tan, and Y. Xia, 2016: Inhomogeneous radiative forcing of homogeneous greenhouse gases. *Journal of Geophysical Research: Atmospheres*, **121 (6)**, 2780–2789, doi:10.1002/2015JD024569.

Iversen, T., and E. Joranger, 1985: Arctic air pollution and large scale atmospheric flows. *Atmospheric Environment (1967)*, **19 (12)**, 2099–2108, doi:10.1016/0004-6981(85)90117-9.

Jacobson, M. Z., 1998: Studying the effects of aerosols on vertical photolysis rate coefficient and temperature profiles over an urban airshed. *Journal of Geophysical Research: Atmospheres*, **103 (D9)**, 10 593–10 604, doi:10.1029/98JD00287.

Jacobson, M. Z., 2002: Control of fossil-fuel particulate black carbon and organic matter, possibly the most effective method of slowing global warming. *Journal of Geophysical Research*, **107 (D19)**, 4410, doi:10.1029/2001JD001376.

Jacobson, M. Z., 2004: Climate response of fossil fuel and biofuel soot, accounting for soot's feedback to snow and sea ice albedo and emissivity. *Journal of Geophysical Research D: Atmospheres*, **109 (21)**, doi:10.1029/2004JD004945.

Jacobson, M. Z., 2010: Short-term effects of controlling fossil-fuel soot, biofuel soot and gases, and methane on climate, Arctic ice, and air pollution health. *Journal of Geophysical Research*, **115 (D14)**, D14 209, doi:10.1029/2009JD013795.

Jacobson, M. Z., 2012: Investigating cloud absorption effects: Global absorption properties of black carbon, tar balls, and soil dust in clouds and aerosols. *Journal of Geophysical Research Atmospheres*, **117 (6)**, doi:10.1029/2011JD017218.

Jacobson, M. Z., and Y. J. Kaufman, 2006: Wind reduction by aerosol particles. *Geophysical Research Letters*, **33 (24)**, L24 814, doi:10.1029/2006GL027838.

Jansen, M., and R. Ferrari, 2013: Equilibration of an Atmosphere by Adiabatic Eddy Fluxes. *Journal of the Atmospheric Sciences*, **70 (9)**, 2948–2962, doi:10.1175/JAS-D-13-013.1.

Janssens-Maenhout, G., and Coauthors, 2015: HTAP_v2.2: a mosaic of regional and global emission grid maps for 2008 and 2010 to study hemispheric transport of air pollution. *Atmospheric Chemistry and Physics*, **15 (19)**, 11 411–11 432, doi:10.5194/acp-15-11411-2015.

Jiao, C., and M. G. Flanner, 2016: Changing black carbon transport to the Arctic from present day to the end of 21st century. *Journal of Geophysical Research: Atmospheres*, **121 (9)**, 4734–4750, doi:10.1002/2015JD023964.

Jones, G. S., P. A. Stott, and N. Christidis, 2008: Human contribution to rapidly increasing frequency of very warm Northern Hemisphere summers. *Journal of Geophysical Research*, **113 (D2)**, D02 109, doi:10.1029/2007JD008914.

Klonecki, A., P. Hess, L. Emmons, L. Smith, J. Orlando, and D. Blake, 2003: Seasonal changes in the transport of pollutants into the Arctic troposphere-model study. *Journal of Geophysical Research*, **108 (D4)**, 8367, doi:10.1029/2002JD002199.

Knutson, T. R., F. Zeng, and A. T. Wittenberg, 2013: Multimodel Assessment of Regional Surface Temperature Trends: CMIP3 and CMIP5 Twentieth-Century Simulations. *Journal of Climate*, **26 (22)**, 8709–8743, doi:10.1175/JCLI-D-12-00567.1.

Koch, D., 2001: Transport and direct radiative forcing of carbonaceous and sulfate aerosols in the GISS GCM. *Journal of Geophysical Research: Atmospheres*, **106 (D17)**, 20 311–20 332, doi:10.1029/2001JD900038.

Koch, D., and J. Hansen, 2005: Distant origins of Arctic black carbon: A Goddard Institute for Space Studies ModelE experiment. *Journal of Geophysical Research*, **110 (D4)**, D04 204, doi:10.1029/2004JD005296.

Koch, D., and Coauthors, 2009: Evaluation of black carbon estimations in global aerosol models. *Atmospheric Chemistry and Physics*, **9 (22)**, 9001–9026, doi:10.5194/acp-9-9001-2009.

Koffi, B., and Coauthors, 2012: Application of the CALIOP layer product to evaluate the vertical distribution of aerosols estimated by global models: AeroCom phase I results. *Journal of Geophysical Research: Atmospheres*, **117 (D10)**, D10 201, doi:10.1029/2011JD016858.

Lamarque, J.-F., G. P. Kyle, M. Meinshausen, K. Riahi, S. J. Smith, D. P. van Vuuren, A. J. Conley, and F. Vitt, 2011: Global and regional evolution of short-lived radiatively-active gases and aerosols in the Representative Concentration Pathways. *Climatic Change*, **109 (1-2)**, 191–212, doi:10.1007/s10584-011-0155-0.

Lamarque, J.-F., and Coauthors, 2010: Historical (18502000) gridded anthropogenic and biomass burning emissions of reactive gases and aerosols: methodology and application. *Atmospheric Chemistry and Physics*, **10 (15)**, 7017–7039, doi:10.5194/acp-10-7017-2010.

Law, K. S., and A. Stohl, 2007: Arctic air pollution: origins and impacts. *Science (New York, N.Y.)*, **315 (5818)**, 1537–40, doi:10.1126/science.1137695.

Levy, H., M. D. Schwarzkopf, L. Horowitz, V. Ramaswamy, and K. L. Findell, 2008: Strong sensitivity of late 21st century climate to projected changes in short-lived air pollutants. *Journal of Geophysical Research*, **113 (D6)**, D06 102, doi:10.1029/2007JD009176.

Li, F., P. Ginoux, and V. Ramaswamy, 2008: Distribution, transport, and deposition of mineral dust in the Southern Ocean and Antarctica: Contribution of major sources. *Journal of Geophysical Research*, **113 (D10)**, D10 207, doi:10.1029/2007JD009190.

Li, X., M. Ting, and D. E. Lee, 2018: Fast Adjustments of the Asian Summer Monsoon to Anthropogenic Aerosols. *Geophysical Research Letters*, **45 (2)**, 1001–1010, doi:10.1002/2017GL076667.

Lin, M., and Coauthors, 2012: Transport of Asian ozone pollution into surface air over the western United States in spring. *Journal of Geophysical Research: Atmospheres*, **117 (D21)**, doi:10.1029/2011JD016961.

Liou, K.-N., and S.-C. Ou, 1989: The role of cloud microphysical processes in climate: An assessment from a one-dimensional perspective. *Journal of Geophysical Research: Atmospheres*, **94 (D6)**, 8599–8607, doi:10.1029/JD094iD06p08599.

Liu, J., S. Fan, L. W. Horowitz, and H. Levy, 2011: Evaluation of factors controlling long-range transport of black carbon to the Arctic. *Journal of Geophysical Research*, **116 (D4)**, D04 307, doi:10.1029/2010JD015145.

Liu, X., P.-L. Ma, H. Wang, S. Tilmes, B. Singh, R. C. Easter, S. J. Ghan, and P. J. Rasch, 2016: Description and evaluation of a new four-mode version of the Modal Aerosol Module (MAM4) within version 5.3 of the Community Atmosphere Model. *Geoscientific Model Development*, **9 (2)**, 505–522, doi:10.5194/gmd-9-505-2016.

Lock, A. P., A. R. Brown, M. R. Bush, G. M. Martin, and R. N. B. Smith, 2000: A New Boundary Layer Mixing Scheme. Part I: Scheme Description and Single-Column Model Tests. *Monthly Weather Review*, **128 (9)**, 3187–3199, doi:10.1175/1520-0493(2000)128⟨3187:ANBLMS⟩2.0.CO;2.

Lorenz, D. J., and E. T. DeWeaver, 2007: Tropopause height and zonal wind response to global warming in the IPCC scenario integrations. *Journal of Geophysical Research Atmospheres*, **112 (10)**, doi:10.1029/2006JD008087.

Lu, J., G. Chen, and D. M. W. Frierson, 2008: Response of the zonal mean atmospheric circulation to El Niño versus global warming. *Journal of Climate*, **21 (22)**, 5835–5851, doi:10.1175/2008JCLI2200.1.

Lu, J., G. a. Vecchi, and T. Reichler, 2007: Expansion of the Hadley cell under global warming. *Geophysical Research Letters*, **34 (6)**, L06 805, doi:10.1029/2006GL028443.

Lu, Y., and Y. Deng, 2016: Impact of Environmental Aerosols on a Developing Extratropical Cyclone in the Superparameterized Community Atmosphere Model. *Journal of Climate*, **29 (15)**, 5533–5546, doi:10.1175/JCLI-D-16-0157.1.

Ma, P.-L., and Coauthors, 2013: The role of circulation features on black carbon transport into the Arctic in the Community Atmosphere Model version 5 (CAM5). *Journal of Geophysical Research: Atmospheres*, **118 (10)**, 4657–4669, doi:10.1002/jgrd.50411.

Malavelle, F. F., and Coauthors, 2017: Strong constraints on aerosol-cloud interactions from volcanic eruptions. *Nature*, **546 (7659)**, 485–491, doi:10.1038/nature22974.

Manabe, S., K. Bryan, and M. J. Spelman, 1990: Transient Response of a Global Ocean-Atmosphere Model to a Doubling of Atmospheric Carbon Dioxide. *Journal of Physical Oceanography*, **20 (5)**, 722–749, doi:10.1175/1520-0485(1990)020⟨0722:TROAGO⟩2.0.CO;2.

Merlis, T. M., 2015: Direct weakening of tropical circulations from masked CO 2 radiative forcing. *Proceedings of the National Academy of Sciences*, **112 (43)**, 13 167–13 171, doi:10.1073/pnas.1508268112.

Ming, Y., and V. Ramaswamy, 2009: Nonlinear Climate and Hydrological Responses to Aerosol Effects. *Journal of Climate*, **22 (6)**, 1329–1339, doi:10.1175/2008JCLI2362.1.

Ming, Y., and V. Ramaswamy, 2011: A Model Investigation of Aerosol-Induced Changes in Tropical Circulation. *Journal of Climate*, **24 (19)**, 5125–5133, doi:10.1175/2011JCLI4108.1.

Ming, Y., V. Ramaswamy, and G. Chen, 2011: A model investigation of aerosol-induced changes in boreal winter extratropical circulation. *Journal of Climate*, **24 (23)**, 6077–6091, doi:10.1175/2011JCLI4111.1.

Ming, Y., V. Ramaswamy, L. J. Donner, V. T. J. Phillips, S. a. Klein, P. a. Ginoux, and L. W. Horowitz, 2007: Modeling the Interactions between Aerosols and Liquid Water Clouds with a Self-Consistent Cloud Scheme in a General Circulation Model. *Journal of the Atmospheric Sciences*, **64 (4)**, 1189–1209, doi:10.1175/JAS3874.1.

Ming, Y., V. Ramaswamy, and G. Persad, 2010: Two opposing effects of absorbing aerosols on global-mean precipitation. *Geophysical Research Letters*, **37 (13)**, doi:10.1029/2010GL042895.

Mitchell, J. M., 1957: Visual range in the polar regions with particular reference to the Alaskan Arctic. *J. Atmos. Terr. Phys. Spec. Suppl*, 195–211.

Moorthi, S., and M. J. Suarez, 1992: Relaxed Arakawa-Schubert. A Parameterization of Moist Convection for General Circulation Models. *Monthly Weather Review*, **120 (6)**, 978–1002, doi:10.1175/1520-0493(1992)120⟨0978:RASAPO⟩2.0.CO;2.

Myhre, G., O. Boucher, F.-M. Bréon, P. Forster, and D. Shindell, 2015: Declining uncertainty in transient climate response as CO2 forcing dominates future climate change. *Nature Geoscience*, **8 (3)**, 181–185, doi:10.1038/ngeo2371.

Myhre, G., and Coauthors, 2013: Anthropogenic and Natural Radiative Forcing. *Climate Change 2013 - The Physical Science Basis*, Intergovernmental Panel on Climate Change, Ed., Cambridge University Press, Cambridge, 659–740, doi:10.1017/CBO9781107415324.018.

Newell, R. E., D. G. Vincent, and J. W. Kidson, 1969: Interhemispheric mass exchange from meteorological and trace substance observations. *Tellus A*, doi:10.3402/tellusa.v21i5.10114.

Ocko, I. B., V. Ramaswamy, and Y. Ming, 2014: Contrasting Climate Responses to the Scattering and Absorbing Features of Anthropogenic Aerosol Forcings. *Journal of Climate*, **27 (14)**, 5329–5345, doi:10.1175/JCLI-D-13-00401.1.

Oshima, N., M. Koike, Y. Zhang, and Y. Kondo, 2009: Aging of black carbon in outflow from anthropogenic sources using a mixing state resolved model: 2. Aerosol optical properties and cloud condensation nuclei activities. *Journal of Geophysical Research*, **114 (D18)**, D18 202, doi:10.1029/2008JD011681.

Paulot, F., and Coauthors, 2016: Sensitivity of nitrate aerosols to ammonia emissions and to nitrate chemistry: implications for present and future nitrate optical depth. *Atmospheric Chemistry and Physics*, **16 (3)**, 1459–1477, doi:10.5194/acp-16-1459-2016.

Paynter, D., and T. L. Frölicher, 2015: Sensitivity of radiative forcing, ocean heat uptake, and climate feedback to changes in anthropogenic greenhouse gases and aerosols. *Journal of Geophysical Research: Atmospheres*, **120 (19)**, 9837–9854, doi:10.1002/2015JD023364.

Persad, G. G., Y. Ming, and V. Ramaswamy, 2012: Tropical Tropospheric-Only Responses to Absorbing Aerosols. *Journal of Climate*, **25 (7)**, 2471–2480, doi:10.1175/JCLI-D-11-00122.1.

Petters, M. D., A. J. Prenni, S. M. Kreidenweis, P. J. DeMott, A. Matsunaga, Y. B. Lim, and P. J. Ziemann, 2006: Chemical aging and the hydrophobic-to-hydrophilic conversion of carbonaceous aerosol. *Geophysical Research Letters*, **33 (24)**, L24 806, doi:10.1029/2006GL027249.

Pressel, K. G., C. M. Kaul, T. Schneider, Z. Tan, and S. Mishra, 2015: Large-eddy simulation in an anelastic framework with closed water and entropy balances. *Journal of Advances in Modeling Earth Systems*, **7 (3)**, 1425–1456, doi:10.1002/2015MS000496.

Quinn, P. K., G. Shaw, E. Andrews, E. G. Dutton, T. Ruoho-Airola, and S. L. Gong, 2007: Arctic haze: current trends and knowledge gaps. *Tellus B*, **59 (1)**, 99–114, doi:10.1111/j.1600-0889.2006.00238.x.

Randles, C. a., and V. Ramaswamy, 2008: Absorbing aerosols over Asia: A Geophysical Fluid Dynamics Laboratory general circulation model sensitivity study of model response to aerosol optical depth and aerosol absorption. *Journal of Geophysical Research*, **113 (D21)**, D21 203, doi:10.1029/2008JD010140.

Reynolds, R. W., N. A. Rayner, T. M. Smith, D. C. Stokes, and W. Wang, 2002: An Improved In Situ and Satellite SST Analysis for Climate. *Journal of Climate*, **15 (13)**, 1609–1625, doi:10.1175/1520-0442(2002)015⟨1609:AIISAS⟩2.0.CO;2.

Rohde, R., R. A. Muller, R. Jacobsen, E. Muller, and C. Wickham, 2013a: A New Estimate of the Average Earth Surface Land Temperature Spanning 1753 to 2011. *Geoinformatics & Geostatistics: An Overview*, **01 (01)**, 1–7, doi:10.4172/2327-4581.1000101.

Rohde, R., R. Muller, R. Jacobsen, S. Perlmutter, and S. Mosher, 2013b: Berkeley Earth Temperature Averaging Process. *Geoinformatics & Geostatistics: An Overview*, **01 (02)**, 1–13, doi:10.4172/2327-4581.1000103.

Rotstayn, L. D., 1997: A physically based scheme for the treatment of stratiform clouds and precipitation in large-scale models. I: Description and evaluation of the microphysical processes. *Quarterly Journal of the Royal Meteorological Society*, **123 (541)**, 1227–1282, doi:10.1002/qj.49712354106.

Rotstayn, L. D., B. F. Ryan, and J. J. Katzfey, 2000: A Scheme for Calculation of the Liquid Fraction in Mixed-Phase Stratiform Clouds in Large-Scale Models. *Monthly Weather Review*, **128 (4)**, 1070–1088, doi:10.1175/1520-0493(2000)128⟨1070:ASFCOT⟩2.0.CO;2.

Schneider, T., and P. a. O'Gorman, 2008: Moist Convection and the Thermal Stratification of the Extratropical Troposphere. *Journal of the Atmospheric Sciences*, **65 (11)**, 3571–3583, doi:10.1175/2008JAS2652.1.

Schulz, M., and Coauthors, 2006: Radiative forcing by aerosols as derived from the AeroCom present-day and pre-industrial simulations. *Atmospheric Chemistry and Physics Discussions*, **6 (3)**, 5095–5136, doi:10.5194/acpd-6-5095-2006.

Schwarz, J. P., and Coauthors, 2013: Global-scale seasonally resolved black carbon vertical profiles over the Pacific. *Geophysical Research Letters*, **40 (20)**, 5542–5547, doi:10.1002/2013GL057775.

Schwarzkopf, M. D., and V. Ramaswamy, 1999: Radiative effects of CH 4 , N 2 O, halocarbons and the foreign-broadened H 2 O continuum: A GCM experiment. *Journal of Geophysical Research: Atmospheres*, **104 (D8)**, 9467–9488, doi:10.1029/1999JD900003.

Seinfeld, J. H., and S. N. Pandis, 2006: *Atmospheric Chemistry and Physics: From Air Pollution to Climate Change*. doi:10.1063/1.882420.

Seinfeld, J. H., and Coauthors, 2016: Improving our fundamental understanding of the role of aerosolcloud interactions in the climate system. *Proceedings of the National Academy of Sciences*, **113 (21)**, 5781–5790, doi:10.1073/pnas.1514043113.

Seo, J., S. M. Kang, and T. M. Merlis, 2017: A model intercomparison of the tropical precipitation response to a CO 2 doubling in aquaplanet simulations. *Geophysical Research Letters*, **44 (2)**, 993–1000, doi:10.1002/2016GL072347.

Sexton, D. M. H., D. P. Rowell, C. K. Folland, and D. J. Karoly, 2001: Detection of anthropogenic climate change using an atmospheric GCM. *Climate Dynamics*, **17 (9)**, 669–685, doi:10.1007/s003820000141.

Sharma, S., 2004: Long-term trends of the black carbon concentrations in the Canadian Arctic. *Journal of Geophysical Research*, **109 (D15)**, D15 203, doi:10.1029/2003JD004331.

Sharma, S., E. Andrews, L. a. Barrie, J. a. Ogren, and D. Lavoué, 2006: Variations and sources of the equivalent black carbon in the high Arctic revealed by long-term observations at Alert and Barrow: 19892003. *Journal of Geophysical Research*, **111 (D14)**, D14 208, doi:10.1029/2005JD006581.

Shaw, G. E., 1981: Eddy diffusion transport of Arctic pollution from the mid-latitudes: A preliminary model. *Atmospheric Environment (1967)*, **15 (8)**, 1483–1490, doi:10.1016/0004-6981(81)90356-5.

Shen, Z., and Y. Ming, 2018: The Influence of Aerosol Absorption on the Extratropical Circulation. *Journal of Climate*, **31 (15)**, 5961–5975, doi:10.1175/JCLI-D-17-0839.1.

Shen, Z., Y. Ming, L. W. Horowitz, V. Ramaswamy, and M. Lin, 2017: On the Seasonality of Arctic Black Carbon. *Journal of Climate*, **30 (12)**, 4429–4441, doi:10.1175/JCLI-D-16-0580.1.

Shin, S. I., and P. D. Sardeshmukh, 2011: Critical influence of the pattern of Tropical Ocean warming on remote climate trends. *Climate Dynamics*, **36 (7)**, 1577–1591, doi:10.1007/s00382-009-0732-3.

Shindell, D., and G. Faluvegi, 2009: Climate response to regional radiative forcing during the twentieth century. *Nature Geoscience*, **2 (4)**, 294–300, doi:10.1038/ngeo473.

Shindell, D. T., and Coauthors, 2008: A multi-model assessment of pollution transport to the Arctic. *Atmospheric Chemistry and Physics*, **8 (17)**, 5353–5372, doi:10.5194/acp-8-5353-2008.

Simmons, A. J., and D. M. Burridge, 1981: An Energy and Angular-Momentum Conserving Vertical Finite-Difference Scheme and Hybrid Vertical Coordinates. *Monthly Weather Review*, **109 (4)**, 758–766, doi:10.1175/1520-0493(1981)109⟨0758:AEAAMC⟩2.0.CO;2.

Singarayer, J. S., J. L. Bamber, and P. J. Valdes, 2006: Twenty-First-Century Climate Impacts from a Declining Arctic Sea Ice Cover. *Journal of Climate*, **19 (7)**, 1109–1125, doi:10.1175/JCLI3649.1.

Skeie, R. B., T. K. Berntsen, G. Myhre, K. Tanaka, M. M. Kvalevåg, and C. R. Hoyle, 2011: Anthropogenic radiative forcing time series from pre-industrial times until 2010. *Atmospheric Chemistry and Physics*, **11 (22)**, 11 827–11 857, doi:10.5194/acp-11-11827-2011.

Smith, S. J., J. van Aardenne, Z. Klimont, R. J. Andres, A. Volke, and S. Delgado Arias, 2011: Anthropogenic sulfur dioxide emissions: 18502005. *Atmospheric Chemistry and Physics*, **11 (3)**, 1101–1116, doi:10.5194/acp-11-1101-2011.

Stohl, A., 2006: Characteristics of atmospheric transport into the Arctic troposphere. *Journal of Geophysical Research*, **111 (D11)**, D11 306, doi:10.1029/2005JD006888.

Stohl, A., Z. Klimont, S. Eckhardt, K. Kupiainen, V. P. Shevchenko, V. M. Kopeikin, and a. N. Novigatsky, 2013: Black carbon in the Arctic: the underestimated role of gas flaring and residential combustion emissions. *Atmospheric Chemistry and Physics*, **13 (17)**, 8833–8855, doi:10.5194/acp-13-8833-2013.

Stouffer, R. J., and Coauthors, 2006: GFDL's CM2 Global Coupled Climate Models. Part IV: Idealized Climate Response. *Journal of Climate*, **19 (5)**, 723–740, doi:10.1175/JCLI3632.1.

Streets, D. G., Y. Wu, and M. Chin, 2006: Two-decadal aerosol trends as a likely explanation of the global dimming/brightening transition. *Geophysical Research Letters*, **33 (15)**, L15 806, doi:10.1029/2006GL026471.

Taylor, K. E., R. J. Stouffer, and G. A. Meehl, 2012: An Overview of CMIP5 and the Experiment Design. *Bulletin of the American Meteorological Society*, **93 (4)**, 485–498, doi:10.1175/BAMS-D-11-00094.1.

Taylor, K. E., D. Williamson, and F. Zwiers, 2000: The sea surface temperature and sea-ice concentration boundary conditions for AMIP II simulations. *PCMDI report No. 60, Program for Climate Model Diagnosis and Intercomparison Climate and Global Dynamics Division, Lawrence Livermore National Laboratory, Livermore, California.*, **(60)**.

Tiedtke, M., 1993: Representation of Clouds in Large-Scale Models. *Monthly Weather Review*, **121 (11)**, 3040–3061, doi:10.1175/1520-0493(1993)121⟨3040:ROCILS⟩2.0.CO;2.

Tomita, H., and M. Satoh, 2004: A new dynamical framework of nonhydrostatic global model using the icosahedral grid. *Fluid Dynamics Research*, **34 (6)**, 357–400, doi:10.1016/j.fluiddyn.2004.03.003.

Twomey, S., 1977: The Influence of Pollution on the Shortwave Albedo of Clouds. *Journal of the Atmospheric Sciences*, **34 (7)**, 1149–1152, doi:10.1175/1520-0469(1977)034⟨1149:TIOPOT⟩2.0.CO;2.

Vecchi, G. A., and B. J. Soden, 2007: Global Warming and the Weakening of the Tropical Circulation. *Journal of Climate*, **20 (17)**, 4316–4340, doi:10.1175/JCLI4258.1.

von Storch, H., and F. W. Zwiers, 1999: *Statistical Analysis in Climate Research*, Vol. 95. Cambridge University Press, Cambridge, 1375 pp., doi:10.1017/CBO9780511612336.

Walker, C. C., and T. Schneider, 2006: Eddy Influences on Hadley Circulations: Simulations with an Idealized GCM. *Journal of the Atmospheric Sciences*, **63 (12)**, 3333–3350, doi:10.1175/JAS3821.1.

Wallace, J. M., Q. Fu, B. V. Smoliak, P. Lin, and C. M. Johanson, 2012: Simulated versus observed patterns of warming over the extratropical Northern Hemisphere

continents during the cold season. *Proceedings of the National Academy of Sciences*, **109 (36)**, 14 337–14 342, doi:10.1073/pnas.1204875109.

Wang, H., and Coauthors, 2013: Sensitivity of remote aerosol distributions to representation of cloudaerosol interactions in a global climate model. *Geoscientific Model Development*, **6 (3)**, 765–782, doi:10.5194/gmd-6-765-2013.

Wang, M., and Coauthors, 2012: Constraining cloud lifetime effects of aerosols using A-Train satellite observations. *Geophysical Research Letters*, **39 (15)**, doi:10.1029/2012GL052204.

Wang, Q., and Coauthors, 2014a: Global budget and radiative forcing of black carbon aerosol: Constraints from pole-to-pole (HIPPO) observations across the Pacific. *Journal of Geophysical Research: Atmospheres*, **119 (1)**, 195–206, doi:10.1002/2013JD020824.

Wang, Y., R. Zhang, and R. Saravanan, 2014b: Asian pollution climatically modulates mid-latitude cyclones following hierarchical modelling and observational analysis. *Nature Communications*, **5**, 3098, doi:10.1038/ncomms4098.

Wang, Y., and Coauthors, 2014c: Assessing the effects of anthropogenic aerosols on Pacific storm track using a multiscale global climate model. *Proceedings of the National Academy of Sciences*, **111 (19)**, 6894–6899, doi:10.1073/pnas.1403364111.

Wiedinmyer, C., S. K. Akagi, R. J. Yokelson, L. K. Emmons, J. a. Al-Saadi, J. J. Orlando, and a. J. Soja, 2011: The Fire INventory from NCAR (FINN): a high resolution global model to estimate the emissions from open burning. *Geoscientific Model Development*, **4 (3)**, 625–641, doi:10.5194/gmd-4-625-2011.

Wofsy, S. C., 2011: HIAPER Pole-to-Pole Observations (HIPPO): fine-grained, global-scale measurements of climatically important atmospheric gases and aerosols. *Philosophical Transactions of the Royal Society A: Mathematical, Physical and Engineering Sciences*, **369 (1943)**, 2073–2086, doi:10.1098/rsta.2010.0313.

Yin, J. H., 2005: A consistent poleward shift of the storm tracks in simulations of 21st century climate. *Geophysical Research Letters*, **32 (18)**, doi:10.1029/2005GL023684.

Zängl, G., D. Reinert, P. Rípodas, and M. Baldauf, 2015: The ICON (ICOsahedral Non-hydrostatic) modelling framework of DWD and MPI-M: Description of the non-hydrostatic dynamical core. *Quarterly Journal of the Royal Meteorological Society*, **141 (687)**, 563–579, doi:10.1002/qj.2378.

Zhang, X., F. W. Zwiers, and P. A. Stott, 2006: Multimodel Multisignal Climate Change Detection at Regional Scale. *Journal of Climate*, **19 (17)**, 4294–4307, doi:10.1175/JCLI3851.1.

Zurita-Gotor, P., and R. S. Lindzen, 2007: Theories of baroclinic adjustment and eddy equilibration. 22–46 pp.

Zurita-Gotor, P., and G. K. Vallis, 2010: Circulation Sensitivity to Heating in a Simple Model of Baroclinic Turbulence. *Journal of the Atmospheric Sciences*, **67 (5)**, 1543–1558, doi:Doi10.1175/2009jas3314.1.